UNIVERSITÀ DEGLI STUDI DI MILANO

Chemistry Department

Doctoral Course in Chemistry, XXX cycle

Fully quantum dynamical studies of Eley-Rideal H_2 recombination on graphite

---

TUTOR:
Prof. Rocco MARTINAZZO

CO-TUTOR:
Dr. Matteo BONFANTI

COORDINATOR:
Prof. Emanuela LICANDRO

PHD STUDENT:
Marta PASQUINI
R10980

A. A.
2016-2017

Contents

Acknowledgments

First of all, I would like to gratefully acknowledge my supervisor, Prof. Rocco Martinazzo, who guided me during my PhD and in the previous years (since my bachelor thesis!); with his contagious enthusiasm, he contributed so much to the grown of my passion for science. I also acknowledge Prof. Irene Burghardt, who kindly hosted me during my stay in Frankfurt.

My co-supervisor (and friend), Dr. Matteo Bonfanti, is also very warmly acknowledged: we worked together on this PhD work as a dream-team and he guided me through physics and maths. He also guided me through Frankfurt, where we cheered each other's German lunch-breaks, rigorously at Italian time.

I want to thank all my ”babies” (who grew up and saved China) for all the laughs, the weird chats, the support we gave each other through the years and overall the time spent together in the office (”Gente in studio” rules): Ambra, Francesca, Nick, Mirko and our colleague-in-law, Fro. I really wish a wonderful future to all of you.

My German friends are also acknowledged for welcoming me in their group and for helping me survive in the serious Germany, with funny chats, laser-games and movie-nights: thanks to Robert, Karno, Jan, Pierre and all the Frankfurter group.

My long-term Italian friends, Lale and Cuccu, stayed by my side throughout these years and they are my second family: caring, supporting, sometimes bizarre, but always indispensable. Thank you for everything.

The most grateful thanks go to my amazing family (cats included) for supporting (and bearing) me through the ups and downs of these challenging years.

Finally, Fede, we started this PhD together and now, at its end, we start something bigger and much more special. Thank you for who I am when I am with you and for what we are when we are together. I love you.

Chapter 1

Introduction

In this chapter we will show why molecular hydrogen formation is a cornerstone reaction for the chemistry of the entire universe. An introduction to the main properties of the interstellar medium will be given, as well as a short review on the H_2 formation mechanisms that occur in space. The importance of graphitic materials will be highlighted and the possible interactions between graphite surface and hydrogen atoms will be illustrated.

1.1 The InterStellar Medium: components and conditions

In astronomy the InteStellar Medium (ISM) is the matter that fills the space between star systems in a galaxy and it consists of ionic and neutral gas (99% of matter), as well as dust grains (1% of matter) and cosmic rays. The interstellar matter is condensed into particular regions, the so-called clouds, which are composed mainly of gas and small dust particles with an average radius of about $r = 0.1$ μm; clouds are classified in diffuse and dense according to temperature and density matter conditions characterizing the environment.

Within diffuse clouds, temperatures are typically between 50 -100 K and the matter densities are very low (10 - 1000 cm^{-3}). According to optical absorption spectroscopy observations, the gaseous phase is mainly atomic and neutral, while molecular species are almost absent. This is primarily due to the strong effects of the interstellar UV radiation, which can indeed easily penetrate in this environment, leading to the photodissociation of molecules and to occasional photoionization of atoms (fractional ionization in the order of 10^{-4})[1]. The elemental abundances are similar to those in the stars: the amount of hydrogen is huge with respect to other elements; indeed, the second most abundant one, helium, has a concentration of about 10% of H.

Dense clouds are in general much colder (10 - 30 K) and have a higher matter density (10^2 - 10^4 cm^{-3}). In this environment, there is a significant amount of interstellar dust, which can shield complex molecules from the destructive stellar radiation; indeed, the dust attenuates the radiation at short wavelengths emitted as starlight, re-emitting it in the infrared[2]. As a consequence, more than 120 different molecular species have been detected within these kind of clouds through emission and absorption spectroscopic techniques. Again, hydrogen dominates the chemical composition: H_2 is the most abundant molecular species and its concentration is about 10^4 times that of the second one, CO. The dense clouds are particularly important for astrophysics because they are the stars birthplaces: portions of matter in the clouds gradually collapse, heating up to the temperature needed for the ignition of nuclear reactions, which mark the birth of a new star[1,3].

1.1.1 Interstellar dust

Unlike the interstellar gas-phase, the exact nature of the dust particles is not yet well established, although some specimens can be provided by meteorites and emission spectroscopy data supply important information. The main spectroscopic features of interstellar dust are the so-called Unidentified Infrared Bands (UIBs): a series of broad emission bands in the infrared region of the spectrum, which are very hard to assign definitively to specific species. Nevertheless, it has been possible to identify the carriers of some of the strongest signals. Some of the most intense bands around 3, 4, 7, 8 and 11 μm closely correspond to the C-H and C-C bond vibrations in aromatic structures, such as simple polycyclic aromatic hydrocarbons (PAHs) and graphitic-like materials. Another important feature is a strong peak at 9.7 μm, which is well compatible with the Si-O stretching in silicate structures[4,5]. These observations and more in-depth investigations led to the conclusion that, in general, dust particles must have a silicate core covered by a mantle, whose composition depends on the environment. In the colder regions of the ISM, icy coatings of H_2O, CO, CO_2 and methanol develop around the grains, while in warmer environment carbon-based, refractory mantles envelop the cores and the smallest particles are entirely carbonaceous with the structure of PAHs. In Figure 1.1 the hypothesized structure of carbonaceous interstellar dust grains is shown[1,5,6].

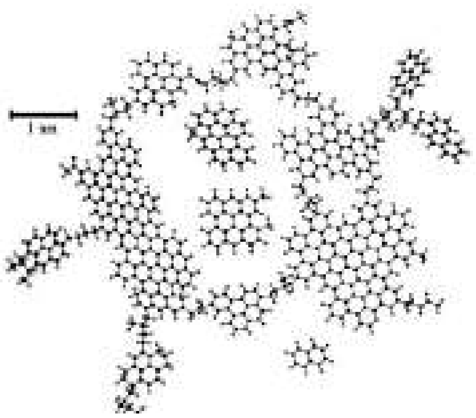

Figure 1.1: The hypothesized structure of carbonaceous dust grains in the ISM, taken from the paper by Ehrenfreund *et al.*[6].

1.1.2 Molecular hydrogen formation in ISM

As previously mentioned, hydrogen is the chemical component dominating the interstellar medium. Being the most abundant molecular species, H_2 is involved in almost every chemical process occurring in the ISM, so that it has a crucial role in the formation of more complex compounds; furthermore, it can act as a radiative cooler during the gravitational collapse of the clouds. The huge concentration of molecular hydrogen is clearly the result of the balance between its formation and dissociation rates. H_2 can form in the gas-phase via different mechanisms involving neutral or ionic hydrogen

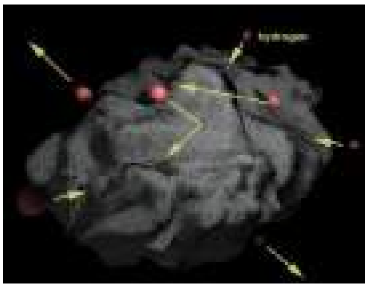

Figure 1.2: Schematic representation of molecular hydrogen formation occurring on an interstellar dust grain[†].

atoms in which the excess of energy due to the bond formation is removed with the emission of an electron e^- or a photon γ:[7]

$$\mathrm{H} + \mathrm{H} \rightarrow \mathrm{H}_2 + \gamma$$
$$\mathrm{H}^- + \mathrm{H} \rightarrow \mathrm{H}_2 + e^-$$

These reactive processes are thought to be fundamental in the chemistry of the primordial universe, when stars and dust grains had not yet appeared[8]. However, at the interstellar medium conditions these reactions are by no means efficient enough to account for the observed amount of molecular hydrogen. This is particularly true since, in addition, H_2 is continuously dissociated by both photons from UV radiation and protons from cosmic rays. Thus, there must be another efficient pathway for H_2 formation in order to explain its amount in the ISM.

It has been proposed that the process occurs on the surface of the interstellar dust grains (schematically represented in Figure 1.2) which should act as catalysts, dissipating the excess of energy resulting from the formation of such a stable molecule through lattice vibrations[9,10]. As mentioned, it has been observed that PAHs and graphite are major components of the interstellar dust grains, so that H_2 is mostly formed on graphitic surfaces. For this reason the hydrogen-graphite system has become prototypical for the investigation of molecular hydrogen formation in the ISM[11–16].

1.2 Hydrogen-graphite system

The interaction between graphitic/graphenic substrates and hydrogen atoms gives rise to a surprisingly complex network of processes; for example, in Figure 1.3 the possible outcome structures due to the interaction between graphitic surface and two H atoms are shown.

Both single and double adsorptions of hydrogen atoms are possible, leading respectively to the formation of CH fragments and dimers CH_2. On one hand, physisorbed adsorbates can diffuse on the surface and eventually recombine, while chemisorbed H atoms can collide with hydrogen atoms coming from the gas phase. The possible paths connecting the initial situation with the two H far from the surface and the final one with a newly formed H_2 correspond to the processes that must be considered in order to gain a complete description of how and under which conditions the molecular hydrogen recombination on graphitic substrate occurs.

[†] Picture taken from https://3c1703fe8d.site.internapcdn.net/newman/gfx/news/hires/2014/2-researchgrou.jpg

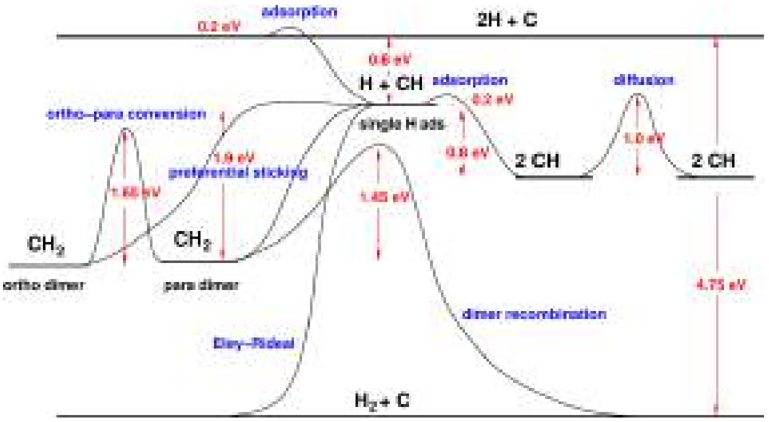

Figure 1.3: Energy diagram of the possible structures due to the interaction between two hydrogen atoms and graphitic substrate. Picture by Martinazzo *et al.*[17].

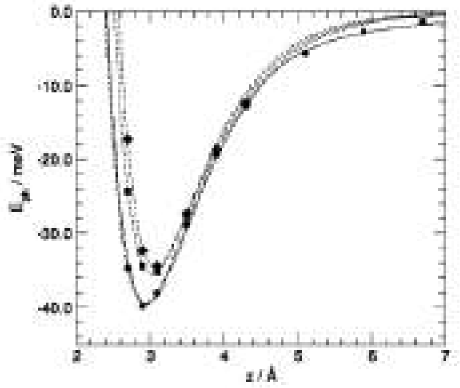

Figure 1.4: Physisorption energies of atomic hydrogen for different graphitic surface sites. Picture by Bonfanti *et al.*[20].

1.2.1 Hydrogen adsorption on graphite

Hydrogen atoms can adsorb onto the regular graphite surface (0001) both physically and chemically. Physisorption of H atoms is barrierless, so that it can in principle occur very easily; however the efficiency of the process is rather low, since for the projectile atoms to physisorb the excess of energy must be dissipated[18]. A physisorbed H atom is accommodated in a quite shallow well of about ∼ 40 meV[19], as reported in Figure 1.4, and can diffuse from site to site across a small barrier (∼ 5 meV) through tunneling, even at the 0 K limit[20]. However, the desorption temperature is about 30 - 40 K, so that it can occur very easily even at clouds conditions; thus, physisorbed hydrogen atoms are absent in the regions of the ISM whose temperature exceeds the desorption threshold.

On the other hand, upon chemisorption, a strong covalent bond is formed between the H atom and a carbon atom of the surface. This leads to the re-hybridization of the C orbitals, from a planar sp^2 conformation to a tetrahedral sp^3 structure, as shown in Figure 1.5. Consequently, the involved carbon atom moves out of the flat graphite surface plane of about 0.4 Å in the so-called puckered configuration and stores a significant amount of energy (∼ 0.8 eV)[21]. This surface rearrangement produces a barrier of ∼ 0.2 eV[21–23], which essentially prevents sticking of cold hydrogen atoms. Thus, chemisorption generally occurs in particular regions of the ISM, characterized

Figure 1.5: Structure of an H atom chemisorbed on graphene showing the extended puckering of the surface around the adatom.

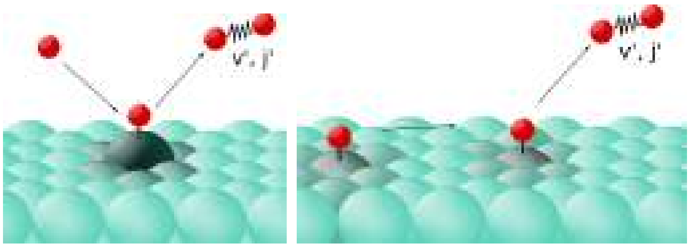

Figure 1.6: Schematic representations of the chemical reaction mechanisms typical of gas-surface processes: Eley-Rideal (left panel) and Langmuir-Hinshelwood (right panel).

by high temperatures (500 - 5000 K), called Photon Dominated Regions, although defects of graphite structure, such as vacancies and edges, can lower the height of the barrier. A considerable energy barrier also prevents the diffusion of chemisorbed species; indeed, H atoms prefer to desorb rather than diffuse since the barrier height matches the desorption threshold.

1.2.2 Gas-surface mechanisms for H_2 recombination

In general, recombination reactions involving surfaces can occur through the well known gas-surface chemistry mechanisms: Langmuir-Hinshelwood (LH), Eley-Rideal (ER) and "Hot-Atom" (HA). A schematic representation of those mechanisms is shown in Figure 1.6. H_2 formation on the surface of interstellar dust grains can in principle take place through any of these processes, although the occurring of each one of them depends on the environmental conditions and on the interaction between the atomic hydrogen and the graphitic substrate.

Molecular species can form via LH reaction when all the reactants are adsorbed and thermalized on the substrate, diffusing onto it until they collide; the impact leads to the formation of products. The formation of H_2 through this mechanism can only occur when both the hydrogen atoms are physisorbed on the surface, since otherwise their diffusion is prevented[24]. In the ER process, on the other hand, only one of the reactants is adsorbed on the surface in thermal equilibrium, while the second one comes from the gas-phase; a direct collision process forms the new molecule. In this case, the adsorbed species can be both physisorbed or chemisorbed on the substrate. The "Hot-Atoms" are atoms "trapped" on the surface: they have a large kinetic energy, higher than the thermal one, which is channeled in the translational motion parallel to the substrate. Thus they hyperthermally diffuse onto it until they encounter the reaction partner. In the chemisorption regime, H atoms remain onto the graphitic substrate even at high temperatures (400 - 500 K) and form H_2 via Hot-Atom or Eley-Rideal reactions[25,26], the latter being particularly efficient.

As already mentioned, the graphitic substrate acts as a catalyst during the reactive process: it dissipates the excess of energy avoiding the dissociation of the newly generated molecule. When the adsorbed hydrogen atom is chemisorbed, the substrate assumes an even important role: indeed, in addition to the exothermicity energy (~3.9 eV), the energy stored in the puckered carbon atom has to be dissipated. The total amount of energy released upon H_2 formation is then distributed between the product, as ro-vibrational and translational energy, and the substrate, as thermal energy. This means that the dissipative properties of the graphitic surface are of primary importance to determine the excitation of H_2 when it leaves the grain.

The ro-vibrational excitation of molecular hydrogen is a key topic in astrochemistry. Indeed, the internal energy of "hot" H_2 is used in a number of important chemical reactions to diminish or climb over an activation barrier or even to overcome endothermicity. The most significative example is relative to the methylidyne ion CH^+, the first molecular ion to be observed in the ISM[27], whose formation process is well known to be endothermic:

$$H_2 + C^+ \rightarrow CH^+ + H$$

It has been hypothesized and then observed that when vibrationally excited molecular hydrogen is involved the rate constant becomes temperature-independent, which is typical of a exothermic reaction between an ion and a non-polar molecule. Thus, the internal energy of H_2 is used to overcome the endothermicity[28].

1.3 Theoretical investigations of H_2 recombination on graphite

Understanding the exact mechanism which leads to molecular hydrogen formation in the interstellar medium is an important goal for the astrochemical and astrophysical scientific community. However, the investigation of this process is a very hard task from both experimental and theoretical point of views. On one hand, setting up an experiment at the exact ISM conditions is still impossible: the average ISM matter density corresponds to a pressure of about 10^{-16} Pa at a temperature of 10 K, which is beyond any ultrahigh vacuum achieved in terrestrial laboratories so far[3]. On the other hand, theoretical investigations need accurate potentials energy surfaces (PES), accurate dynamical models and the use of approaches suitable for dealing with the peculiar features of the title reaction. Indeed, the low mass of hydrogen and the low ISM temperatures implicate strong quantum effects in the entire dynamics; furthermore, the important substrate role has to be included in order to have a complete description of the reactive process.

Currently, theoretical studies of H_2 recombination on graphite are performed resorting to many different models, each one of which allows the correct description of a particular feature of the process. Molecular Dynamics[14] (MD) and Ab Initio Molecular Dynamics[26] (AIMD) are employed when the main focus is the substrate role and its effects on the dynamics. Indeed, classical approaches allow one to include in the simulations many degrees of freedom (DOFs) and, thus, a consistent part of the surface; however, MD and AIMD obviously neglect the quantum effects. The latter are included when a quantum dynamical approach is used[13,25,29,30], although two main technical issues arise. On one side, the inclusion of the substrate implicates dealing with many

DOFs coupled with a complicated potential which would make the quantum simulations computationally unattainable. Hence, the dimensionality of the system has to be reduced, which in general means to consider the surface as flat and rigid and thus to neglect the substrate role. On the other side, dealing with very low temperatures, corresponding to very low translational energies, is challenging with standard quantum dynamical methods. Thus, a complete description of the reaction is still lacking.

This PhD project was devoted to the investigation of the molecular hydrogen recombination on graphitic substrate through the Eley-Rideal mechanism employing quantum dynamical simulations. We developed methodologies and dynamical models able to overcome the limitations of standard approaches. In the first part, we employed the rigid-flat surface approximation to reduce the dimensionality of the system and addressed the problem of the isotope effect focusing on the vanishing collision energies regime. We employed a specific implementation of the standard time-dependent wavepacket method, which allowed us to perform calculations at very low translational energies (down to $\sim 10^{-4}$ eV). In the second part of the project, we investigated the effect of the energy dissipation through the substrate, employing a system-bath model together with high dimensional quantum dynamical simulations performed with the Multi-Configuration Time Dependent Hartree (MCTDH) method.

1.4 Thesis overview

In the present thesis, we will investigate the dynamics of the Eley-Rideal H_2 recombination on graphitic surface using peculiar methodologies and models which will allow us to get a deep insight into this fascinating reactive process and to overcome the limits of traditional techniques.

In chapter 2 we will present the theoretical fundamentals of our work. In particular, we will review the main features of quantum scattering theory in its time dependent approach; then, a summary of time dependent wavepacket methods will be present.

In chapter 3, we will present our research on the isotopic effect in the ER recombination of molecular hydrogen on graphite, an issue that has been only occasionally considered in previous works. We investigated the effects of the substitution of one or both hydrogen atoms with deuterium on reaction cross sections and products rovibrational distributions. In particular, we addressed the vanishing collision energies regime -the one relevant for astrochemistry-, employing a specific implementation which overcomes the limitations of standard time-dependent wavepacket methods.

In chapter 4, the effects on the collinear ER H_2 formation on graphite due to the energy dissipation through the substrate will be considered. We employed a system-bath model, which allows us to evaluate the amount of energy left on the surface after the reactive event and the effects on the internal excitation of the product.

In chapter 5, our future goals and new challenges will be presented, as well as some preliminary results obtained so far.

Chapter 2

Theoretical methods

In this chapter, a brief illustration of the main theoretical methods that have been used throughout this work will be given. The scattering theory investigates how particles collide and it represents the basis of our simulations; in the first part of this chapter the basic concepts of this topic are summarized. In the second part, the main features of time-dependent wavepacket methods will be briefly shown, focusing on the wavefunction representation and its propagation. Lastly, a non-traditional wavepacket method will be described. In the following, atomic units are used, so that $\hbar$=1.

2.1 Quantum scattering theory

The quantum scattering theory is the theoretical background for the analysis of scattering experiments in which a beam of incoming particles is scattered by the interaction with some scattering center. This theory is, in fact, the framework for the investigation of molecular collisions within a quantum setting.

Let's consider a typical scattering event in the gas-phase (for simplicity), such as the one shown in Figure 2.1 in which an incident particle moves towards a scattering center that will deviates the particle due to an interaction potential. The process can be divide into three different regimes:

1. the incident particle approaches the scattering center and the interaction between them is negligible
2. the incident particle collides with the scattering center and its motion is affected by the interaction potential
3. the particle moves far away from the scattering center

and only steps 1. and 3. are directly observable during a scattering experiment. Indeed, the interaction usually occurs within a very short time interval and a very small region of space, so that it cannot be actually detected. As a result, we assume that the full Hamiltonian governing the system dynamics has the following form:

$$H = H^0 + V \tag{2.1}$$

where H^0 is the Hamiltonian of a free particle $H^0 = \frac{p^2}{2m}$ and V is the interaction potential, which is in general local. When the particle is far away from the scattering center, *i.e.* when the interaction between them is negligible (steps 1. and 3.), it behaves

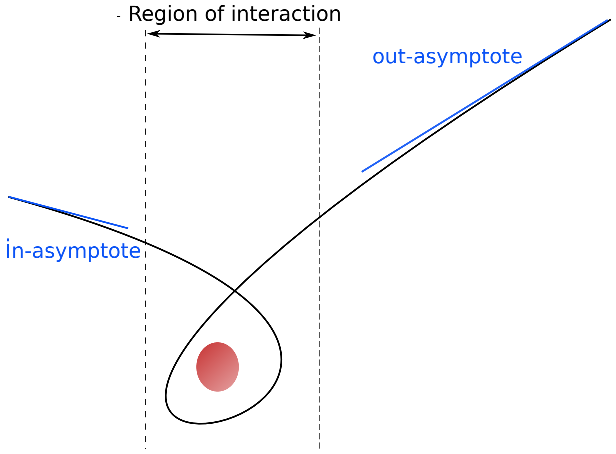

Figure 2.1: Schematic representation of a typical scattering event.

as a free particle, since $V \to 0$ and $H = H^0$; the initial and final states of the system are called respectively *incoming* and *outgoing asymptotes*. During the actual scattering event the effects of interaction potential are not negligible, so that the particle motion evolves according to the full Hamiltonian H.
Through the scattering theory, we want to find the relation between the interaction potential and the transition probabilities between asymptotic states.

2.1.1 Incoming and outgoing asymptotes

In quantum dynamics, the state of a system is completely defined by its state vector $|\psi\rangle$, which satisfies the Time-Dependent Schrödinger Equation

$$i\frac{d}{dt}|\psi\rangle = H|\psi\rangle \tag{2.2}$$

Considering the state vector at $t = 0$ $|\psi_0\rangle$, its time evolution $|\psi_t\rangle$ is given by:

$$|\psi_t\rangle = U(t)|\psi_0\rangle = e^{-iHt}|\psi_0\rangle \tag{2.3}$$

where $U(t) = e^{-iHt}$ is the evolution operator.

Let's consider a scattering process such as the one previously described, in which the collision occurs at $t = 0$. For long time before the interaction with the scattering center, *i.e.* during step 1., when $t \to -\infty$, the particle state vector is represented by a free wavepacket, whose time evolution is given by the free evolution operator $U^0(t) = e^{-iH^0t}$. Hence, in this asymptotic regime, the actual state vector $|\psi\rangle$ is not distinguishable from a free state $|\psi_{in}\rangle$:

$$\lim_{t\to-\infty}\big(U(t)|\psi\rangle - U^0(t)|\psi_{in}\rangle\big) = 0 \tag{2.4}$$

and analogously for long time after the collision:

$$\lim_{t\to+\infty}\big(U(t)|\psi\rangle - U^0(t)|\psi_{out}\rangle\big) = 0 \tag{2.5}$$

$|\psi_{in}\rangle$ and $|\psi_{out}\rangle$ are called the *in* and *out* asymptotes of the actual state vector of the system. It is possible to prove that for every vector $|\psi_{in}\rangle$ and $|\psi_{out}\rangle$ in the Hilbert space $\mathscr{H}$ there is a solution $U(t)|\psi\rangle$ of the Schrödinger equation that is asymptotic to $U^0(t)|\psi_{in/out}\rangle$ as $t \to \pm\infty$; this results is called *asymptotic condition*[31]. Equations 2.4 and 2.5 show that the actual state $|\psi\rangle$ is directly related to its asymptotes. In particular:

$$\begin{aligned} |\psi\rangle &= \lim_{t\to-\infty} U(t)^\dagger U^0(t)|\psi_{in}\rangle \\ |\psi\rangle &= \lim_{t\to+\infty} U(t)^\dagger U^0(t)|\psi_{out}\rangle \end{aligned} \tag{2.6}$$

which allow us to define the *Møller operators* $\Omega_\pm$ as:

$$\Omega_\pm = \lim_{t\to\mp\infty} U(t)^\dagger U^0(t) \tag{2.7}$$

With these operators any actual state at $t = 0$ can be expressed in terms of the asymptotes it would evolve from/to.

The asymptotic condition mentioned above guarantees that every vector in $\mathscr{H}$ ($|\psi_{in}\rangle$, $|\psi_{out}\rangle$) represents the asymptote of some actual state $U(t)|\psi\rangle$. However, the opposite is not always true, *i.e.* not every $|\psi\rangle \in \mathscr{H}$ represents an actual state with incoming/outgoing asymptotes. Indeed, in general, the full Hamiltonian H can have bound states, that are stationary states in which the particle never behaves as free. Now, two important results can be proved.

First, it is possible to verify that any states with asymptotes is orthogonal to all bound states; this is called the *orthogonality theorem*[31] which asserts that:

$$\begin{aligned} \mathscr{B} &\perp \mathscr{R}_+ \\ \mathscr{B} &\perp \mathscr{R}_- \end{aligned} \tag{2.8}$$

Here, $\mathscr{B}$ is the subspace of the bound states, $\mathscr{R}_+$ is the range of Ω_+, made up of the vectors with incoming asymptote $|\psi\rangle = \Omega_+|\psi_{in}\rangle$ and the same for $\mathscr{R}_-$ and the vectors with outgoing asymptote.

The second results is the so-called *asymptotic completeness*[31] which asserts that the set of vectors with incoming asymptote coincides with the set of vectors with outgoing asymptote, *i.e.* $\mathscr{R}_+ = \mathscr{R}_- = \mathscr{R}$. Moreover, since $\mathscr{B} \perp \mathscr{R}$, the Hilbert space of all states $\mathscr{H}$ is just the direct sum of $\mathscr{B}$ and $\mathscr{R}$.

With these two results, we can summarize the description of the scattering process that we obtained so far: considering the actual states of the system, the Hilbert space $\mathscr{H}$ is composed of two orthogonal parts, the subspace of the bound states and the subspace of the scattering states, *i.e.* states with incoming and outgoing asymptotes. The Møller operators previously introduced are then responsible for mapping each asymptote $|\psi_{in/out}\rangle$ onto the corresponding scattering state $|\psi\rangle \in \mathscr{R}$:

$$|\psi\rangle = \Omega_+|\psi_{in}\rangle = \Omega_-|\psi_{out}\rangle$$

Since $\Omega_\pm$ are defined as limits of unitary operators (equation 2.7), they are certainly isometric, *i.e.* norm preserving, and thus $\Omega_\pm^\dagger\Omega_\pm = 1$. However, they map the Hilbert space $\mathscr{H}$ onto the subspace of the scattering states $\mathscr{R}$, which means that in general they are not unitary, *i.e.* $\Omega_\pm\Omega_\pm^\dagger \neq 1$. The only case in which $\Omega_\pm$ are unitary is when the full Hamiltonian has no bound states.

2.1.2 Scattering operator

So far, we have been able to express the actual state vector of the system in terms of one of its asymptotes. However, as previously mentioned, the actual state vector cannot be investigated with a scattering experiment. Thus, our aim is to directly relate the incoming and the outgoing asymptotes.

The expressions $|\psi\rangle = \Omega_{-}|\psi_{out}\rangle$ can be inverted, thanks to the isometric property of the Møller operators, and multiplying on the left side by $\Omega_{-}^{\dagger}$ we obtain:

$$|\psi_{out}\rangle = \Omega_{-}^{\dagger}|\psi\rangle = \Omega_{-}^{\dagger}\Omega_{+}|\psi_{in}\rangle \tag{2.9}$$

We can now define the *scattering operator* S as:

$$S = \Omega_{-}^{\dagger}\Omega_{+} \tag{2.10}$$

so that equation 2.9 becomes:

$$|\psi_{out}\rangle = S|\psi_{in}\rangle \tag{2.11}$$

The scattering operator gives the outgoing asymptote directly in terms of the incoming one: if the incident particle enters the interaction region with the incoming state $|\psi_{in}\rangle$, it will leave with the outgoing state $|\psi_{out}\rangle = S|\psi_{in}\rangle$. The scattering operator contains all the information available from a scattering experiment, so that if it is known, the scattering problem is completely solved.

The most relevant quantity which can be experimentally obtained is the scattering probability and it can be theoretically computed exploiting the scattering operator. The quantity of interest consists in the probability that a particle that entered the interaction region with incoming asymptote $|\psi_{in}\rangle = |\phi\rangle$ will emerge with outgoing asymptote $|\psi_{out}\rangle = |\chi\rangle$. Using the Møller operators, we can define the actual state at $t = 0$ that will evolve from the incoming asymptote $|\phi\rangle$ as $|\phi+\rangle = \Omega_{+}|\phi\rangle$. Analogously, the actual state that would evolve into the outgoing state $|\chi\rangle$ is $|\chi-\rangle = \Omega_{-}|\chi\rangle$. Since the probability of interest corresponds to the scalar product of the actual states at any time, we can write:

$$\begin{aligned} w(\chi \leftarrow \phi) &= |\langle \chi - |\phi+\rangle|^2 \\ &= |\langle \chi|\Omega_{-}^{\dagger}\Omega_{+}|\phi\rangle|^2 \\ &= |\langle \chi|S|\phi\rangle|^2 \end{aligned} \tag{2.12}$$

Hence, the probability amplitude is given by the square of the scattering operator matrix elements $\langle \chi|S|\phi\rangle$.

The scattering operator S and the Møller operators $\Omega_{\pm}$ satisfy some important relations. The *intertwining relation* asserts that the Møller operators and the full and the free Hamiltonians are correlated through:

$$H\Omega_{\pm} = \Omega_{\pm}H^{0} \tag{2.13}$$

and since $\Omega_{\pm}$ are isometric, it can be written as:

$$H^{0} = \Omega_{\pm}^{\dagger}H\Omega_{\pm} \tag{2.14}$$

The above expression shows that the Møller operators act on the full Hamiltonian to give the free Hamiltonian, which is analogous to their action on the state vectors. Concerning the scattering operator, the first fundamental property is that it is unitary. Indeed, because of its definition (equation 2.10) and the isometricity of $\Omega_\pm$, S is linear and norm preserving, *i.e.* it is unitary.
Another important characteristic of the scattering operator is that it guarantees energy conservation. In fact, it commutes with the free Hamiltonian H^0, which means that the incoming and the outgoing asymptotes have the same energy. In order to prove that S commutes with the free Hamiltonian H^0

$$[S, H^0] = 0$$

we simply apply twice the intertwining relation (equation 2.14) getting:

$$SH^0 = \Omega_-^\dagger \Omega_+ H^0 = \Omega_-^\dagger H \Omega_+ = H^0 \Omega_-^\dagger \Omega_+ = H^0 S \tag{2.15}$$

The mean initial energy is:

$$E_{in} = \langle \psi_{in} | H^0 | \psi_{in} \rangle$$

and similarly the mean final energy:

$$E_{out} = \langle \psi_{out} | H^0 | \psi_{out} \rangle$$

Since $|\psi_{out}\rangle = S|\psi_{in}\rangle$ and, according to equation 2.15 $S^\dagger H^0 S = H^0$, we obtain:

$$E_{out} = \langle \psi_{in} | S^\dagger H^0 S | \psi_{in} \rangle = \langle \psi_{in} | H^0 | \psi_{in} \rangle = E_{in}$$

i.e. the initial and the final energies are equal.
Before presenting the third feature of S, it is convenient to introduce its momentum representation, which we refer to as the S-*matrix*, using the momentum eigenvectors:

$$\langle \mathbf{p}' | S | \mathbf{p} \rangle$$

The above expression represents the probability amplitude that an incoming asymptote with momentum $\mathbf{p}$ leads to an outgoing asymptote with momentum $\mathbf{p}'$[*]. Because S commutes with H^0, its momentum representation must satisfy:

$$\begin{aligned} \langle \mathbf{p}' | [H^0, S] | \mathbf{p} \rangle &= 0 \\ &= (E_{p'} - E_p) \langle \mathbf{p}' | S | \mathbf{p} \rangle \end{aligned} \tag{2.16}$$

$$\tag{2.17}$$

which is true when $(E_{p'} - E_p) = 0$ or when $\langle \mathbf{p}' | S | \mathbf{p} \rangle = 0$. Thus, the S-matrix elements are non-zero only if $E_{p'} = E_p$, which represents the energy conservation in the momentum space:

$$\langle \mathbf{p}' | S | \mathbf{p} \rangle \propto \delta(E_{p'} - E_p)$$

We can now introduce the R operator, which is defined by the relation $S = 1 + R$. In absence of any interaction, we would have $S = 1$, so that R represents the difference

---

[*] However, one should remember that $|\mathbf{p}\rangle$ is actually an improper vector, so that it does not represents a physically realizable state. The momentum eigenvectors are just a convenient choice as basis for the expansion of proper vectors.

between this ideal value and the actual value of the scattering operator. The R operator commutes with H^0 and its matrix elements are given by:

$$\langle \mathbf{p}'|R|\mathbf{p}\rangle = -2\pi i\delta(E_{p'} - E_p)t(\mathbf{p}' \leftarrow \mathbf{p}) \tag{2.18}$$

The above expression allows us to write a useful decomposition of the S-matrix as:

$$\langle \mathbf{p}'|S|\mathbf{p}\rangle = \delta(\mathbf{p}' - \mathbf{p}) - 2\pi i\delta(E_{p'} - E_p)t(\mathbf{p}' \leftarrow \mathbf{p}) \tag{2.19}$$

The first term on the right-hand side represents the amplitude in absence of any interaction between the incident particle and the scattering center and the momentum is completely conserved. The second term is the amplitude that the particle is actually scattered, in which the energy is conserved, but the individual components of the momentum are allowed to change. $t(\mathbf{p}' \leftarrow \mathbf{p})$ is a smooth function of its argument and, because of the factor $\delta(E_{p'} - E_p)$, it is defined only on the "shell" $\mathbf{p}'^2 = \mathbf{p}^2$ and it is called the *on shell T-matrix*. The latter can be used to define the scattering amplitude $f(\mathbf{p}' \leftarrow \mathbf{p})$ as:

$$f(\mathbf{p}' \leftarrow \mathbf{p}) = -(2\pi)^2 m\, t(\mathbf{p}' \leftarrow \mathbf{p}) \tag{2.20}$$

The scattering amplitude has a central role in the scattering theory, since it is directly related to the the observable cross section σ through:

$$\frac{d\sigma}{d\Omega} = |f(\mathbf{p}' \leftarrow \mathbf{p})|^2 \tag{2.21}$$

The above equation expresses the differential cross section in terms of the matrix elements of the scattering operator S.

2.1.3 Scattering states

The scattering states are the improper eigenvectors of the full Hamiltonian $H = H^0 + V$ that can be used to express the scattering amplitude. They are defined as:

$$H|E\alpha\pm\rangle = \epsilon_\alpha|E\alpha\pm\rangle \tag{2.22}$$

and considering the eigenvectors of the free Hamiltonian:

$$H^0|E\alpha\rangle = \epsilon'_\alpha|E\alpha\rangle$$

the latter are related with the scattering states through the Møller operators:

$$|E\alpha\pm\rangle = \Omega_\pm|E\alpha\rangle \tag{2.23}$$

Moreover the scattering states are characterized by the same energy eigenvalue of the corresponding free states, *i.e.* $\epsilon_\alpha = \epsilon'_\alpha$. This can be proved using the intertwining relation:

$$\begin{aligned} H|E\alpha\pm\rangle &= \epsilon_\alpha|E\alpha\pm\rangle \\ &= H\Omega_\pm|E\alpha\rangle = \Omega_\pm H^0|E\alpha\rangle = \epsilon'_\alpha\Omega_\pm|E\alpha\rangle = \epsilon'_\alpha|E\alpha\pm\rangle \end{aligned}$$

$$\Rightarrow \epsilon_\alpha = \epsilon'_\alpha$$

The scattering states must indeed smoothly evolve into free states of the same energy upon removal of the interaction potential $V \to 0$. $\{|E_\alpha \pm\rangle\}$ can be also used to express the projectors onto the improper eigenstates at a certain energy of the full Hamiltonian:

$$P = \delta(E - H) = \sum_\alpha |E\alpha\pm\rangle\langle E\alpha\pm| \tag{2.24}$$

In order to obtain information about a scattering event through a quantum calculation, two approaches can be used. On one hand, in a *Time-Independent* method, the time-independent Schrödinger equation (equation 2.22) is solved with the appropriate scattering boundary conditions, and the scattering states are analyzed to obtain the quantities of interest (scattering amplitudes). On the other hand, in a *Time-Dependent* approach the wavefunction is time-propagated and energy-resolved information about the dynamics can be obtained through the time-energy mapping (time-to-energy Fourier transform). Throughout our work, we employed Time-Dependent wavepacket methods to simulate the gas-surface processes of interest.

2.2 Standard Time-Dependent Wavepacket method

The time-dependent wavepacket methods are based on the solution of the Time-Dependent Schrödinger Equation:

$$i\frac{d}{dt}|\psi\rangle = H|\psi\rangle \tag{2.25}$$

whose general solution is

$$|\psi\rangle = U(t)|\psi_0\rangle = e^{-iHt}|\psi_0\rangle \tag{2.26}$$

In this approach, the wavefunction is represented on an appropriate basis and propagated in time. Its time evolution $|\psi\rangle$ contains all the information regarding the system, so that any property can be computed. Moreover, employing the time-energy mapping, it is possible to obtain expectation values and cross sections for a wide range of energies from the data of a single propagation.

The standard approach for solving equation 2.25 is a numerically exact propagation of the wavepacket represented on a time-independent basis-set. The wavefunction is then expressed as:

$$\psi(Q_1, \dots Q_f, t) = \sum_{j_1=1}^{N_1} \dots \sum_{j_f=1}^{N_f} C_{j_1 \dots j_f} \chi_{j_i}(Q_1) \dots \chi_{j_f}(Q_f) \tag{2.27}$$

where f is the number of degrees of freedom, $C_{j_1 \dots j_f}$ are the time-dependent expansion coefficients and $\chi_{j_i}(Q_1) \dots \chi_{j_f}(Q_f)$ are the time-independent basis functions.
In the following, the wavefunction representation problem will be briefly discussed, with the introduction of a very popular technique for the definition of the time-independent basis. Then, an efficient method for evolving the wavefunction will be illustrated. In the third and final part of this section, an approximate time-dependent approach, the Multi Configuration Time-Dependent Hartree (MCTDH) method, will be presented.

2.2.1 Wavepacket representation

The wavefunction is a continuous object, which has to be represented within a numerical procedure in order to perform quantum dynamical calculations. A convenient choice is to use discrete grids, so that the wavepacket is expanded on basis functions extremely localized on the grid. This kind of basis is called Discrete Variable Representation (DVR)[32,33].

In order to define a generic DVR, let's denote the space on which the wavefunctions live with $\mathscr{M}$ and the Hilbert space of square-integrable wavefunctions on $\mathscr{M}$ with $\mathscr{H} = L^2(\mathscr{M})$. Let's now define a projection operator on $\mathscr{H}$, P, and the subspace $\mathscr{S}$ such that $\mathscr{S} = P\mathscr{H}$. The last elements that we need are a set of N grid points on $\mathscr{M}$ $\{x_\alpha, \alpha = 0, \ldots, N-1\}$ and a set of δ-functions, each one of them being projected onto a grid point $\Delta_\alpha = P[\delta(x-x_\alpha)]$. The last expression can be conveniently written in Dirac notation $|\Delta_\alpha\rangle = P|x_\alpha\rangle$, so that $\Delta_\alpha(x) = \langle x|\Delta_\alpha\rangle$. The combination of the projector P and the grid points $\{x_\alpha\}$ forms a DVR set if the vectors $|\Delta_\alpha\rangle$ are *orthogonal*:

$$\langle\Delta_\alpha|\Delta_\beta\rangle = \Delta_\beta(x_\alpha) = \Delta_\alpha(x_\beta)^* \tag{2.28}$$

and *complete* in the subspace $\mathscr{S}$.

Equation 2.28 means that the overlap matrix of the projected δ-functions is obtained by evaluating them at each other grid points and thus it follows that:

$$\Delta_\alpha(x_\beta) = K_\alpha \delta_{\alpha\beta} \tag{2.29}$$

where $K_\alpha = \langle\Delta_\beta|\Delta_\alpha\rangle$ is the squared norm of Δ_α. If the $\{\Delta_\alpha(x)\}$ do not vanish identically and thus K_α is always non-zero and positive, we can define the orthonormal DVR set as:

$$|F_\alpha\rangle = \frac{1}{\sqrt{K_\alpha}}|\Delta_\alpha\rangle \tag{2.30}$$

so that $\langle F_\alpha|F_\beta\rangle = \delta_{\alpha\beta}$.

Thus, the two properties that a DVR set must satisfy are:

- orthogonality $\langle F_\alpha|F_\beta\rangle = \delta_{\alpha\beta}$
- interpolation $F_\alpha(x_\beta) = \delta_{\alpha\beta}$

The interpolation property means that every DVR function must vanish at all grid points but its own.

If the subspace $\mathscr{S}$ is finite-dimensional with $dim\mathscr{S} = N$, the set of projected δ-functions is complete if the number of grid points, and thus the number of functions, is equal to the dimensionality of $\mathscr{S}$. In this situation the DVR functions are orthonormal, non-vanishing and form a linearly independent set, so that $\{F_\alpha\}$ are an orthonormal basis of the subspace.

The two main properties of a DVR set, interpolation and orthogonality, allow one to expand a function $\psi \in \mathscr{S}$ using two different procedures for the definition of the expansion coefficients. Indeed, if ψ belongs to the subspace $\mathscr{S}$, the following expansion exists:

$$\psi(x) = \sum_\alpha c_\alpha F_\alpha(x) \tag{2.31}$$

The coefficients c_α can be determined exploiting the orthogonality feature or by setting $x = x_\beta$ and using the corollary 2.29. Thus $\{c_\alpha\}$ are given by

$$c_\alpha = \int dx F_\alpha^*(x)\psi(x) = \frac{1}{\sqrt{K_\alpha}}\psi(x_\alpha) \tag{2.32}$$

so that they are simply the values of the function that we want to represent at each grid point; these coefficients are the Discrete Variable Representation of the function $\psi(x)$. The latter can be fully expressed as:

$$\psi(x) = \sum_\alpha \frac{1}{\sqrt{K_\alpha}}\psi(x_\alpha)F_\alpha(x) \tag{2.33}$$

Many different kinds of DVR are available and the choice is strongly related to the addressed problem and to the features of the degrees of freedom that are considered. For example, it is possible to choose polynomials basis functions such that they are eigenvectors of a part of the Hamiltonian; for example, Hermite polynomials for vibrational DOFs or Legendre polynomials (spherical harmonics) for rotational DOFs.

For scattering coordinates a convenient option is the exponential (*aka* Fourier) DVR[34], which makes use of plane waves as basis functions. The DVR set is defined by the following projector:

$$P = \int_{-p_{max}}^{+p_{max}} dp|p\rangle\langle p|$$

and by a uniform set of grid points:

$$x_\alpha = \frac{\pi}{p_{max}}\alpha$$

with $\alpha \in Z$. The DVR functions are then:

$$|\Delta_\alpha\rangle = \int_{-p_{max}}^{+p_{max}} dp\frac{e^{-ipx_\alpha}}{\sqrt{2\pi}}$$

and the corresponding orthonormal functions are:

$$F_\alpha(x) = \sqrt{\frac{\pi}{p_{max}}}\Delta_\alpha(x) = \frac{1}{\pi p_{max}} = \delta_{\alpha\beta}\frac{p_{max}}{\pi}$$

Through an infinite but discrete set of functions, the DVR set $\{F_\alpha\}$ allows one to exactly represent any function which is *band-limited* -because of the truncation in the momentum space- as:

$$|\psi\rangle = \sum_\alpha |F_\alpha\rangle\frac{\pi}{p_{max}}\psi(x_\alpha)$$

Since in practical applications, only a finite number of functions, *i.e.* a finite number of grid points $|\alpha| < N$, can be used, a discretization in the momenta is also introduced, so that $p_\alpha = \frac{p_{max}}{N}\alpha$. Moreover, in this representation, the wavefunction satisfies periodic boundary conditions, so that $\psi(x_0) = \psi(x_N)$.
Considering a one Cartesian dimension and a interval $a = N\Delta x$, the kinetic matrix elements $\langle x_i|T|x_j\rangle$ for a odd number of grid points, $N = 2M + 1$, are given as:

$$T_{ii} = \frac{2\pi^2}{ma^2}\frac{(M(M+1))}{3}$$
$$T_{ij} = \frac{2\pi^2}{ma^2}\frac{(-1)^{i-j}}{2}\frac{\cos\left(\frac{\pi(i-j)}{N}\right)}{\sin^2\left(\frac{\pi(i-j)}{N}\right)}$$

where m is the mass. If the number of grid points is even, $N = 2M$, the matrix elements are:

$$T_{ii} = \frac{2\pi^2}{ma^2}\frac{(2M^2+1)}{6}$$
$$T_{ij} = \frac{2\pi^2}{ma^2}\frac{(-1)^{i-j}}{2}\frac{1}{\sin^2\left(\frac{\pi(i-j)}{N}\right)}$$

This DVR set underlies the use of Fast Fourier Transform.

The *sync* DVR[35] is similar to the exponential one, but makes use of particle-in-a-box eigenfunctions as a basis. In this case, the boundary conditions are $\psi(x_0) = \psi(x_{N+1}) = 0$, where x_0 and x_{N+1} do not actually belong to the grid; the grid interval (*i.e.* the length of the box) is then $a = (N+1)\Delta x$.
In this representation, the kinetic energy matrix elements read as:

$$T_{ii} = \frac{\pi^2}{4ma^2}\left[\frac{2(N+1)^2+1}{3}\frac{1}{\sin^2\left(\frac{\pi i}{(N+1)}\right)}\right]$$
$$T_{ij} = \frac{\pi^2(-1)^{i-j}}{4ma^2}\left[\frac{1}{\sin^2\left(\frac{\pi(i-j)}{(N+1)}\right)} - \frac{1}{\sin^2\left(\frac{\pi(i+j)}{(N+1)}\right)}\right]$$

2.2.2 Wavepacket propagation

In order to perform the actual time propagation of the wavepacket, we need to evaluate the expression in equation 2.26 and in particular to compute the quantum propagator $U(t) = e^{-iHt}$. This can be achieved with the direct diagonalization of the Hamiltonian operator H, although it can be done exactly only for a very small number of DOFs. In general, indeed, approximation techniques are needed and, among them, the split-operator is a very common one.

The split operator is one of the simpler methods for time evolution propagation of wavepackets. It is very useful when the global, time-independent Hamiltonian H can be expressed as sum of terms which depend on different variables such as a kinetic and a potential term.
The first step is to represent the propagator over the whole time interval $[0, t]$ as a product of N propagators over short time interval Δt, such that $N\Delta t = t$:

$$U(t) = \underbrace{e^{-iH\Delta t}e^{-iH\Delta t}\cdots e^{-iH\Delta t}}_{N\text{ times}} \tag{2.34}$$

Then, each short time propagator is approximated as a product of a kinetic and a potential factor:

$$e^{-iH\Delta t} = e^{-i(\frac{\hat{p}^2}{2m}+V(\hat{x}))\Delta t} \approx e^{-iT\Delta t}e^{-iV\Delta t} + \mathcal{O}(\Delta t^2) \tag{2.35}$$

Since T and V do not commute, an error proportional to their commutator $[T, V]$ appears. This can be proved by considering the Taylor expansions of $e^{-i(T+V)\Delta t}$ and of $e^{-iT\Delta t}e^{-iV\Delta t}$ and then subtracting the two expressions. The result represents the error, whose leading order is given by:

$$\text{error} = \frac{TV - VT}{2}\frac{\Delta t^2}{\hbar^2} + \cdots \tag{2.36}$$

It can be analogously demonstrated that the leading order error can be lowered by using a symmetric product of kinetic and potential factors:

$$e^{-iH\Delta t} \approx e^{-iV\frac{\Delta t}{2}}e^{-i\frac{p^2}{2m}\Delta t}e^{-iV\frac{\Delta t}{2}} \tag{2.37}$$

In this case, the error becomes:

$$\text{error} = i\frac{\Delta t^3}{\hbar^3}\left(\frac{[T,[V,T]]}{12} + \frac{[V,[V,T]]}{24}\right) \tag{2.38}$$

This approach is particularly advantageous when applied to a specific configurations space. In fact, the kinetic operator is diagonal in momentum space, while a local potential is diagonal in coordinates space. Thus, the operation $e^{-iV\frac{\Delta t}{2}}\psi$ can be computed by simple multiplication, using the coordinates representation of the wave function, $\psi(x)$. Then, the kinetic factor $e^{-i\frac{p^2}{2m}\Delta t}\psi$ is performed as $Ze^{-i\frac{p^2}{2m}\Delta t}Z^\dagger\psi(x)$, where $Z^\dagger$ is the transformation between coordinates and momentum representations. The efficiency of this approach can be increased employing the exponential DVR for the wavefunction representation (described in section 2.2.1), since in this case it is possible to exploit the Fast Fourier Transform (*FFT*) algorithm. Considering N basis functions, the computational cost to apply the transformation Z is proportional to N^2 with standard vector-matrix operations, while with the *FFT* procedure the cost scales as $N \log N$. The main limit is that the set of grid points must be uniformly spaced, which means that the less interesting parts of the potential are represented with the same accuracy of the most important regions.

2.2.3 Final analysis

When a quantum dynamical simulation is performed with a time-dependent method, the wavefunction in time domain $\psi(t)$ is the main outcome of the calculation; the latter must then be manipulated to extract the desired information. In fact, from $\psi(t)$ it is possible to compute the scattering states, which can be used to obtain the scattering amplitudes.

This is achieved through the time-energy mapping of the dynamics, whose application is made possible by the imposition of two "asymptotic conditions" that the initial wavepacket must satisfy:

(i) it is localized in the asymptotic reagents region;

(ii) it has only *incoming* momentum components.

When the above conditions are fulfilled, two important relations can be found. Firstly, it is possible to relate the forward propagation to the (differential) eigenprojector on the energy shell $\delta(E-H)$, namely through

$$\begin{aligned}\langle \mathbf{x}|\Psi_E\rangle = \int_0^\infty e^{iEt}\,\langle \mathbf{x}\,|\,\Psi_t\rangle\,dt &\approx \int_{-\infty}^\infty e^{iEt}\,\langle \mathbf{x}\,|\,\Psi_t\rangle\,dt \\ &= 2\pi\,\langle \mathbf{x}\,|\,\delta(E-H)\,|\,\Psi_0\rangle\end{aligned}$$

Here $|\Psi_t\rangle = U_t\,|\Psi_0\rangle = e^{-iHt}\,|\Psi_0\rangle$ is the time-evolving wavepacket and $\mathbf{x}$ is an arbitrary point in the system configuration space which is *not* in the reagent region. This expression holds because assumptions (i) and (ii) guarantee that in this case the past dynamics makes no contributions to the amplitude to be integrated. Secondly, they relate the initial state $|\Psi_0\rangle$ to the desired scattering states through the appropriate energy weights. Indeed, using equation 2.24, we can express the eigenprojector on the energy shell $\delta(E-H)$ through a scattering states expansion and, if α is the initial internal state, the r.h.s. of the above equation simplifies to

$$\begin{aligned}2\pi\,\langle \mathbf{x}\,|\,\delta(E-H)\,|\,\Psi_0\rangle &= 2\pi\sum_\beta \langle \mathbf{x}|E\beta+\rangle\,\langle E\beta+|\Psi_0\rangle \\ &\approx 2\pi\,\langle \mathbf{x}|E\alpha+\rangle\,\langle E\alpha|\Psi_0\rangle\end{aligned}$$

Here $|E\beta+\rangle$ is a scattering (outgoing) eigenstate corresponding to the precollisional $|E\beta\rangle$ eigenstate, the sum runs over the open channels of every arrangement, and in the last step we have used

$$\begin{aligned}\langle E\beta+|\Psi_0\rangle &= \lim_{t\to-\infty}\langle E\beta|U_t^{0,\beta\,\dagger}U_t|\Psi_0\rangle \\ &= \delta_{\alpha\beta}\,\langle E\alpha|\Psi_0\rangle\end{aligned}$$

($U_t^{0,\beta}$ being the free-evolution operator for channel β) which holds thanks to the conditions above. Finally, one obtains

$$\langle \mathbf{x}|E\alpha+\rangle = \frac{1}{2\pi}\frac{\sqrt{\bar{v}}}{\psi_0(-\bar{p})}\int_0^\infty e^{iEt}\,\langle \mathbf{x}\,|\,\Psi_t\rangle\,dt \tag{2.39}$$

where $\langle E\alpha|\Psi_0\rangle$ has been expressed in terms of the initial momentum wavefunction $\psi_0(p)$ for the motion in the scattering coordinate - *i.e.* $\langle E\alpha|\Psi_0\rangle \equiv \psi_0(-\bar{p})/\sqrt{\bar{v}}$ - and $\bar{p}$, $\bar{v}$ (≥ 0) are the entrance channel momentum and speed, respectively.

In general, one needs the amplitude of the scattering states only at specific configuration points, where the flux is computed. Indeed, these are enough to obtain information about the dynamics. For example, the probability $P_{\alpha\to\beta}$ for the collisional transition to a product internal state β reads as:

$$\begin{aligned}P_{\alpha\to\beta}(E) &= 2\pi\,\langle E\alpha+|F_\beta^\infty|E\alpha+\rangle \\ &= \frac{2\pi}{m'}\Im\left\{\Phi^*_{\alpha\to\beta}(R_\infty,E)\frac{\partial\Phi_{\alpha\to\beta}}{\partial R}(R_\infty,E)\right\}\end{aligned}$$

where F_β^∞ is the flux operator in the β product channel.

2.3 MCTDH

In standard time-dependent wavepacket techniques, the wavefunction is expressed in terms of time-independent basis functions, such as DVR, weighted through time-dependent coefficients:

$$\Psi(q_1, q_2, \ldots, q_f, t) = \sum_{j_1=1}^{n_1} \cdots \sum_{j_f=1}^{n_f} A_{j_1 \ldots j_f}(t) \prod_{k=1}^{f} \chi_{j_f}^{(k)}(q_k) \tag{2.40}$$

where f is the number of degrees of freedom and n_i is the number of basis functions chosen to represent each DOF. One of the main problem with this standard approach is the exponential increase of both memory requirements and computational cost with the number of DOFs f.

Let's suppose that the number of basis functions for each degree of freedom is the same $n_1 = n_2 \ldots = n_f = n$ and that the kinetic part of the Hamiltonian can be expressed as a tensor; the potential operator is diagonal on a DVR grid. We can define the computational effort as the number of floating point operations that must be computed to solve the equations of motion for the coefficients. In this case, the effort turns out to be proportional to fn^{f+1}. This is known as the *dimensionality curse*, since it restricts the standard method to systems composed of just few degrees of freedom.

A successful approach developed to overcome this issue is the Multi-Configuration Time Dependent Hartree (MCTDH) method[36–38]: it employs a different wavefunction expansion with respect to other approaches, so that the exponential scaling is alleviated. In the following, the main features of the MCTDH method will be described.

2.3.1 Wavefunction *ansatz*

In the MCTDH approach the wavefunction is expressed as direct product expansion of sets of orthonormal, time-dependent basis functions, called Single Particle Functions (SPFs), weighted via time-dependent coefficients. Considering a system composed of f degrees of freedom, the wavefunction will be expressed as:

$$\begin{aligned}\Psi(q_1, q_2, \ldots, q_f, t) &= \Psi(Q_1, Q_2, \ldots, Q_p, t) \\ &= \sum_{j_1=1}^{n_1} \cdots \sum_{j_p=1}^{n_p} A_{j_1 \ldots j_p}(t) \phi_{j_1}^{(1)}(Q_1, t) \ldots \phi_{j_p}^{(p)}(Q_p, t) \\ &= \sum_J A_J \Phi_J \end{aligned} \tag{2.41}$$

where the coordinates Q_k are the so-called combined modes and they can be composite of one or more system coordinates:

$$Q_k = (q_a, q_b \ldots)$$

so that the total number of SPFs is reduced from f to p. $\phi_{j_k}^{(k)}(Q_k, t)$ are the n_k single particle functions relative to the k combined mode; each one of them is expanded in a chosen time-independent basis set $\{|u_a^{(k)}\rangle\}$, such as the DVR basis:

$$|\phi_{j_k}^{(k)}(Q_k, t)\rangle = \sum_{a}^{m_{j_k}} B_{a,j_k}^{(k)}(t) |u_a^{(k)}\rangle \tag{2.42}$$

Before deriving the Equations of Motion (EoMs) for the MCTDH approach, it is convenient to introduce some notations:

- the projector on the subspace spanned by the SPFs relative to the k combined mode is defined as:
$$P^{(k)} = \sum_{j=1}^{n_k} |\phi_j^{(k)}\rangle\langle\phi_j^{(k)}|$$
- the single-hole functions $\Psi_l^{(k)}$ are defined as the linear combinations of Hartree products which contain all the SPFs, but the ones associated with the k coordinate:
$$\begin{aligned}\Psi_l^{(k)} &= \sum_{j_1}^{n_1}\cdots\sum_{j_{k-1}}^{n_{k-1}}\sum_{j_{k+1}}^{n_{k+1}}\cdots\sum_{j_p}^{n_p} A_{j_1\ldots j_{k-1},j_{k+1}\ldots j_p}(t)\phi_{j_1}^{(1)}\ldots\phi_{j_{k-1}}^{(k-1)},\phi_{j_{k+1}}^{(k+1)}\ldots\phi_{j_p}^{(p)}\\ &= \sum_{J^k} A_{J_l^k}\phi_{j_1}^{(1)}\ldots\phi_{j_{k-1}}^{(k-1)},\phi_{j_{k+1}}^{(k+1)}\ldots\phi_{j_p}^{(p)}\end{aligned}$$
- the Hamiltonian mean field is given by:
$$\langle H_{jl}^{(k)}\rangle = \langle\Psi_j^{(k)}|H|\Psi_l^{(k)}\rangle$$
- the density matrices are defined as:
$$\rho_{jl}^{(k)} = \langle\Psi_j^{(k)}|\Psi_l^{(k)}\rangle = \sum_{J^k} A^*_{J_j^k}A_{J_l^k}$$

With this notation, we can express the complete wavefunction as:

$$\Psi = \sum_J A_J\Phi_J = \sum_j^{n_k}\phi_j^{(k)}\Psi_j^{(k)} \tag{2.43}$$

2.3.2 The constraint operator

The representation of the wavefunction in equation 2.43 is not unique. Indeed, in principle, every well-defined function is admissible as an SPF; however, if two different sets of functions $\{\Phi_J\}$ and $\{\widetilde{\Phi}_J\}$ span the same Hilbert subspace, it is always possible to define the coefficients $\widetilde{A}_J$ so that

$$\Psi(Q_1, Q_2, \ldots, Q_p, t) = \sum_J A_J\Phi_J = \sum_J \widetilde{A}_J\widetilde{\Phi}_J$$

and thus one can freely alternate between different spanning sets of the same subspace. Consequently, only the time evolution of the subspace is determined, while the evolution of the individual SPFs is not fixed. Such redundancies prohibit well-defined and singularity-free equations of motion[39].

In order to obtain a uniquely defined propagation, two constraints on the single particle functions are imposed. In particular, the SPFs are chosen to be orthonormal at $t = 0$:

$$\langle\phi_j^{(k)}(0)|\phi_l^{(k)}(0)\rangle = \delta_{jl} \tag{2.44}$$

and their time evolution is fixed so that they remain orthonormal for all times, so that:

$$\langle \phi_j^{(k)}(t) | \dot{\phi_l}^{(k)}(t) \rangle = -i \langle \phi_j^{(k)}(t) | h^{(k)} | \phi_l^{(k)}(t) \rangle \tag{2.45}$$

where $h^{(k)}$ is the so-called constraint operator. It is Hermitian, but otherwise arbitrary; the standard choice is to set $h^{(k)} = 0$ for all DOFs, which is also our choice in the following derivation of the equations of motion.

2.3.3 Equations of motion

The equations of motion of the MCTDH method are obtained with a variational approach based on the Dirac-Frenkel variational principle

$$\langle \delta\Psi | \hat{H} - i\partial_t | \Psi \rangle = 0 \tag{2.46}$$

In particular, we find all the allowed variations of the wavefunction $\delta\Psi$ by deriving the *ansatz* (equation 2.43):

- variation along the single particle functions

$$\delta\Psi / \delta\phi_j^{(k)} = \Psi_j^{(k)} \tag{2.47}$$

- variation along the coefficients

$$\delta\Psi / \delta A_J = \Phi_J \tag{2.48}$$

The time derivative approximation error $(H - i\partial_t)\Psi$ is then projected over the above $\delta\Psi$ in order to obtain the EoMs. The latter are a coupled set of equations, one for the coefficients and one for the SPFs:

$$\begin{gathered} \langle \delta\Psi | \hat{H} - i\partial_t | \Psi \rangle_{SPF} = 0 \\ \langle \delta\Psi | \hat{H} - i\partial_t | \Psi \rangle_{coef} = 0 \end{gathered} \tag{2.49}$$

whose solution is:

$$i\dot{A}_J = \sum_L \langle \Phi_J | H | \Phi_L \rangle A_L \tag{2.50}$$

$$i\dot{\boldsymbol{\phi}}^{(k)} = \left(1 - P^{(k)}\right) \left(\boldsymbol{\rho}^{(k)}\right)^{-1} \langle \mathbf{H} \rangle^{(k)} \boldsymbol{\phi}^{(k)} \tag{2.51}$$

where $\boldsymbol{\phi}^{(k)}$ is the vector whose elements are the n_k SPFs associated with the k coordinate, $P^{(k)}$ is the projector onto the subspace spanned by the SPFs, $\boldsymbol{\rho}^{(k)}$ is the density matrix and $\langle \mathbf{H} \rangle^{(k)}$ is the matrix of the mean field operators. The MCTDH equations of motion are norm-preserving and for time-independent Hamiltonians, they are also energy-conserving.

2.3.4 Multi-Layer MCTDH

With the standard MCTDH approach it is possible to handle up to a few dozen of degrees of freedom (50-80); this is an important improvement with respect to conventional time-dependent wavepacket techniques, but it still represents a limit. In order to extend the applicability of the MCTDH approach to substantially larger systems, a formulation called Multi-Layer MCTDH (ML-MCTDH) has been proposed[40].

In the ML-MCTDH approach the basic MCTDH strategy is used to treat each SPF, whose expansion in equation 2.42 is now replaced by a time-dependent multiconfigurational construction:

$$|\phi^{(k)}_{j_k}(Q_k,t)\rangle = \sum_{I}^{m_{j_k}} B^{(k),j_k}_{I}(t)|u^{(k)}_{I}(t)\rangle \tag{2.52}$$

Thus, the SPFs on level 1 (L1), *i.e.* those introduced in the previous sections, in turn contain several SPFs of level 2 (L2):

$$|u^{(k)}_{I}(t)\rangle = \prod_{s=1}^{S} |\nu^{(k),s}_{i_s}(t)\rangle \tag{2.53}$$

so that

$$|\phi^{(k)}_{j_k}(Q_k,t)\rangle = \sum_{i_1=1}\dots\sum_{i_S=1} B^{(k),j_k}_{i_1\dots i_S}(t)\prod_{s=1}^{S}|\nu^{(k),s}_{i_s}(t)\rangle \tag{2.54}$$

The L2 SPFs $|\nu^{(k),s}_{i_s}(t)\rangle$ are expanded onto time-independent basis functions:

$$|\nu^{(k),s}_{i_s}(t)\rangle = \sum_{\alpha} C^{(k),s}_{\alpha,i_s}|\varphi^{(k),s}_{\alpha}\rangle \tag{2.55}$$

The general *ansatz* in the ML-MCTDH method is then:

$$|\Psi(t)\rangle = \sum_{j_1}\dots\sum_{j_M} A_{j_1\dots j_M}(t)\times\prod_{k=1}^{M}\left[\sum_{i_1}\dots\sum_{i_S} B^{(k),j_k}_{i_1\dots i_S}(t)\prod_{s=1}^{S}|\nu^{(k),s}_{i_s}(t)\rangle\right] \tag{2.56}$$

Just like the single particle functions of L1, the ones of L2 are chosen to be orthonormal at every time of the propagation, so that, setting the constraint operator to zero, we obtain:

$$\langle u^{(k)}_{l}(0)|u^{(k)}_{j}(0)\rangle = \delta_{lj}$$
$$\langle u^{(k)}_{l}(t)|\dot{u}_{j}^{(k)}(t)\rangle = 0$$

The equations of motion are derived with the same procedure as in the standard MCTDH, although, now the variation of the overall wavefunction involves the variation with respect to the L1 expansion coefficients A_J, to the L2 expansion coefficients $B^{(k),j_k}_{I}$ and to the L2 SPFs $C^{(k),s}_{\alpha,i_s}$. Thus, the EoMs are:

$$i\dot{A}_J = \sum_L \langle \Phi_J | H | \Phi_L \rangle A_L \tag{2.57}$$

$$i\sum_m \rho^{(k)}_{nm}\dot{B}^{(k)}_{ml} = \langle u^{(k)}_l(t)|(1-P^{(k)}(t))\sum_m \langle H\rangle^{(k)}_{nm}\,|\phi^{(k)}_m(t)\rangle \tag{2.58}$$

$$\sum_s \varrho^{(k),s}_{rp}(t)\dot{C}^{(k),s}_{\alpha,p} = \langle\varphi^{(k),s}_\alpha|(1-P^{(k),s}_{L2}(t)\sum_s \langle\mathcal{H}(t)\rangle^{(k),s}_{rp}\,|\nu^{(k),s}_p(t)\rangle \tag{2.59}$$

where $\rho^{(k)}_{nm}$ is the L1 density matrix, $P^{(k)}(t)$ is the projector onto the subspace spanned by the L1 SPFs, $\varrho^{(k),s}_{rp}(t)$, $P^{(k),s}_{L2}(t)$ and $\mathcal{H}(t)$ are respectively the density matrix, the projector and the mean-field Hamiltonian relative to the L2 space.

In the ML-MCTDH formulation, there are more elements than in the basic MCTDH approach, so that the evaluation of the different elements becomes more complex. For this reason, the Multi-Layer expansion is expected to be more efficient than the standard method only when the number of DOFs is large.

It is important to emphasize that the same strategy showed above can be employed to include a higher number of layers to the MCTDH expansion and that the EoM for the coefficients of each deeper layer have the same form as those for the first two layers.

In Figure 2.2 is reported the so-called "tree" of a 2 layers MCTDH expansion of a wavefunction. The squares containing the letters at the bottom of the tree represent the degrees of freedom, which have been combined in 2D modes. N_P is the number of grid points used for the primitive basis, N_{L1} and N_{L2} are the number of SPFs employed, respectively, in the first and in the second layer of the expansion.

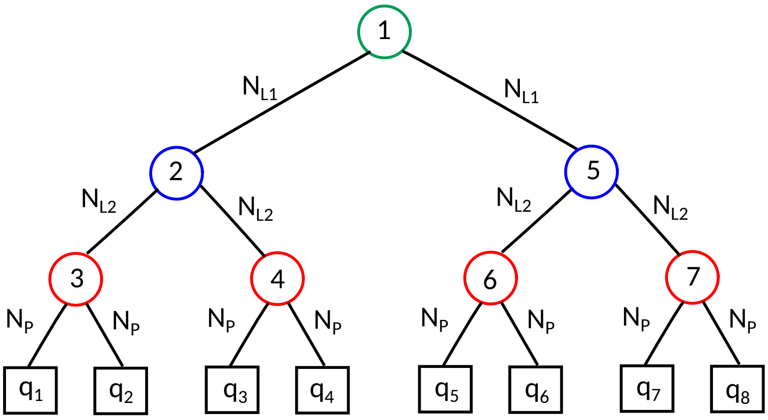

Figure 2.2: Example of ML-MCTDH "tree" for the wavefunction.

2.3.5 Remarks

As shown in the previous sections, the MCTDH approach and its Multi-Layer variant represent essential improvements with respect to traditional quantum dynamical methods in treating large systems within a fully quantum setting. Indeed, although the MCTDH equations of motion are rather complicated, they turn out to be advantageous since there are fewer differential equations to be solved with respect to standard approaches. Moreover, the memory requirement for the wavefunction description is much smaller in MCTDH with respect conventional wavepacket methods. If N is the number of points for the primitive basis representation, in the standard approach the amount of memory required is proportional to N^f. On the other hand, employing the MCTDH method the memory needed is proportional to:

$$fnN + n^f$$

where n is the number of single particle functions for single-combined mode (for simplicity, we assume that the number of SPFs is the same for every mode). In the above expression, the term fnN is relative to the SPFs representation, while the term n^f is relative to the coefficients vector $\mathbf{A}$. Since, in general $n < N$, the MCTDH approach needs much less memory and thus allows larger systems to be treated than conventional time-dependent wavepacket techniques.

However, an important drawback is inherent in the method and it can limit the MCTDH applicability. Indeed, in order to be able to exploit the efficiency of the MCTDH algorithm, it is crucial to avoid the direct evaluation of the Hamiltonian matrix elements $\langle \Phi_J | H | \Phi_L \rangle$ and of the mean field terms $\langle \Psi_j^{(k)} | H | \Psi_l^{(k)} \rangle$, since this would require f dimensional and $(f-1)$ dimensional integrations respectively. These computationally demanding integrations can be avoided only if the Hamiltonian operator has a very simple form and, in particular, if it can be expressed as a product of single-particle operators:

$$H(Q_1, \dots, Q_p) = \sum_{k=1}^{p} \prod_{i=1}^{m} h_i^{(k)}(Q_k)$$

This is usually the case for the kinetic energy, but not for the potential energy operator, which in general does not have the required structure. There exist some procedures to fit a potential energy surface into a product representation, although a certain loss of accuracy can occur. The best option to circumvent this issue is to use an analytic potential term for each combined mode used in the MCTDH expansion, which though is not always feasible. In Chapter 4, we describe our general approach to convert an originally complicated dynamical problem into a form that suits perfect to the MCTDH *ansatz*.

Chapter 3

Isotope effect at vanishing collision energies

In this chapter we report our investigation of the isotope effect in the Eley-Rideal H_2 recombination on graphitic substrate. It is performed employing a time-dependent wavepacket method within the successful rigid and flat surface approximation[41,42]. Furthermore, we exploit a specific implementation that allows us to address collision energies down to 10^{-4} eV $\approx$1.2 K[15]. It makes use of two independent wavepackets propagations which overcomes the typical limitations of standard wavepacket technique. In section 3.1 we will describe in details our two-wavepacket method, in section 3.2 we will show the dynamical models employed and, finally, in section 3.3 we will report our results regarding the isotopic effect.

3.1 Two-wavepackets method

One of the main advantages of employing Time Dependent Wavepacket (TDWP) methods with respect to the Time Independent ones is that from a single calculations information over a range of collision energies can be extracted. As described in section 2.2.3, it is possible to perform the time-energy mapping procedure only when two asymptotic conditions are fulfilled. However, these conditions become limiting in the applicability of Time Dependent methods when the very low energy regime is addressed. Indeed, in this case, the initial wavepacket momentum p_0 is very small, which leads to a narrow momentum wavefunction, since $p_0 \geq \Delta p$. This, in turns, produces a very broad wavepacket in the coordinate space, since $\Delta x \geq \hbar/\Delta p$. Hence, two problems arise: the collision energy range will be particularly narrow and very long grids will be needed. This is clearly unpleasant if one is interested in covering a large range of collision energies with a single calculation and, in addition, wants to keep the grid dimensions reasonably small.

In section 2.2.3, we described why the two asymptotic conditions

(i) it is localized in the asymptotic reagents region;

(ii) it has only *incoming* momentum components.

must be satisfied to perform the time-energy mapping and thus extract the desired information in the standard procedure. Let us now show how to exploit the linearity of the Schrödinger equation and obviate condition (ii) by (independently) propagating two wavepackets in place of one[43]. If $\psi_a(p)$ is a generic (momentum) wavefunction for the motion in the entrance-channel scattering coordinate (to be used in $|\Psi_a\rangle = |\psi_a\alpha\rangle$ as initial state) we may write, under the sole condition (i) above,

$$2\pi\,\langle \mathbf{x}\,|\,\delta(E-H)\,|\,\Psi_a\rangle = \frac{2\pi}{\sqrt{\bar{v}}}\left\{\langle \mathbf{x}|E\alpha+\rangle\,\psi_a(-\bar{p}) - \sum_\beta S^*_{\alpha\beta}(E)\,\langle \mathbf{x}|E\beta+\rangle\,\psi_a(\bar{p})\right\}$$

where $S_{\alpha\beta}(E)$ is the $\beta \to \alpha$ S-matrix element at energy E and the sum runs over the open channels of the reagent arrangement only. The above formula holds for any point $\mathbf{x}$ and can be obtained by noticing that $|\Psi_a\rangle$ localizes in the asymptotic region, since this allows one to use the *asymptotic* expansion of scattering eigenstates contained in the energy-shell projector, $\delta(E-H) = \sum_\beta |E\beta+\rangle\,\langle E\beta+|$. The second term on the r.h.s. of the above expression represents the contribution of the *outgoing* components to the energy shell, *i.e.* the collision processes $\beta \to \alpha$ which do have *outgoing* components in channel α and necessarily overlap with those contained in $|\Psi_a\rangle$. This term disappears, of course, in the traditional approach when condition (ii) is enforced. Now, using two (linearly independent) initial states ($a = 1, 2$) the above equation reduces to a 2×2 linear system in the variables $X = \langle \mathbf{x}|E\alpha+\rangle$ and $Y = \sum_\beta S^*_{\alpha\beta}(E)\,\langle \mathbf{x}|E\beta+\rangle$ which can be easily solved to give

$$\langle \mathbf{x}|E\alpha+\rangle = \frac{\sqrt{\bar{v}}}{\psi_1(-\bar{p})\psi_2(\bar{p}) - \psi_1(\bar{p})\psi_2(-\bar{p})}\times \left[\psi_2(\bar{p})\,\langle \mathbf{x}\,|\,\delta(E-H)\,|\,\Psi_1\rangle - \psi_1(\bar{p})\,\langle \mathbf{x}\,|\,\delta(E-H)\,|\,\Psi_2\rangle\right]$$

This is the desired expression that we were looking for and that can be further re-expressed in terms of time-evolving wavepackets

$$2\pi\,\langle \mathbf{x}\,|\,\delta(E-H)\,|\,\Psi_a\rangle = \int_{-\infty}^{\infty} e^{iEt}\,\langle \mathbf{x}\,|\,\Psi_{a,t}\rangle\,dt$$

using, in general, both the forward and the backward evolutions. The resulting equation generalizes Eq. (2.39) *without* the requirement of condition (ii). It is easy to check that when enforcing this additional condition one wavepacket is sufficient to get the desired scattering eigenstate, and that the above expression does indeed reduce to Eq. (2.39) (just use $\psi_1(\bar{p}) \sim 0$ and consider $\mathbf{x}$ in the product region so that only the $t > 0$ evolution is required).

Finally, it is advantageous in practice to further simplify the expression above by employing time-reversal invariant initial states, *i.e.* states for which $T\,|\Psi_a\rangle = |\Psi_a\rangle$ holds, T being the antiunitary time-reversal operator. Indeed, in this case,

$$\langle \mathbf{x}\,|\,U_t\Psi_a\rangle = \langle \mathbf{x}\,|\,U_tT\Psi_a\rangle = \langle \mathbf{x}\,|\,TU_{-t}\Psi_a\rangle = \langle \mathbf{x}\,|\,U_{-t}\Psi_a\rangle^*$$

holds provided $[T, H] = 0$, and the final working equation becomes

$$\langle \mathbf{x}|E\alpha+\rangle = \frac{1}{2\pi}\frac{\sqrt{\bar{v}}}{i\Im(\psi_1^*(\bar{p})\psi_2(\bar{p}))} \left\{\psi_2(\bar{p})\Re\int_0^\infty e^{iEt}\,\langle \mathbf{x}\,|\,\Psi_{1,t}\rangle\,dt - \psi_1(\bar{p})\Re\int_0^\infty e^{iEt}\,\langle \mathbf{x}\,|\,\Psi_{2,t}\rangle\,dt\right\}$$

thereby involving only the forward evolution. Here, we can choose wavepackets for the translational motion that are 'even' or 'odd' with respect to a reflection on a plane passing through their average position x_0, whose corresponding momentum wavefunctions are given by $\psi_1(p) = \phi_g(p)e^{-ipx_0}$ and $\psi_2(p) = -i\phi_u(p)e^{-ipx_0}$, where $\phi_g(\phi_u)$ is a *real* even (odd) function of p. This reduces the scattering amplitude to

$$\begin{aligned}\langle \mathbf{x}|E\alpha+\rangle =& \frac{1}{2\pi}\sqrt{\bar{v}}e^{-i\bar{p}x_0} \\ & \left\{\frac{1}{\phi_g(\bar{p})}\Re\int_0^\infty e^{iEt}\,\langle \mathbf{x}\mid \Psi_{g,t}\rangle\,dt \right. \\ & \left. -\frac{i}{\phi_u(\bar{p})}\Re\int_0^\infty e^{iEt}\,\langle \mathbf{x}\mid \Psi_{u,t}\rangle\,dt\right\}\end{aligned} \tag{3.1}$$

in which the distinct real/imaginary contributions come from the initially "even"/"odd" time-evolving wavepackets (apart from the irrelevant phase factor $e^{-i\bar{p}x_0}$). This means that the two can be computed and managed independently of each other and stored as independent parts of a single complex array.

In this work we have used Eq. (3.1) in place of Eq. (2.39) in order to perform the time-energy mappings needed to extract energy resolved information from the time propagations. Thus, for example, the probability $P_{\alpha\to\beta}$ for the collisional transition to a product internal state β reads as usual [*]

$$\begin{aligned}P_{\alpha\to\beta}(E) &= 2\pi\,\langle E\alpha+|F^\infty_\beta|E\alpha+\rangle \\ &= \frac{2\pi}{m'}\Im\left\{\Phi^*_{\alpha\to\beta}(R_\infty,E)\frac{\partial\Phi_{\alpha\to\beta}}{\partial R}(R_\infty,E)\right\}\end{aligned}$$

where F^∞_β is the flux operator in the β product channel[†], m' is the product reduced mass and $\Phi_{\alpha\to\beta}(R,E) = \langle R,\beta|E\alpha+\rangle$ has to be known for a large distance R_∞ in the product arrangement. The only difference with the standard approach is that now $\Phi_{\alpha\to\beta}$ is obtained from the amplitude of Eq. (3.1) rather than from Eq. (2.39).

For completeness Table 3.1 summarizes the main formulas used in the standard approach (with the common choice of a Gaussian wavepacket as initial translational state) and in this work. Notice that the 'even' and 'odd' components in our approach correspond to the ground and the first excited state of a harmonic oscillator potential centered in x_0; the choice $\delta' = \sqrt{3}\delta$ for the width appearing in ψ_u guarantees that the two wavefunctions have the same spread Δp in momentum space.

---

[*] See, for example, the Appendix in Ref. 13 for a time-dependent perspective.

[†] The flux operator appearing here, F^∞_β, is defined as the Heisenberg derivative of the projector onto the products internal state β, $F^\infty_\beta = i[H, P^\infty_\beta]$. The latter reads as $P^\infty_\beta = h_\infty(R)\,|\beta\rangle\,\langle\beta|$ where R is the product scattering coordinate (operator), $h_\infty(x) = \{1 \text{ for } x > R_\infty, 0 \text{ otherwise}\}$ is the usual Heaviside function centered on a large distance R_∞ and β labels the relevant product internal state.

	1WP	**2WP**
initial translational state(s)	$\psi_0(x) = (\frac{1}{2\pi\delta^2})^{1/4} e^{-(x-x_0)^2/4\delta^2} e^{-ip_0(x-x_0)}$	$\psi_g(x) = (\frac{1}{2\pi\delta^2})^{1/4} e^{-(x-x_0)^2/4\delta^2}$ $\psi_u(x) = (\frac{1}{6\pi\delta^2})^{1/4} e^{-(x-x_0)^2/12\delta^2} (x - x_0)/\sqrt{3}\delta$
energy weights	$g(E) = \sqrt{8\pi} \frac{mm'\delta}{p} e^{-2\delta^2(p-p_0)^2}$	$g(E) = 2^{5/2}\, 3^{3/4}\, \sqrt{\pi}\delta^2 mm' e^{-4\delta^2 p}$
reduced amplitudes	$\phi_\beta^\infty(E) = \int_0^\infty e^{iEt} \langle R_\infty \beta \vert \Psi_t \rangle \, dt$	$\phi_\beta^\infty(E) = \Re \int_0^\infty e^{iEt} \langle R_\infty \beta \vert \Psi_{g,t} \rangle \, dt +$ $-i\Re \int_0^\infty e^{iEt} \langle R_\infty \beta \vert \Psi_{u,t} \rangle \, dt$

Table 3.1: Comparison between the traditional wavepacket approach for initial-state selected dynamics (1WP) and the one (2WP) adopted in this work. The momentum p is related to the total energy E through $p = \sqrt{2m(E - \epsilon_\alpha)}$, where ϵ_α is the channel energy in the pre-collisional state, and the reaction probabilities are obtained from $P_\beta = \Im \left(\phi_\beta^\infty D_R \phi_\beta^\infty \right) / g(E)$. Here, $D_R \phi_\beta^\infty$ is analogous to ϕ_β^∞, and involves the derivative with respect to the scattering coordinate R evaluated at the large value R^∞. In the table entries m and m' are the reduced masses in the reagent and product arrangement, respectively, δ is the width of the initial wavepacket in the scattering coordinate and x_0 (p_0) the average position (momentum).

3.2 Dynamical models and methodology

To simulate the Eley-Rideal process, we considered a projectile atom of mass m_P and position $\mathbf{x}_P$ which scatters off a chemisorbed target atom of mass m_T and position $\mathbf{x}_T$. In line with our previous work[13,15,25,29,44] a reduction of the number of relevant coordinates is achieved by invoking the rigid, flat surface approximation[41,42]: with this approach the interaction between the two atoms turns out to be invariant both translationally and rotationally around the axis normal to the surface and passing through the target. Thus, the total momentum parallel to the substrate, $\mathbf{P}_{\|}$, and the projection of the total momentum angular momentum on the surface normal, $J_{\mathbf{n}}$, are conserved quantities [‡]. In this simplified 3D description, the phonons of the graphitic surface are neglected and the interaction of the target/incident atoms with the surface is site-independent. On the other hand, the (important) role of the carbon binding the target can be included in the potential energy surface (PES) governing the dynamics in two opposite dynamical limits[11]. In the (substrate) *diabatic* limit the reaction dynamics is supposed to be so fast that the C atom remains frozen in its puckered configuration, whereas in the *adiabatic* limit the substrate atom relaxes instantaneously during the (supposedly slow) recombination process. These limits give rise to two different PESs with rather different exothermicity (3.90 eV in the adiabatic potential and 3.03 eV in the diabatic one), on account of the energy left on the lattice in the diabatic model. Apart from this, though, the energy landscape is rather similar in the two dynamical limits, and displays a downhill (barrierless) route to the molecular product[11].

In modeling the dynamics, the relevant dynamical variables are conveniently chosen to be either the height of the two atoms above the surface (z_P, z_T for the projectile and target atoms, respectively) and their separation on the surface plane (ρ), or the center of mass height $Z = (m_P z_P + m_T z_T)/(m_P + m_T)$, the relative height $z = z_P - z_T$ and ρ (see Fig. 3.1). The first is a "reagent" set of coordinates which best suits to compute energy resolved (in)elastic scattering, atom exchange and trapping probabilities, the second is a "product" set which is ideal for determining the rovibrational populations of the reaction products.

As for the wavepacket propagation, a detailed description of our strategy, which stems from previous work by Lemoine and Jackson[42], has been presented elsewhere[13]. Briefly, for the cartesian coordinates (either (z_T, z_P) or (Z, z)) the wavepacket is represented on a uniform grid, and the pseudospectral strategy involving the use of Fast Fourier Transforms (FFTs) is exploited to move efficiently back and forth between coordinate and momentum space. For the cylindrical coordinate, the discrete Bessel transform (DBT) of Lemoine[45] is used instead, since Bessel functions correctly handle the boundary conditions in the cylindrical radial coordinate and guarantee a numerically stable representation of the kinetic energy operator. The length of the grid along ρ (which sets the maximum value of the classical impact parameter) was set to 13 Å irrespective of the isotopic combination, after carefully testing that this value gives reasonably well converged cross sections. The number of grid points, on the other hand, was chosen differently for each reaction in order to guarantee a common value of the maximum momentum on the ρ axis. The same consideration guided the choice for the grid spacing of the cartesian coordinates, for which an energy cutoff of ~ 5.5 eV was introduced. Time propagation was performed with the split-operator method[46], using

---

[‡] Conservation of the angular momentum gives rise to a partial wave expansion. At normal incidence (the case considered in this work) only the zero angular momentum partial wave is required.

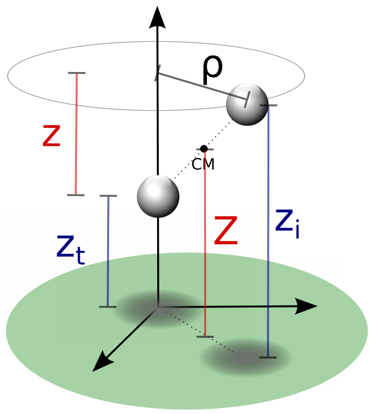

Figure 3.1: Schematic representation of the coordinates adopted for the rigid, flat-surface modeling of the ER recombination dynamics. In blue, the reagent coordinates z_P and z_T, and in red the product coordinates Z and z. In both cases, ρ describes the motion parallel to the surface.

multithreaded routines for FFTs and linear algebra operations which are available in commercial packages.

3.3 Results

In the following, we describe the results of the quantum calculations that we performed on both the adiabatic and the diabatic model developed by Sha *et al.*[11] to describe hydrogen recombination on graphite. We shall use “AonB” to indicate the process in which the A atom from the gas phase (the *incidon*) collides with the chemisorbed B atom (the *targon*):

$$\mathrm{A}_{(g)} + \mathrm{B}_{ad} \rightarrow \mathrm{AB}_{(g)}$$

and consider the possible isotopic substitutions (A,B=H,D), with the target atom in its ground-vibrational state. We first describe the collinear 2D case where the incident atom collides on top the targon. This case shows a clear isotope effect, essentially classical in nature, that can be interpreted by means of a simple impulsive model of the dynamics. Next, we describe the more realistic 3D calculations, where the main constraints of the reduced-dimensional collinear dynamics are removed. In this case reliable reaction cross-sections can be computed, which can eventually be turned into rate constants useful for astrophysical modeling. As we shall see, the most striking feature of relaxing the above mentioned dynamical constraint (often invoked in qualitative descriptions of an Eley-Rideal reaction) is the disappearance of the isotope effect, a signature that the dynamics is less direct than commonly believed.

3.3.1 2D calculations

Fig. 3.2 reports the results for collinear reaction probabilities for the adiabatic potential, showing a clear isotope effect for each collision energy, though qualitatively different depending on the energy range considered. Similar results were obtained for the diabatic model (not shown).

At high collision energy ($E_{coll} > 0.2$ eV) the behavior of the probability curves is rather classical and well captured by a simple, *quasi*-classical impulsive model of the

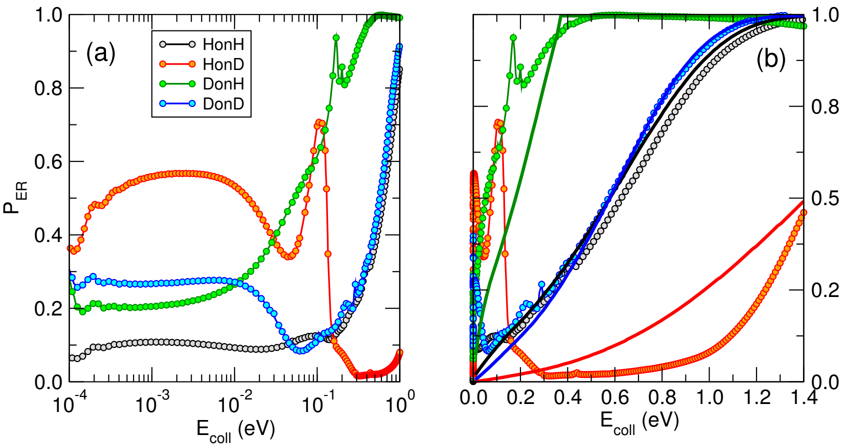

Figure 3.2: ER recombination probabilities from 2D collinear calculations with the adiabatic model, as a function of the collision energy in both log (left panel) and linear (right panel) scale. In (b) the thick lines are the results of the *quasi*-classical impulsive model described in the main text, color coded as the quantum results.

dynamics§. In this model, the projectile with mass m_P and speed $v_P = \sqrt{2E_{coll}/m_P}$ undergoes a binary collision with the target of mass m_T and speed v_T, slows down its motion, and gets captured by the targon after the latter elastically bounces off the surface. Reaction occurs when the final kinetic energy of the targon E_T' is larger than E_R, a dynamical threshold which replaces the details of the dynamics and filters out those trajectories in which the targon is too slow to capture the projectile before leaving the reaction region (*i.e.* the surface).

The final kinetic energy E_T' is determined by the post-collisional target velocity v_T', as results, in turn, by the acceleration provided by the strong H-H interaction and by the above two sequential collisions, that is through the sequence

$$v_T = V - \frac{\mu}{m_T}v \overset{(i)}{\to} V - \frac{\mu}{m_T}\tilde{v} \overset{(ii)}{\to} V + \frac{\mu}{m_T}\tilde{v} \overset{(iii)}{\to} -V - \frac{\mu}{m_T}\tilde{v}$$

where (i) is the acceleration of the colliding pair, (ii) the projectile-targon collision and (iii) the bounce of the targon off the surface, as schematically shown in Figure 3.3. Here $V = (m_P v_P + m_T v_T)/(m_P + m_T)$ is the center of mass speed of the colliding pair, $v = v_P - v_T$ is their initial relative velocity, $\tilde{v} = \sqrt{v^2 + 2D_m/\mu}$ (D_m being the H-H well depth) and $\mu = m_P m_T/(m_P + m_T)$ the reduced mass of the binary system. Hence, the reaction condition $E_T^f(v_T, v_P) > E_R$, determines a domain $\mathcal{V}(v_P)$ of target velocities leading to reaction, and the reaction probability P follows by integrating the distribution of target velocities $g(v)$ over $\mathcal{V}(v_P)$ for each value of the collision energy $E_{coll} = m_P v_P^2/2$:

$$P(v_P) = \int_{\mathcal{V}(v_P)} g(v)dv$$

It then remains to establish what is the most appropriate velocity distribution function $g(v)$ to be used. In the true impulsive limit $g(v)$ would simply be $g(v) = m_T|\phi_\nu(m_T v)|^2$ where $\phi_\nu(p)$ is the momentum space wavefunction of the target initial

---

§We term it *quasi*-classical because it makes use of the quantum distribution of the precollisional targon momenta.

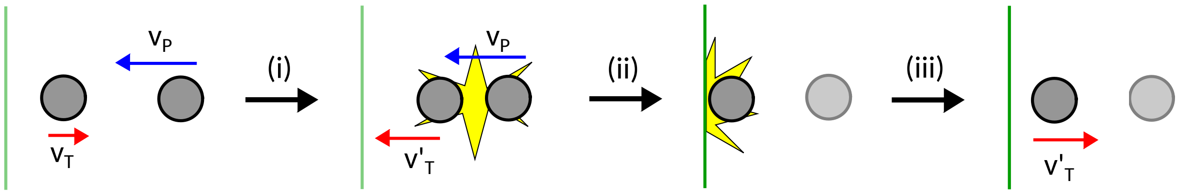

Figure 3.3: Schematic representation of the binary collision dynamics detailed in the main text.

vibrational state ($v = 0$ in our case). However, this limit does not strictly hold in our case since the (high-frequency) target vibration ω_0 sets a bound to the collision time $\tau << \omega_0^{-1}$ which only attains at some eV of collision energy, as can be seen upon noticing that $\tau^2 \approx \frac{1}{2}m_T r_0^2/(E_{coll} + D_m)$, where r_0 is the potential range and $\omega_0^2 = 2\alpha^2 D_T/m_T$ (here, D_T is the targon-surface well depth and α^{-1} is the length scale of the Morse potential used to represent the targon-surface interaction, $\alpha^{-1} \approx r_0$). In other words, the targon atom performs one-two vibrations during the collision, and this makes the above mentioned vibrational distribution particularly inadequate for the lightest targets. To remedy this deficiency, and keep the model as simple as possible, we assume that the appropriate momentum distribution keeps the same shape and average but is bound to describe the increase of the average kinetic energy due to the interaction with the projectile, *i.e.* $\langle \Delta p^2 \rangle = \langle \Delta p_0^2 \rangle + 2m_T D_{eff}$ where D_{eff} is an effective interaction energy and $\langle \Delta p_0^2 \rangle$ is the width of the bare momentum distribution of the target. This amounts to replace the original targon frequency ω_0 determining $\phi_\nu(p)$ with an effective frequency $\omega = \omega_0 + 4D_{eff}/\hbar$.

The results of such modeling for the adiabatic limit are given in Fig. 3.2 as full lines (panel (b)), color coded as the results of the quantum simulations. We set $E_T = 3.4$ eV, $D_m = 4.0$ eV, and $D_{eff} = 0.124$ eV to obtain a reasonable representation of the quantum results. Similar agreement was found for the diabatic model, using the same values of parameters except for D_{eff} which had to be increased to 0.250 eV, in accordance with the larger frequency of the H-graphite motion in the diabatic limit¶.

The model is rather crude but, as can be seen from Fig. 3.2, it captures the main aspects of the dynamics and reproduces the isotope effect observed at high energies. The increase of the reaction probability with increasing m_P/m_T is a consequence of the larger range of targon initial velocities leading to sufficiently fast post-collisional targon atoms. Thus, in this classical energy regime, the largest isotope effect (*i.e.* the largest overall difference in reactivity) occurs at the "threshold" energy of the $m_P/m_T = 1$ case, ~ 0.6 eV in Fig. 3.2. This is the prototypical case where the projectile atom completely transfers its energy *when the targon is at rest* ($v_T = 0$), and thus represents a sort of transition between two different dynamical behaviors.

At low energies ($E_{coll} < 0.2$ eV), on the other hand, the dynamical outcome is largely determined by the details of the interaction potential, and by the quantum character of the dynamics that becomes more and more marked the smaller the energy is. As a consequence, for instance, the HonD combination (barely reactive at high energies) becomes more reactive at low energies than the "references", equal-mass combinations HoH and DonD. Thus, apart from the complicated details of the curves that appear to be tightly bound to the potential model (with sharp resonances dominating the

---

¶For the H-graphite surface oscillator the vibrational wavenumber $\bar{\nu} = \omega_0/2\pi c$ turns out to be 1807 and 2252 cm^{-1} for the adiabatic and diabatic cases, respectively.

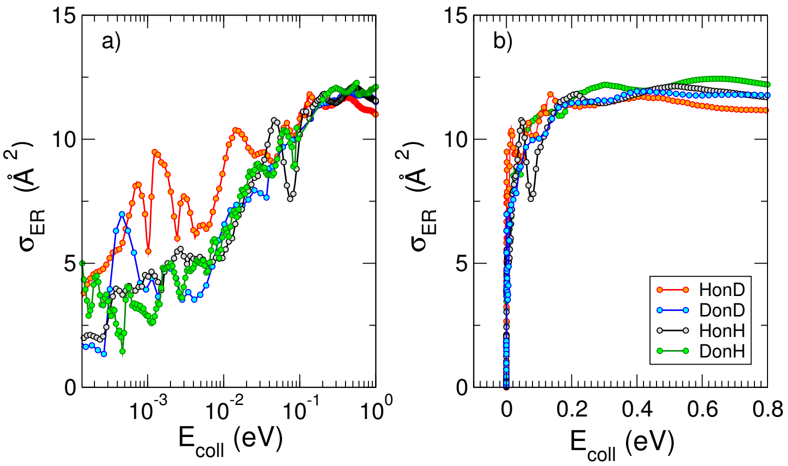

Figure 3.4: Quantum ER cross sections for the four considered reactions as functions of collision energy, obtained with the adiabatic model. Logarithmic and linear scale for panels (a) and (b), respectively.

outcome of the collision process), the only general conclusion that can be drawn for this energy range is that the collinear reaction probability is again highly affected by the mass of the incident and of target atom.

3.3.2 3D calculations

When the third spatial coordinate is added, the reactive cross sections for the Eley-Rideal H_2 recombination σ_{ER} can be computed, as well as the cross sections for non-reactive collisions giving rise to hot-atom species σ_{HA}. In Fig. 3.4, σ_{ER} computed with the adiabatic model is plotted as a function of the collision energy, for the four possible isotope combinations. The general behavior of such cross-sections was already extensively discussed in previous works[11,13,15,29]. At low energies, σ_{ER} decreases as the collision energy decreases, likely because of the strong, short-range interaction potential between the two atoms that prevents low energy projectiles to enter the exit channel if their de Broglie wavelength is larger than the range of the potential. Thus, the cross sections decay to zero for $E_{coll} \rightarrow 0$, though non-monotonically because of the presence of a number of sharp resonances. At moderate-to-high energy range, σ_{ER} reaches large values ($\sim$12 Å^2) in all the considered cases, much larger than those observed on many metal surfaces[47], where σ_{ER} barely reaches 1 Å^2[‖]

Importantly, a rather striking feature of the results shown in Fig. 3.4 is the disappearance of the isotopic effect observed in the collinear case, in agreement with the findings of previous quantum studies at high collision energies on a crude model PES[49]. This suggests that the dynamics is not as direct as the constrained collinear geometry forces it to be, and the reaction mechanism involves some energy "randomization"

[‖] Notice though that a spin-statistical factor of 1/4 applies on graphitic substrates but does not on metals. This is due to the fact that the spin of the chemisorbed H atom is *not* quenched on graphene(ite), see *e.g.* Ref. 48. This feature is rather peculiar of the graphitic substrate where, in contrast to many metals, target hydrogen atoms are found at a larger height above the surface and projectile atoms experience a reduced interaction *with the surface*. At even higher energies (E_{coll} > 0.2 eV), quantum oscillations appear in the cross section, as a consequence of the particular reaction mechanism that - by featuring a rapidly decreasing internal excitation of the product for increasing energies - allows the low-lying product vibrational levels to be selectively populated[13,25,29].

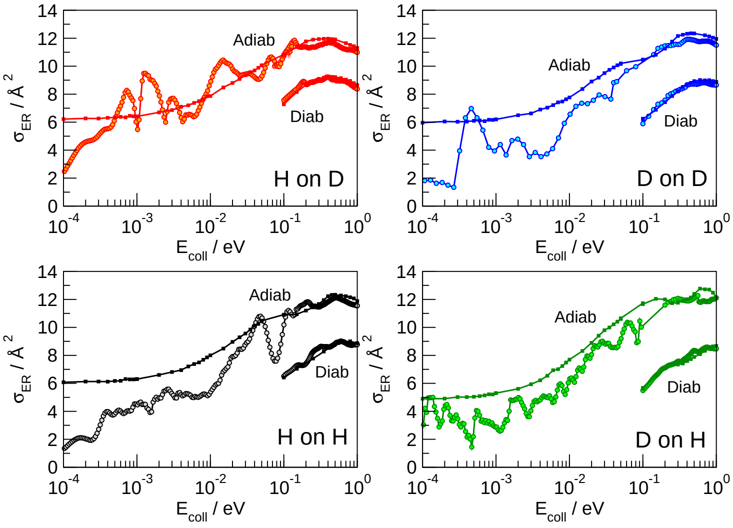

Figure 3.5: Comparison between quantum (circles) and *quasi*-classical results (squares). The size of the squares matches the estimated uncertainties in QCT results.

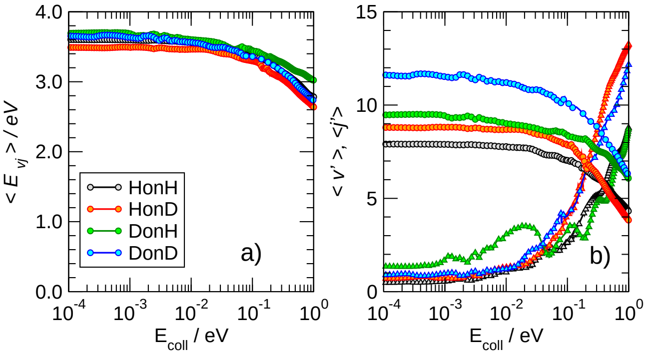

Figure 3.6: Average internal energy (panel a) and average quantum numbers (panel b) of the nascent molecules, as obtained in the adiabatic model. In (b) circles and triangles are for the averaged vibrational and rotational quantum numbers, respectively.

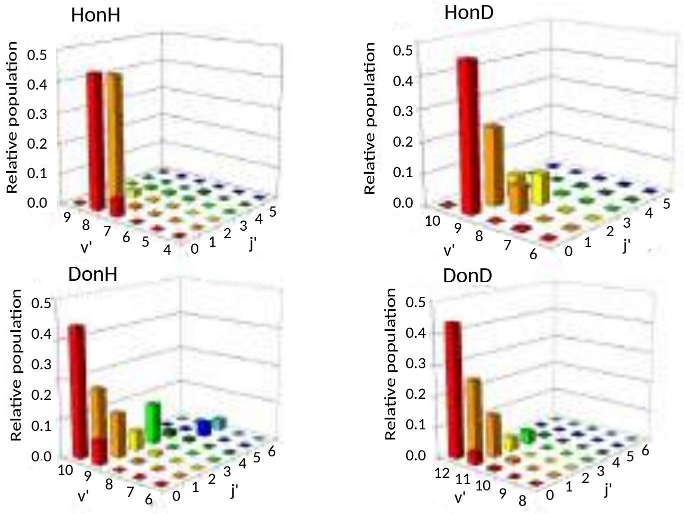

Figure 3.7: Distribution of the rovibrational states ($\nu' j'$) of the ER recombination products, computed at $E_{coll} = 2$ meV in the adiabatic case. Different panels refer to the four isotopic combinations considered.

prior to reaction which hides the effect of the different mass combinations. No real "tendency" can be discerned in the quantum results, and the effect of an unfavorable mass-ratio must be offset by some non-collinear dynamical effects. Such effects though must be of classical nature, since *quasi*-classical trajectory calculations reproduce quantum results very well over a large energy range, and do not show isotope effects either. This is shown in Fig. 3.5, where the QCT cross-sections, reported alongside with the quantum results, differ considerably from the latter only in the very low energy region, and are shown to reproduce rather well (on average) the quantum results. Notice, though, that differently from the quantum results, the limiting classical cross-section at zero energy does not vanish, as expected for a barrierless classical reaction dynamics. For completeness, Fig. 3.5 also shows the results for the diabatic dynamical model (for clarity, only in the energy range where they are more reliable), which present a behavior similar to those obtained in the adiabatic limit, except for an overall reduction of the cross-section which correlates with the reduced exothermicity of the diabatic model.

More information about the reaction dynamics can be obtained by looking at the rovibrational populations of the molecular product. Results for the average internal energy, and average vibrational and rotational quantum numbers are shown in Fig. 3.6 (left). As is evident from that figure, and in agreement with previous studies at high energies[11,13,29], the nascent molecules are internally hot, with *ca.* $3.0 - 3.5$ eV of the reaction exothermicity going in internal excitation of the Eley-Rideal product. In contrast to the behavior at high collision energies, though, internal excitation is mainly vibrational, the average rotational quantum number being rather small in the energy range $10^{-4} - 10^{-1}$ eV [**]. This is not an artifact of the averaging procedure, since the detailed rovibrational distributions are rather peaked around few rovibrational states, as shown in Fig. 3.7 at a representative energy of 2 meV. It is evident from that figure that the nascent molecule mostly appears in either one or two high-ν, low$-j$ rovibrational states.

The behavior of the rotational excitation - which monotonically increases with the collision energy - correlates well with the reaction cross-sections, especially at high energies where the dynamics is classical. The rationale here is that, classically, the angular momentum j of the product molecule correlates well with the entrance orbital angular momentum l of the projectile-targon pair (*i.e.* $j \sim l$), as discussed previously[13], hence $< j >$ can be related to the reaction cross-section through the "maximum" impact parameter b_{max}, $l_{max} = b_{max}\mu v \approx \mu v\sqrt{\sigma_{ER}/\pi}$.

The above considerations suggest that in this realistic 3D case the reaction dynamics is determined by the relative motion in the entrance channel - similarly to what happens for the collinear approach -, but now the *orbital* angular motion of the colliding pair plays a primary role. If it were for the H-H potential only, "capture" of the projectile would not depend on the specific isotope combination, since the "capture radius" ρ_c reads as

$$\rho_c = \sqrt{\frac{n}{n-2}}\sqrt[n]{\frac{n}{2}-1}\sqrt[n]{\frac{\alpha}{E}}$$

when the long-range tail of the projectile-targon potential takes the form $U(r) = -\alpha/r^n$ ($n > 2$). In the gas-phase, this result holds for arbitrarily small collision energies, and determines, *e.g.,* the Langevin capture rate constant that accurately describes low-temperature ion-molecule reactions ($n = 4$). It cannot strictly hold in our problem,

---

[**] The "isotope effect" which is apparent in the average vibrational quantum numbers just reflects the different level spacing of the H_2, HD and D_2 molecules, see Fig. 3.6, panel (a)

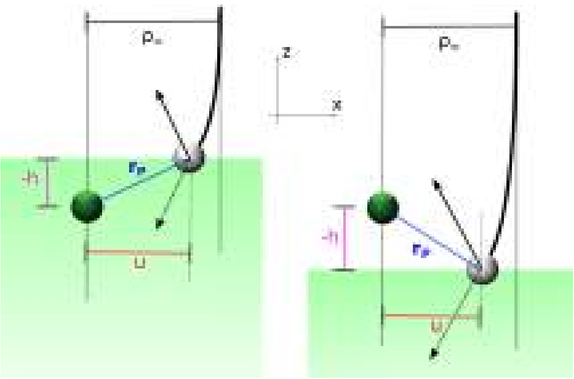

Figure 3.8: Surface-mediated capture. The targon (green balls) is held fixed at height h above the surface ($h < 0$ in the left panel and $h > 0$ on the right) and collision of the projectile (gray balls) with the surface occurs at a position $\mathbf{r}_P = (u, -h)$ in the scattering plane. The arrows indicate the projectile speed before (dashed) and after (thin line) the bounce and ρ_∞ is the impact parameter of the trajectory.

though, since the projectile-targon attraction competes with the projectile-surface interaction (particularly in those large impact parameter trajectories which determine the size of the cross-section) and this competition strongly modifies the energy dependence of ρ_c. The surface *shields* the targon from low-energy projectiles and, conversely, *focuses* higher energy trajectories towards the target, thereby reducing (increasing) the capture radius at low (high) collision energies.

This is best seen in a simple model where the targon is held fixed at a height h ($h > 0$ when the target atom lies above the surface) and the surface is represented by a hard wall that has the simple effect of reverting the normal component of the projectile velocity, $v_z \to -v_z$ (see Fig. 3.8). In this model, the orbital angular momentum of the projectile undergoes a sudden change $l \to l'$ upon collision with the surface, namely

$$\Delta l^2 = l'^2 - l^2 = -4uhv_x v_z$$

if $\mathbf{r}_P = (u, -h)$ represents the projectile position in the scattering plane (referenced to the targon) at the time of the impact and $\mathbf{v} = (v_x, v_z)$ its speed[††] (Fig. 3.8). Since for an attractive interaction $v_x v_z \geq 0$ (≤ 0) holds to the right (left) of the targon atom, the change Δl is *negative* for a targon *above* the surface and *positive* otherwise. As a consequence, the effective barrier ruling the capture process decreases (increases) when the target lies above (below) the surface and, correspondingly, the capture radius becomes larger (smaller) than its gas-phase value[‡‡].

Real surfaces are not hard walls and display a more intricate competition with the targon field of forces than the one outlined above. Nevertheless, for the large-impact parameter trajectories we are interested in, the picture above is mainly modified only to the extent that the height of the turning point becomes energy dependent, the smaller the collision energy is the higher the "altitude" where the projectiles reverts its motion. In particular, the location of the physisorption wall (relative to the chemisorpton well)

[††] If needed, v_x and v_z can be expressed in terms of $\mathbf{r}_P$ and the constants of motion in the targon field, namely as $v_x = (-v_r u + v_\omega h)/r_P$ and $v_z = (v_r h + u v_z)/r_P$ where $v_r = \sqrt{2\left(E - l^2/2mr^2 - U(r)\right)/m}$ and $v_\omega = -l/mr_P v_\omega$ ($U(r)$ being the projectile-targon spherical potential).

[‡‡] The case $h = 0$ with the targon "in the plane" of the surface does not modify l, hence in this case the rotational angular momentum of the product molecules exactly matches the angular momentum of the reagents. This is the conservation of the angular momentum alluded to above.

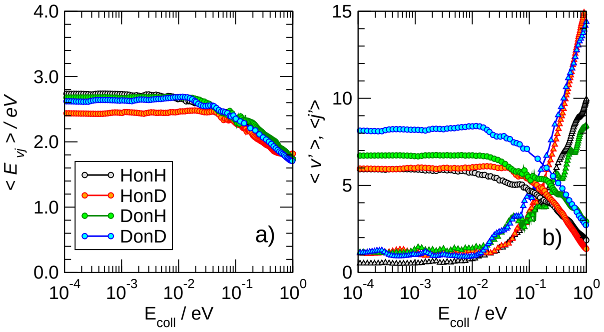

Figure 3.9: Average internal energy (panel a) and average quantum numbers (panel b) of the nascent molecules, as obtained in the diabatic model. In (b) circles and triangles are for the averaged vibrational and rotational quantum numbers, respectively.

determines the limiting "height of the targon" at vanishing collision energies. Its negative value considerably reduces the size of the gas-phase capture radius and makes it finite at zero energy.

Overall, even though this argument does not explain the precise form that σ_{ER} takes as a function of energy, it does suggest a reason why the reaction cross-section does *not* depend on the mass combination of the colliding pair: reaction is dominated by the capture process - *i.e.* collisions are mainly glancing rather than head-on - and this is only marginally affected by isotopic substitutions.

Fig. 3.9 shows the average internal energy, and the average vibrational and rotational quantum numbers of the product molecules, as obtained from the diabatic model, similarly to Fig. 3.6 for the adiabatic limit. As can be seen from this figure, the dynamics is very similar in the two models, the only difference being the smaller reaction exothermicity described in the diabatic limit, which determines a corresponding decrease of the internal energy of the products. In other words, the change in the reaction energetics does not affect the translation energy of the products, only its internal content. This highlights the importance of including energy relaxation to the surface into the reaction dynamics in order to accurately assess the internal excitation of the product molecule - the "missing energy" of the diabatic model is just a crude way to describe such energy transfer, energy is stored in the puckered carbon atom and released to the substrate upon molecular formation.

In contrast with the ER reaction, the cross section for the formation of hot-atom species is characterized by a strong isotopic effect. This is shown in Fig. 3.10, which reports σ_{HA} as a function of the energy of the incident atom for the four isotope combinations. As evident from the figure, when the incident atom is hydrogen (black and red curves), σ_{HA} barely reaches 2 Å^2, whereas when the incident atom is deuterium (green and blue curves), the cross section significantly increases and can be as large as $\sim$ 16 Å^2. In our dynamical model, the HA formation corresponds to the situation in which the reactive event ends with a large momentum along ρ and with the incident atom bound (normal to the surface) in the physisorption well. Hence, the larger deuterium cross sections are simply a consequence of the larger number of final physisorbed bound states available to the incident atom. The well is in fact only ~7.75 meV in our model potential and supports only one state for H and two for D, but similar results are expected for a more realistic physisorption well depth[19,20]. In any case, and irrespective of the mass combination, σ_{HA} quickly vanishes for E$_{coll}$ > 10^{-2} eV, when projectile energy becomes too large for trapping in the physisorption well.

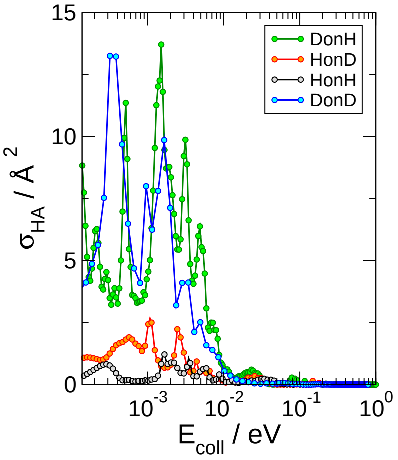

Figure 3.10: Quantum cross sections for the "hot-atom" formation for the four considered isotopic combinations as a function of collision energy, computed within the adiabatic model.

A word of caution is appropriate here. Our dynamical model is not entirely adequate to simulate hot-atom formation, since within the flat surface approximation a free motion along ρ implies that *both* incidon and targon might be moving along the direction parallel to the surface. This situation should *not* be allowed in our case where the target atom is held in place by a strong, directional bond with the surface. The model though does capture the main effects of the presence of the target atom - *i.e.* the increase of surface corrugation and energy accommodation -, hence we are confident that it correctly describes the "initial" trapping cross section. After this step it is the dynamical response of the C-H bond that determines whether the trapped incidon species interacts again with the targon or is left free to move on the surface. In this respect, our results can be considered the limiting case where the targon rebounce (a CH bending) is slow enough to not affect the projectile atom after the first collision.

3.4 Summary and Conclusions

In this work we have used quantum dynamics to investigate isotope effects in collision induced processes involving hydrogen/deuterium atoms on graphite at the cold collision energies typical of the ISM. We focused on chemisorbed target atoms and analyzed Eley-Rideal reaction and trapping dynamics for the four possible isotopic combinations, using a time-dependent "two-wavepacket" method and *quasi*-classical dynamics.

Our simulations show that ER hydrogen formation is affected by isotopic substitution only in the collinear approach. In this case, the P_{ER} curves for different mass combinations result from an intricate interplay of kinematic and quantum effects but, at high energies, are well rationalized by a simple *quasi*-classical impulsive model of the dynamics. In the 3D case, on the other hand, this marked isotopic effect disappears and the four considered reactions show almost identical trends and values for σ_{ER}, likely as a consequence of the fact that "capture" of the projectile does not depend on the specific mass combination. This suggests two different "mechanisms" for product formation, namely through either "head-on" or "glancing" collisions. The first presents a marked isotopic effect but has a limited weight in the cross-section while the second has the largest weight but is less sensitive to mass effects. In contrast to Eley-Rideal reaction, the mass of the projectile does strongly influence hot-atoms formation. σ_{HA} reaches considerably large values (~ 16 Å^2) when the atom from the gas phase is the heaviest, and barely attains 2 Å^2 for hydrogen. This is a direct consequence of the increased number of bound states in the physisorption well that can host the trapped incidon. This effect, likely occurring on different surfaces as well (*e.g.* those covered by ice mantles), might be responsible for some deuterium enrichment in the ISM grains, with impact on deuterium fractionation* through surface reactions. It is worth noticing though that such fractionation is mainly a gas-phase effect related to the efficient 'primary' fractionation in H_3^+ ($[H_2D^+]/[H_3^+] \sim 10^4[HD]/[H_2]$), and the primary role of surfaces is through accretion, which depletes H_2D^+-destroying molecules (notably CO) and makes formation of higher deuterated species D_2H^+ and D_3^+ possible[50,51].

Comparison of the results obtained in the adiabatic and in the diabatic limits suggests that the reaction is only marginally affected by the lattice dynamics - *ab initio* molecular dynamics simulations including the lattice dynamics indeed found cross-section values intermediate between these two limits[26] - but for a correct description of the internal excitation of the product molecules it is essential to include energy transfer to the carbon atom holding the targon in place. Work is currently in progress to lift this static surface approximation and describe the dynamical role that the substrate carbon atoms (and the ensuing energy dissipation to the surface) plays in the reaction.

---

[*] That is, the observation of deuterated molecules well in excess (up to 10^{11}) the statistical predictions based on the cosmic D/H ratio $\sim 10^{-5}$.

Chapter 4

Dissipative effects

In this chapter the dynamics of H_2 formation through the Eley-Rideal mechanism on a graphitic surface is investigated with a fully quantum approach and exploiting a dynamical model that, for the first time, allows us to include the substrate effects. Thus, the energy transfer through the surface is consistently described, overcoming the limits of the rigid, flat surface approximation. In particular, we apply a system-bath model, in which the two recombining hydrogen atoms and the carbon atom involved form the main system, while the rest of the graphitic substrate is represented with an independent oscillator bath. High-dimensional wavepacket calculations are performed using the multi-layer Multi-Configuration Time Dependent Hartree method, in the collision energy range 0.2-1.0 eV; we focused on the collinear reaction with a surface at 0 K. We will describe the system-bath dynamical model in section 4.1 end the details of our calculations in section 4.2. Finally, in section 4.3 we will present our results.

4.1 System-bath model

4.1.1 Generalized Langevin Equation

The motion of a particle interacting with a macroscopic environment and exposed to an arbitrary potential, *i.e.* a Brownian particle, is classically described by the Generalized Langevin Equation (GLE):

$$M\ddot{x}(t) + M\int_{-\infty}^{+\infty} \gamma(t-t')\dot{x}(t')dt' + V'(x(t)) = \xi(t) \qquad (4.1)$$

Here, x is the particle position and M its mass, $\gamma(t-t')$ is called *memory kernel*, V is an arbitrary potential and ξ is a random force; the dot denotes the derivative with respect to time t, while the prime denotes the derivative with respect to x. Equation 4.1 means that three different forces are exerted on the system:

- a friction force, described by the memory kernel $\gamma(t-t')$, which results in effects of energy dissipation;
- a Gaussian stochastic force $\xi(t)$, which results in effects of energy fluctuation;
- a deterministic force given by the potential $V(x)$.

The friction force and the stochastic force originate from the interaction between the system end the environment, the so-called "bath", they have opposite effects and at the equilibrium they balance out. Indeed, they are closely related through a fluctuation-dissipation theorem of the second kind holds, so that:

$$\langle \xi(t)\xi(0)\rangle = \frac{\gamma(|t|)k_B T}{m} \tag{4.2}$$

where $\langle \ldots \rangle$ denotes the average over the canonical equilibrium, T is the temperature and k_B is the Boltzmann constant. $\gamma(t)$ is in turn determined by the spectral density of the environmental coupling $J(\omega)$, defined as:

$$J(\omega) = m\omega \Re\widetilde{\gamma}(\omega) \tag{4.3}$$

so that, by virtue of the Kramer-Kronig relations, $J(\omega)$ completely determines the memory kernel and, hence, the dynamics described by the GLE[22,52].

Equation 4.1 has been validated and deeply investigated employing classical dynamics simulations which can deal with a huge number of DOFs, so that both the main system and the bath can be explicitly included in the calculations. However, the situation becomes much more complicated when a quantum approach is needed. Indeed, including all the necessary degrees of freedom in a quantum dynamical simulation, the so-called *brute force approach*, is impossible because of the well known dimensionality curse. Thus, the main efforts in this area are addressed to find reasonable reduced description of the dynamics and to obtain reasonable master equations. In this approach, the environmental DOFs are traced out and the main system undergoes to a dissipative, non-unitary dynamics. Nevertheless, even with this reduced dynamics strategy additional approximations are often needed to gain manageable equations. An interesting alternative possibility is represented by the so-called *unitary system-bath approaches*, in which the complex environment is modeled as a simpler surrogate whose DOFs can be explicitly included in the quantum dynamical calculations[53].

4.1.2 The Independent Oscillator model

The Independent Oscillator (IO)[54] or Caldeira-Leggett[55] model allows one to determine a model Hamiltonian for a quantum system coupled to an environment; the Hamiltonian is analytically treatable, is able to mimic the realistic physical phenomenon and, most importantly, allows one to deal with quantum mechanics.

The model is very simple: the quantum main system is surrounded by a heat bath composed of a large number (eventually infinite) of "heat-bath particles"; each one of them is linked to the main system with a spring characterized by a frequency ω_α. The Hamiltonian of such a system is given by:

$$\begin{aligned} H =& \frac{p^2}{2m} + V(x) + \sum_\alpha \left[\frac{p_\alpha^2}{2m_\alpha} + \frac{1}{2} m_\alpha \omega_\alpha^2 \left(q_\alpha - \frac{c_\alpha}{m_\alpha \omega_\alpha^2} x \right)^2 \right] \\ =& \frac{p^2}{2m} + V(x) - \sum_\alpha c_\alpha q_\alpha x + \sum_\alpha \frac{1}{2} \frac{c_\alpha^2}{m_\alpha \omega_\alpha^2} x^2 + \sum_\alpha \left(\frac{p_\alpha^2}{2m_\alpha} + \frac{m_\alpha \omega_\alpha^2}{2} q_\alpha^2 \right) \\ =& \frac{p^2}{2m} + V(x) - \sum_\alpha c_\alpha q_\alpha x + \sum_\alpha \frac{1}{2} \Omega^2 x^2 + \sum_\alpha \left(\frac{p_\alpha^2}{2m_\alpha} + \frac{m_\alpha \omega_\alpha^2}{2} q_\alpha^2 \right) \end{aligned} \tag{4.4}$$

Here, the sums run over the number of heat-bath particles, c_α are the coupling coefficients of the bath to the system and the system-bath coupling has a bilinear form where each oscillator in the bath is coupled to the main system $\sum_\alpha c_\alpha q_\alpha x$.

In order to prove that the Hamiltonian of the IO model is equivalent to the GLE in equation 4.1, we derive the Heisenberg equations of motion from equation 4.4 for the system degree of freedom:

$$\begin{aligned} \dot{x} &= \frac{[x,H]}{i} = \frac{p}{m} \\ \dot{p} &= \frac{[p,H]}{i} = -V'(x) + \sum_\alpha c_\alpha q_\alpha - m_\alpha \Omega^2 x \end{aligned} \tag{4.5}$$

and for the heat bath DOFs:

$$\begin{aligned} \dot{q_\alpha} &= \frac{[q_\alpha,H]}{i} = \frac{p_\alpha}{m_\alpha} \\ \dot{p_\alpha} &= \frac{[p_\alpha,H]}{i} = -m_\alpha \omega_\alpha^2 q_\alpha + c_\alpha x \end{aligned} \tag{4.6}$$

The pairs of equations 4.5 and 4.6 can be expressed as two second order differential equations, eliminating the momenta variables:

$$m\ddot{x} = -V'(x) + \sum_\alpha c_\alpha q_\alpha - m_\alpha \Omega^2 x \tag{4.7}$$

$$\ddot{q_\alpha} = -m_\alpha \omega_\alpha^2 q_\alpha + c_\alpha x \tag{4.8}$$

In order to obtain the solution for the system dynamics $x(t)$, we solve first for the dynamics of the bath DOFs $q_\alpha(t)$ (equations 4.8) and substitute the solution in equation 4.7. We choose t_0 as the initial moment, corresponding to the initial conditions for the bath particles $\{q_\alpha^0, v_\alpha^0\}$. From equations 4.8 we find the solution for the bath particles $q_\alpha(t)$:

$$\begin{aligned} q_\alpha(t) =& \frac{c_\alpha}{m_\alpha \omega_\alpha^2} x(t) + \left[q_\alpha^0 - \frac{c_\alpha}{m_\alpha \omega_\alpha^2} x(t_0) \right] \cos(\omega_\alpha(t-t_0)) + \\ &+ \frac{v_\alpha^0}{\omega_\alpha} \sin(\omega_\alpha(t-t_0)) - \frac{c_\alpha}{m_\alpha \omega_\alpha^2} \int_{t_0}^t \cos(\omega_\alpha(t-t'))\dot{x}(t')dt' \end{aligned} \tag{4.9}$$

Now, we can substitute the solution 4.9 in equation 4.7 to find the expression for $x(t)$; the result is:

$$\begin{aligned} m\ddot{x} =& -V'(x) + \sum_\alpha c_\alpha \left\{ \left[q_\alpha^0 - \frac{c_\alpha}{m_\alpha \omega_\alpha^2} x(t_0) \right] \cos(\omega_\alpha(t-t_0)) + \frac{v_\alpha^0}{\omega_\alpha} \sin(\omega_\alpha(t-t_0)) \right\} + \\ &- \int_{t_0}^t \left(\sum_\alpha \frac{c_\alpha}{m_\alpha \omega_\alpha^2} \cos(\omega_\alpha(t-t')) \right) \dot{x}(t')dt' \end{aligned} \tag{4.10}$$

where we find the three forces acting on the main system that appear in the Generalized Langevin Equation. Indeed, upon taking the limit $t_0 \to -\infty$ and the ensemble average over the initial condition of the bath* we can identify

$$\xi(t) = \sum_\alpha c_\alpha \left\{ \left[q_\alpha^0 - \frac{c_\alpha}{m_\alpha \omega_\alpha^2} x(t_0) \right] \cos(\omega_\alpha (t - t_0)) + \frac{v_\alpha^0}{\omega_\alpha} \sin(\omega_\alpha (t - t_0)) \right\}$$

with the zero-average, Gaussian random force and

$$\gamma(t) = \Theta(t) \sum_\alpha \frac{c_\alpha}{m_\alpha \omega_\alpha^2} \cos(\omega_\alpha t)$$

with the memory kernel appearing in 4.1, thereby proving that the Independent Oscillator Hamiltonian is equivalent to the GLE.

We stress out that in equation 4.4 the total potential relative to the main system only is:

$$V^{tot}(x) = V(x) + \sum_\alpha \frac{c_\alpha^2}{2 m_\alpha \omega_\alpha^2} x^2 \tag{4.11}$$

where $\sum_\alpha \frac{c_\alpha^2}{2 m_\alpha \omega_\alpha^2} x^2$ is the so-called counter term, which is introduced to avoid possible unpleasant effects on the potential energy ground state. Indeed, for a bilinear system-bath coupling and in absence of the counter term, the minimum of the potential can be shifted and, in the most tragic situations, there could be no lower bound to it.
In absence of the counter term, the total potential is given by:

$$V^{tot}(x, q_1 \dots q_N) = V(x) + \sum_\alpha + \frac{1}{2} m_\alpha \omega_\alpha^2 q_\alpha^2 - x \sum_\alpha c_\alpha q_\alpha \tag{4.12}$$

so that the minimum of V^{tot} with respect to the bath DOFs is given by:

$$\frac{dV^{tot}}{dq_\alpha} = 0 \; \Rightarrow \; q_\alpha^{min} = \frac{c_\alpha^2 x^2}{m_\alpha \omega_\alpha^2} \tag{4.13}$$

Substituting q_α^{min} in 4.12 we obtain:

$$V^{tot}(x, q_1^{min} \dots q_N^{min}) = V(x) - \sum_\alpha \frac{1}{2} \frac{c_\alpha^2 x^2}{m_\alpha \omega_\alpha^2} = V(x) - \Delta V(x) \tag{4.14}$$

which corresponds to a shift in the potential minimum. In order to get rid of this issue, we introduce the counter term in equation 4.11, so that the total potential becomes:

$$V^{tot}(x, q_1 \dots q_N) = V(x) + \sum_\alpha \frac{1}{2} m_\alpha \omega_\alpha^2 \left(q_\alpha - \frac{c_\alpha}{m_\alpha \omega_\alpha^2} x \right)^2$$

and, repeating the above procedure, we get:

$$\begin{aligned} q_\alpha^{min} &= \frac{c_\alpha x}{m_\alpha \omega_\alpha^2} \\ V^{tot}(x, q_1^{min} \dots q_N^{min}) &= V(x) \end{aligned}$$

---

*This requires that the equilibrium state of the bath refers to the uncoupled environment with the system frozen at its initial position and it is actually feasible in classical mechanics only.

The undesirable effect has been fixed.

The bath defined as described in this section is characterized by a spectral density $J_{IO}(\omega)$ with the following form:

$$J_{IO}(\omega) = \frac{\pi}{2} \sum_{\alpha} \frac{c_{\alpha}^{2}}{m_{\alpha}\omega_{\alpha}^{2}} \delta(\omega - \omega_{\alpha}) \tag{4.15}$$

In general, the above expression can reproduce any spectral density and, thus, any GLE dynamics. Indeed, any spectral density can be expressed as:

$$J(\omega) = \int d\omega' J(\omega')\delta(\omega - \omega') \cong \sum_{\alpha} \Delta\omega J(\omega_{\alpha})\delta(\omega - \omega_{\alpha})$$

where in the second step, we introduce a uniform discretization of the frequencies, $\omega_{\alpha} = \alpha\Delta\omega$. For $J_{IO}(\omega)$ to be identical to $J(\omega)$ it is necessary that:

$$\Delta\omega J(\omega_{\alpha}) = \frac{\pi}{2} \sum_{\alpha} \frac{c_{\alpha}^{2}}{m_{\alpha}\omega_{\alpha}^{2}}$$

and from the above equation, we obtain the expression for the coupling coefficients c_{α}:

$$c_{\alpha} = \sqrt{\frac{2m_{\alpha}\omega_{\alpha}\Delta\omega J(\omega_{\alpha})}{\pi}} \tag{4.16}$$

In this way, the bath has the same fluctuative-dissipative properties of the environment described by $J(\omega)$ and the model Hamiltonian can reproduce the dynamics expressed by the equivalent GLE. However, considering discretized frequencies implies a truncation in the time domain, so that the strict equivalence between equation 4.1 and Hamiltonian 4.4 holds only for a finite time range, whose upper bound is called *Poincaré recurrence time* t_{rec} and is given by:

$$t_{rec} = \frac{2\pi}{\Delta\omega} \tag{4.17}$$

Moreover, in practical applications, only a finite number of harmonic oscillators can be used. This means that a frequency cut-off $\omega_c = N\Delta\omega_{\alpha}$ is introduces which implies a discretization in the time domain given by $\delta t = \frac{2\pi}{\omega_c}$, so that it is not possible to represent dynamics with a time-scale shorter than δt.

Thus, in order to perform proper simulations, we need to ensure that the recurrence time t_{rec} is longer and that the time discretization δt is shorter than the time-scale of the tackled problem and that the bath samples the right spectral range of $J(\omega)$.

4.1.3 Spectral density of the H-graphite system

The spectral density contains all the information about the environmental coupling so that it fully characterizes the GLE and the equivalent Hamiltonians of the Independent Oscillator model. Thus, in order to be able to exploit the methods based on the GLE and its quantum equivalent, it is crucial to find a way to compute the spectral density.

Considering a classical harmonic Brownian motion with $V = \frac{1}{2}m\omega_0^2 s^2$, $J(\omega)$ results to be related to the autocorrelation function of the system position in the frequency domain $\widetilde{C}(\omega)$, which is defined as:

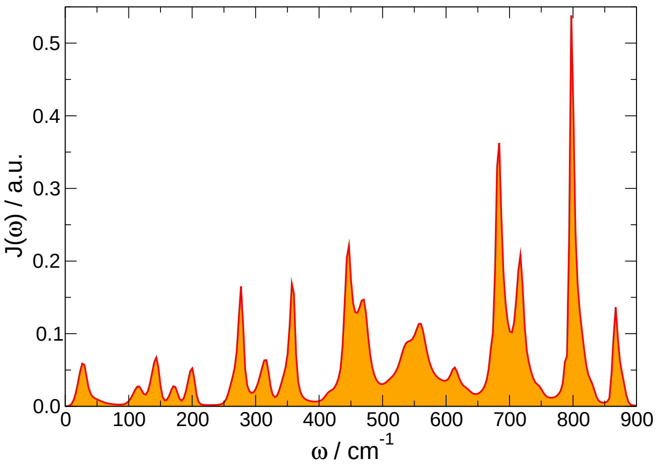

Figure 4.1: Spectral density of the environmental coupling relative to the system composed of a chemisorbed H atom onto a graphitic substrate.

$$\widetilde{C}(\omega) = \int_{-\infty}^{+\infty} C(t)e^{i\omega t}dt = \int_{-\infty}^{+\infty} \langle x(t)x(0)\rangle\, e^{i\omega t}dt$$

where $x(t)$ is the main system position. The relation between the spectral density and the autocorrelation function is expressed as:

$$\frac{1}{2}\omega\widetilde{C}(\omega) = \frac{k_B T}{m}\Im\left(\frac{1}{\omega_0^2 - \omega - i\omega\widetilde{\gamma}(\omega)}\right) \tag{4.18}$$

Since $C(t)$ can be easily obtained from classical dynamical simulations of the system at equilibrium, $J(\omega)$ can be derived in terms of frequency-dependent autocorrelation function inverting equation 4.18[52].

For this work, the spectral density of interest is the one relative to a graphitic surface with a chemisorbed hydrogen atom bound to it. It was derived for our previous investigation on the sticking dynamics of a H atom onto the same substrate and it is shown in Figure 4.1[22].

4.2 Theory

4.2.1 Dynamical models

The bath-system model described in the previous sections is perfectly suitable for performing theoretical investigations of the Eley-Rideal recombination of H_2 on graphitic surfaces with the introduction of the dissipative effects due to the substrate.

In order to simulate the title reaction, we represent a projectile atom, the so-called “incidon”, which collides with a chemisorbed target atom, the so-called “targon”, at normal direction, since here we consider the collinear configuration only; the target atom is bond to a carbon atom which is initially at its puckered position. These three atoms form the main reactive system. The C atom is in turn linearly coupled with a bath of harmonic oscillators which represents the graphitic substrate. The Hamiltonian for the system-bath dynamics has the form of an Independent Oscillator

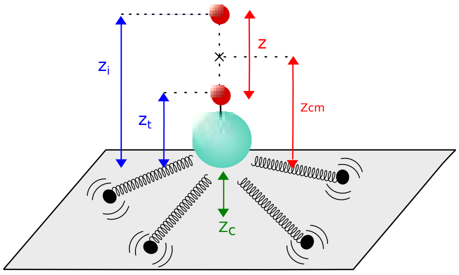

Figure 4.2: The "reagents" set of coordinates in blue and the "products" set of coordinates in red.

(IO) Hamiltonian (equation 4.4) and the working expression is:

$$H = \frac{p_i^2}{2m_i} + \frac{p_t^2}{2m_t} + \frac{p_C^2}{2m_C} + V(z_i, z_t, z_C) + \sum_k \frac{p_k^2}{2m} + \frac{m\omega_k^2}{2}\left(x_k - \frac{c_k z_C}{m\omega_k^2}\right)^2 \qquad (4.19)$$

Here z_i, p_i and m_i represent respectively the height above the surface, the momentum and the mass of the incidon; the same notation has been used for the targon t and the binding carbon atom C. These dynamical variables form the "reagent" set of coordinates shown in blue in Figure 4.2, which is appropriate to investigate the reaction probabilities. On the other hand, the "products" set of coordinates (in red in Figure 4.2) suits better to the calculation of the vibrational populations of the reaction products; in this case, the dynamical variables are the center of mass height $Z_{CM} = \frac{m_i z_i + m_t z_t}{m_i + m_t}$ and the relative height between the two atoms $z = z_i - z_t$. Furthermore, in equation 4.19 x_k and p_k denote respectively the position and momentum of the k-th harmonic oscillator in the bath; the mass m is chosen to be the same for each oscillator, without loss of generality. Importantly, the frequencies ω_k and the coupling coefficients c_k sample the spectral density $J(\omega)$ characterizing the Langevin dynamics of the binding carbon that was derived for our investigation of the hydrogen sticking on the same substrate[21,22]. We employed a standard sampling for $J(\omega)$ with evenly spaced frequencies with spacing $\Delta\omega$, so that the coupling coefficients c_k are computed with equation 4.16.

Finally, $V(z_i, z_t, z_C)$ is an analytic 3D potential describing the interactions within the main system. We built it starting from the well established, rigid-surface LEPS potential from Sha *et al.*[11] -here limited to the collinear configuration- and modifying it introducing a term V_{CH} in order to explicitly include the perpendicular motion of the carbon atom:

$$V(z_i, z_t, z_C) = V_{diab}^{LEPS}(z_i - z_C, z_t - z_C) + V_{CH}(z_t, z_C) - V_t(z_t - z_C) \qquad (4.20)$$

Here, V_{CH} is the DFT-based potential by Kerwin at al.[56] which describes the sticking of an hydrogen atom on a graphitic substrate, the coupling between the reacting hydrogens and the C atom is given in a surface-oscillator (SO)-like form (first term on the r.h.s.) and V_t is a counter-term avoiding double counting. V_{diab} describes the recombination of two H atoms in the diabatic limit, *i.e.* with the binding carbon frozen at its puckered configuration. consistently with the SO-like form of the coupling (potential of type A in the paper by Sha *et al.*[11]).

Overall, the total potential $V(z_i, z_t, z_C)$ resembles the main features of the LEPS potential: the reactive process has a downhill barrierless path, apart for a spurious, tiny barrier ($\sim$ 10 meV high) in the entrance channel, which does not affect the dynamics in the collision energy range that we explored ($E_{coll} > 0.2$ eV). The energetics of the process provided by the adopted potential energy surface (PES) is reasonably good. The chemisorption well for the H atom is -0.66 eV deep and the equilibrium heights above the surface plane for the target and the binding carbon are respectively of 1.48 Å and 0.37 Å . The binding energy for H_2 is 4.58 eV and the reaction exoergocity is 3.9 eV (not corrected for the zero point energy).

Starting from our full dynamical model corresponding to Hamiltonian in equation 4.19, we devised lower dimensional models, 3D and 2D, in order to investigate the effects of the substrate on the dynamics. In the 3D model, the binding carbon id dynamically active, while the bath is removed; in this way, we can understand whether the energy dissipation affects the reaction dynamics. The 2D model, on the other hand, resembles the diabatic limit, with the C atom fixed at its puckered configuration throughout the reactive process, neglecting any dynamical effects of the substrate.

4.2.2 Wavepacket dynamics

We performed several quantum dynamical calculations with the Multi Layer Multi-Configuration Time-Dependent Hartree[37,57,58] method, which is particularly efficient when propagating many DOFs. In this method the wave function is expanded as a combination of Hartree products of time-dependent single-particle functions of combined modes (*i.e.* groups of the original variables), like in the original MCTDH method, but the latter are further expanded in a MCTDH fashion, using smaller dimensional modes. The procedure can be arbitrarily repeated to generate a 'tree' until reaching the lower level of description, which is in terms of a primitive (time-independent) grid for each coordinate. Expansion coefficients and single-particle functions are then evolved in time following variational equations of motion, and the wavefunction can be analyzed for the quantities of interest.

We performed our calculations using the powerful MCTDH Heidelberg package[59], which is the first implementing the ML-MCTDH method for arbitrary trees[60]. Fig.s 4.3 and 4.4 give a representation of the ML-MCTDH wavefunctions employed in our simulations. We used a bath of 32 harmonic oscillators, uniformly spaced in frequency in the range 0-900 cm^{-1}, since this number is large enough to guarantee a Poincaré recurrence time t_P much larger than the reaction dynamics ($t_P \sim 1200$ fs). As a consequence of the uniform sampling, the coupling coefficients c_k, were set according to Eq. 4.16, using the spectral density $J_C(\omega)$ derived in our previous work on the sticking dynamics of H atoms on graphite[22] . As for the single-particle functions of our wavefunctions we chose to group the degrees of freedom of the reactive system in a single 3D combined mode, while the bath DOFs were arranged in 2D modes within multilayer expansions, which were designed differently for the 'reagent' (Figure 4.3) and for the 'product' (Figure 4.4) set of coordinates. We found the results rather insensitive to the adopted ML tree (likely because the reaction dynamics is much faster than bath relaxation, see below) though the second scheme, Figure 4.4, where the system couples directly to near-resonant oscillators, turns out to be computationally more efficient. As for the primitive grids, we used a Hermite basis for the harmonic oscillators DOFs $\{q_k\}$ (see bottom of Fig.s 4.3-4.4), and uniform grids for the system degrees of freedom (Table 4.1).

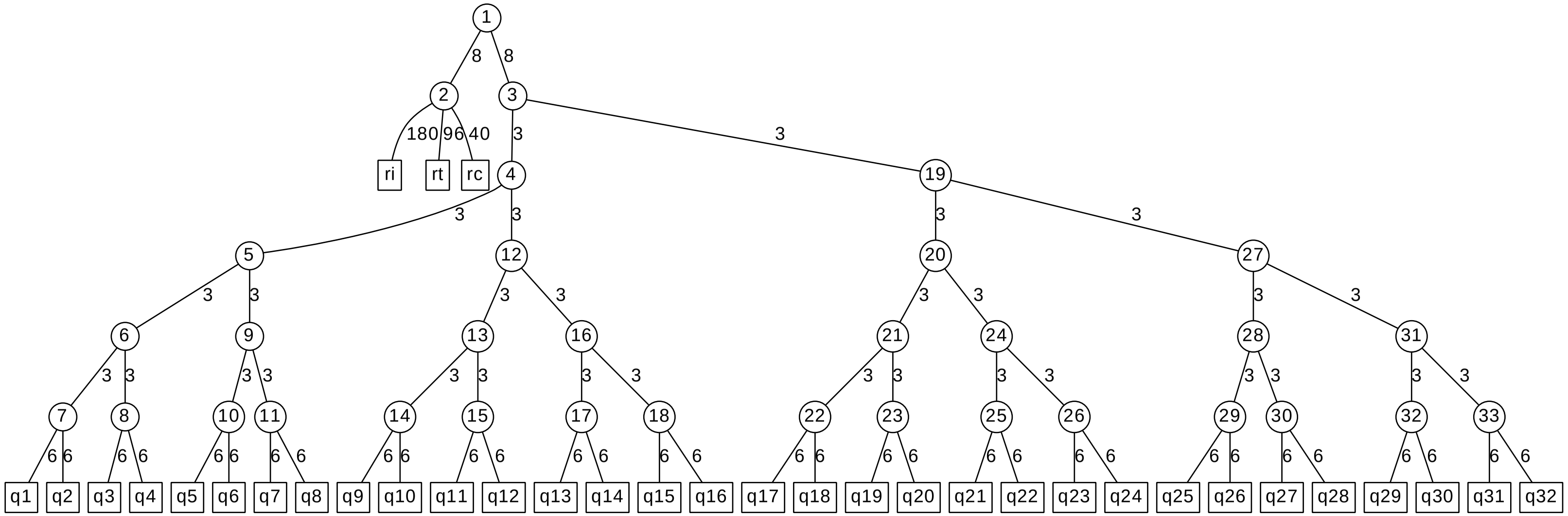

Figure 4.3: Multi Layer tree used in the reagent set of coordinates. Here, ri, rt and rc are respectively z_i, z_t and z_C.

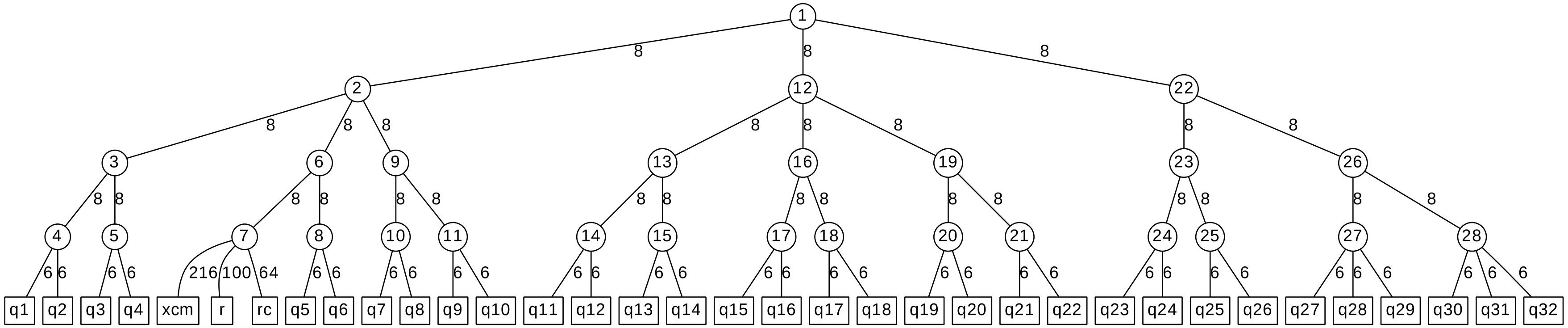

Figure 4.4: Same as Figure 4.3, but for the product set of coordinates. Here, xcm and r are respectively Z_{cm} and z.

The initial wavefunctions were of the product form, a wavefunction for the projectile times a wavefunction for the rest, and represented a hydrogen atom scattering off a target hydrogen atom equilibrated with a T_s=0 K surface. The projectile wavefunction was chosen to be a Gaussian wavepacket with an average initial momentum directed towards the surface and sufficiently narrow in momentum space to be representative of the corresponding average energy. The 'target' wavefunction, on the other hand, was the ground-state wavefunction describing a H atom bound to the C atom that in turn coupled to the bath. The whole initial wavefunction was obtained from a relaxation run (*i.e.* propagation in imaginary-time) that used a modified Hamiltonian, namely

$$H^{\text{relax}} = \frac{(p_i - p_0)^2}{2m_i} + \frac{\hbar^2}{2m_i\Delta z^2}(z_i - z_0)^2 + \\ + \frac{p_t^2}{2m_t} + \frac{p_C^2}{2m_C} + V_\infty(z_t, z_C) + \sum_k \left[\frac{p_k^2}{2m} + \frac{m\omega_k^2}{2}\left(q_k - \frac{c_k z_C}{m\omega_k^2}\right)^2\right] \quad (4.21)$$

where p_0 is the average momentum of the projectile, Δz is the spatial width of the Gaussian wavepacket and $V_\infty(z_t, z_C)$ is the asymptotic interaction potential, $V_\infty(z_t, z_C) = \lim_{z_i \to \infty} V(z_i, z_t, z_C)$. This form of the Hamiltonian ensures that the desired initial state is the long time limit of the imaginary-time dynamics, irrespective of the coordinates used to represent the wavefunction. Once obtained the correct initial state, real time propagation was performed using the Hamiltonian of Eq. 4.19, adding only cubic absorption potentials at the edges of the (z_i, z_t) grid to avoid artificial reflections of the wavepacket and allow analysis of the results. Time-energy mapping of the flux was not feasible for our high-dimensional wavepacket calculations and, as mentioned above, we resorted to sufficiently narrow wavepackets that were representative of the average energy of interest. We checked, though, in the 2D and 3D simulations that such procedure gives results in excellent agreement with the energy-resolved total reaction probabilities obtained from the time-energy mapped flux along z_t in the 'reagent' set of coordinates.

Total reaction probabilities were computed in the 'reagent' set of coordinates using the average flux absorbed along z_t. Calculations in the 'product' set, on the other hand, were used to extract the vibrational populations of the product molecular hydrogen, as well as the average internal and kinetic energy of the molecule and the energy transfer to the substrate. In particular, since the latter are referenced to the reacted fraction of the wavepacket only, we employed standard product projection operators h —*i.e.*, $h(\mathbf{x}) = 1$ for $\mathbf{x}$ in the product channel and $h(\mathbf{x}) = 0$ otherwise— to evaluate expectation values normalized to a reactive event,

$$E_R[\Psi] = \frac{\langle\Psi|h\hat{R}h|\Psi\rangle}{\langle\Psi|h|\Psi\rangle}$$

Here R is the observable of interest, *e.g.* the internal and kinetic Hamiltonians of the H_2 molecule, the projector onto a vibrational state of H_2, etc..

We also performed classical and quasi-classical trajectories in the microcanonical ensemble, using the system-bath Hamiltonian in Eq. 4.19 in the 'reagent' set of coordinates. In these classical calculations the bath was made of 500 harmonic oscillators, which were arranged uniformly in the same range as above (0-900 cm^{-1}) with coupling coefficients sampling the spectral density $J_C(\omega)$. This gave rise to a recurrence time much larger than in the quantum simulations (t_P ~18 ps) that allowed us to perform

	2D	3D	Full
z_i^{min}	2.5	2.5	2.5
z_i^{max}	18	16	21
n_i	144	144	180
z_t^{min}	1.0	1.0	1.0
z_t^{max}	12.0	12.0	12.0
n_t	108	108	96
$Z_{Z_{CM}}^{min}$	2.0	2.0	2.0
$Z_{Z_{CM}}^{max}$	20	20	20
$n_{Z_{CM}}$	225	225	216
z^{min}	0	0	0
z^{max}	20	20	20
n_z	144	256	100
z_C^{min}	-	-1.5	-1.5
z_C^{max}	-	2.2	2.2
n_C	-	64	40

Table 4.1: Left (*min*) and right (*max*) bounds of the grids (in atomic units) and number of points (n_x) used in the 2D, 3D and full calculations, for both ”reagent” (z_i and z_t) and ”products” (Z_{CM} and z) coordinates.

unrestricted checks of convergence with respect to propagation times. The initial states of the trajectories were chosen differently according to the recipes for either a classical or a quasi-classical dynamics. In the first case, the bath was prepared with an equilibration run at a given surface temperature (1 K, 5 K, 100 K and 300 K), using Langevin dynamics to obtain the desired temperature. In the quasi-classical simulations at 0 K, on the other hand, the zero point energy of the substrate was taken into account, and the initial state of the trajectories was chosen by sampling the quantum ground state of the surface. Specifically, the equilibration step was replaced by a random pick of coordinates and momenta from the phase-space orbits of the normal modes of the surface (*i.e.* the target hydrogen atom, the binding carbon and the harmonic bath) at the energy of their (quantum) ground-state. For both classical and quasi-classical trajectories, in order to evaluate the H_2 energy components and the amount of energy transfer to the substrate, we computed the average energies considering the reactive trajectories only.

4.3 Results

In the following, we present the results of the quantum, the quasi-classical and the classical calculations that we performed in order to investigate the Eley-Rideal H_2 recombination on graphite. Results from the three different substrate approximations are also shown.

Figure 4.5 gives an overview of the results of a typical quantum dynamical simulation: here the one-dimensional densities along z_C (left panel) and z_t (right panel) are reported at different times — from bottom to top, well before the collision, at the collision instant and after the collision — for a projectile energy of $\sim$ 1.1 eV. As it can be seen for that figure, the wavepacket, initially localized to describe the CH moi-

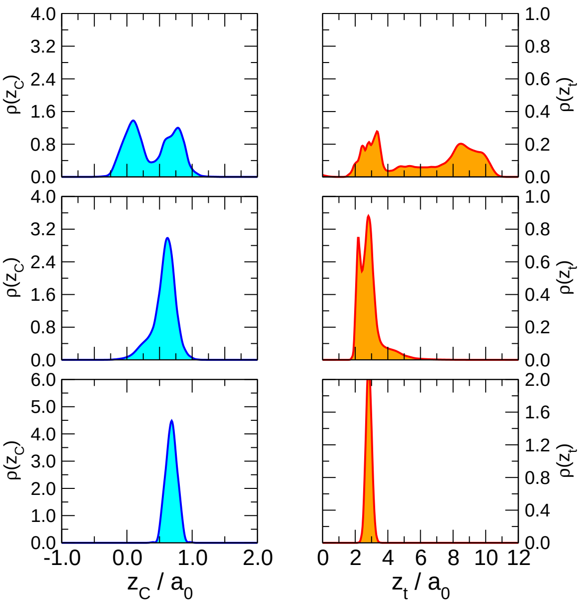

Figure 4.5: Time evolution of the reduced densities along z_C (left panel) and z_t (right panel) obtained from the quantum simulations using the full dynamical model at different times, t = 0, 30 and 60 fs from bottom to top. The latter correspond respectively to a time before, during and after the bouncing of the projectile off the target. The data refer to a collision energy of $\sim$ 1.1 eV.

ety above the surface, broadens and distorts during the collision and split afterward to describe a reacted (small z_C and large z_t) and a reflected (larger z_C and small z_t) fraction. This is best seen in Figure 4.6, where the same one-dimensional densities are plotted over time, though now the wavepacket is absorbed at the grid edges and disappears from the grid. For the chosen initial state the collision occurs after about 35 - 40 fs of propagation, and appears to be a rather direct process, with no evident signature of multiple rebounds. The target atom presses the binding C atom on the surface, the latter recoils and eventually pushes the H atom towards the projectile. In this reactive fraction z_t moves away from the surface and the binding carbon, now performing large amplitude oscillations around the equilibrium position of the flat surface, starts relaxing and decays towards its final equilibrium position z_C=0. This relaxation process starts soon after the product molecule left the surface, and is signaled by the shrinking of the left branch of the wavepacket pictured in Figure 4.6, left panel. At the same time, energy is transferred to the rest of the lattice, and is distributed to the bath oscillators in a way which is determined by the coupling. This can be seen in Figure 4.7, which reports the average number of phonons in the bath during the dynamics, along with the spectral density $J_C(\omega)$ governing the system-bath coupling. Relaxation of the C atom — *i.e.* the unpuckering of the surface — is rather fast, and is completed in tens of fs, in accordance with the similar behavior found for the surface mode describing block oscillations of the CH moiety in the H-graphene system[22]. This is due to the fact that the frequency of the carbon atom vibrator normal to the surface (834 cm^{-1}) is well within the spectral range of the bath.

As for the reflected fraction of the wavepacket, on the other hand, it describes a situation where both z_C and z_{H_t} remain close to their initial equilibrium value, only slightly vibrationally excited as is evidenced by the broadening of the wavepacket. Here, relaxation involves the carbon-hydrogen stretching, it is yet fast (few ps)[22,61] but

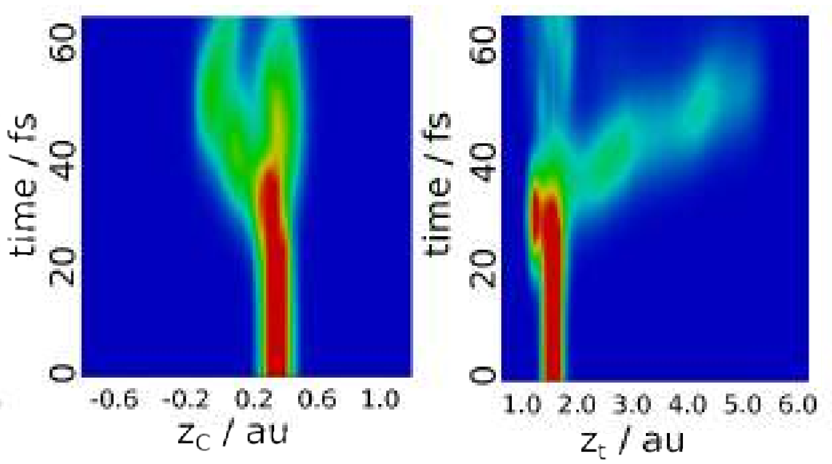

Figure 4.6: Time evolution of the reduced densities along z_C (left panel) and z_t (right panel) from the same calculations of Fig. 4.5.

occurs on a much longer time-scale than the one relevant for the reaction dynamics.

4.3.1 Reaction probabilities

Figure 4.8 shows the reaction probabilities P_{ER} as functions of the collision energy, as obtained from the quantum, the quasi-classical and the classical calculations using the full-dimensional model of Eq.4.19. Classical simulations were performed at two different surface temperatures, a high value (300 K) and a low value (1 K) mimicking scattering off a surface in its classical ground state.

The probability curves share a similar trend, featuring a minimum at intermediate values of the collision energy, whose exact position depends on the type of calculation. This minimum results from the smoothening of the low-T_s classical results, which show no reaction in a sharply defined energy range, ~0.2-0.7 eV. The decrease of P_{ER} for decreasing energy is common to many other calculations[15,44] but its increase at low energies is a peculiar feature risen by the adopted potential, at odds with previous works[13,15,16]. This effect is also present in the results of the reduced-dimensional 2D calculations (see below) that made use of the same LEPS potential of previous works[11], except for the refinements of the CH interaction detailed in Eq. 4.20. Hence, it is most likely due to some minor change in the PES at short range and it shows up here because, in the absence of a barrier, the shape of the PES determines the (collinear) reaction probabilities to a large extent[44].

From Figure 4.8 it is evident that the classical results are only qualitatively similar to the quantum ones, though the latter always fall in between the limits provided by the (high temperature) classical simulations and the quasi-classical results. Hence, even though the agreement is not as good as for the sticking case[21], classical mechanics does a reasonably good job in describing the reaction, *provided the lattice and the binding C atom are given some energy that can mimic the quantum fluctuations of the substrate.* In fact, as mentioned above, the classical data at the lowest temperature considered (1 K) show a different behavior, with sharp transitions between 100% reaction and no reaction at all, suggesting that the initial condition of the substrate plays a primary role in determining the outcome of the collision.

Further insights into the reaction dynamics are obtained by comparing different

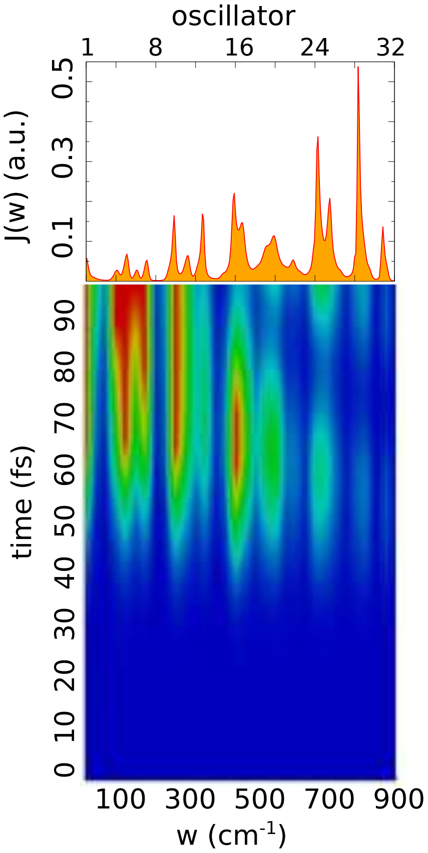

Figure 4.7: Average excitation number of the bath oscillators. The data refer to the same collision energy of Fig. 4.5.

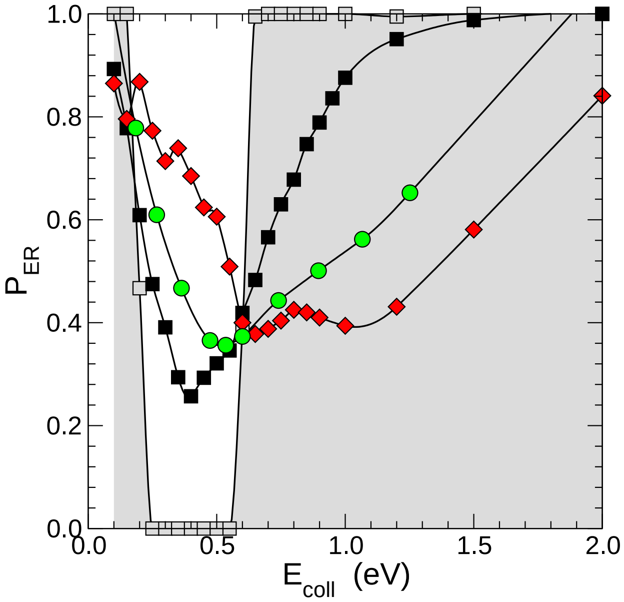

Figure 4.8: Eley-Rideal reaction probabilities as functions of the collision energy $E_{\rm coll}$, as obtained with classical (squares), quasi-classical (diamonds) and quantum (circles) calculations using the full Hamiltonian of Eq. 4.19. Classical results refer to two different surface temperatures, namely gray symbols (and shaded area) for $T_s = 1$ K and black symbols for $T_s = 300$ K.

dynamical models in the quantum setting. Figure 4.9 shows the results obtained from two reduced-dimensional quantum calculations (the 2D and the 3D model described in section 4.2.1) along with those of the full dimensional model, Eq. 4.19. This figure unambiguously shows that the main effect of a movable substrate comes from the carbon atom dynamics. The results of the rigid substrate case (2D case, black line in the plot), though having a similar trend, compare only qualitatively with the results of the calculations in which C was allowed to move. In particular, the carbon dynamics shifts — roughly rigidly — the reaction probability curve to higher energies and thus leads to an increase of P_{ER} at low energies, while for $E_{coll} \sim 0.5$ eV the trend is reversed.

Importantly, there is almost no difference between the results from the 3D and the full calculations (respectively, red line and green circles in Figure 4.9), thereby suggesting that the reaction dynamics is so fast, compared to the C atom dynamics, that the fate of the C atom after the impact of the two Hydrogens — *i.e.* whether it quickly relaxes or vibrates indefinitely — has little effect on the outcome of the collision. This result partly justifies the numerous studies which kept the substrate frozen: the lattice atoms play only a *passive* role in the dynamics, with the important exception of the binding C atom which does affect the reactive event and needs to be explicitly described to obtain a correct description of the reaction.

It is worth noticing in this context that attempting to reduce the effect of the C atom to a static one — *i.e.* by averaging 2D *diabatic* results over the appropriate distribution of the initial position of the C atom, according to what is known as 'phonon sudden approximation'[62,63] — is only partially successful. In fact, because of the SO-like coupling employed in our modeling (Eq. 4.20), here the sudden approximation to the dynamics would precisely reduce to a single frozen-surface calculation with the potential $V(z_i, z_t, z_C^{\rm eq})$, and Figure 4.9 shows that this is only qualitatively similar to the exact result. Even worst, an adiabatic approximation where the 2D PES implicitly

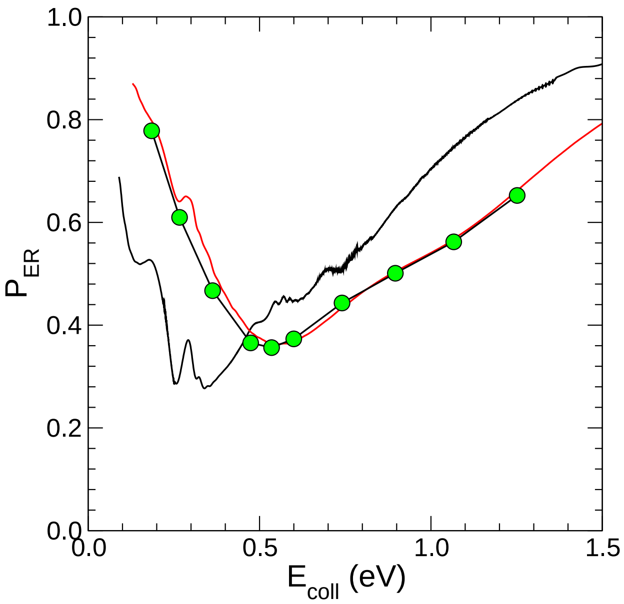

Figure 4.9: Quantum reaction probabilities as functions of the collision energy, as obtained from reduced-dimensional calculations (black and red lines for 2D and 3D models, respectively) and from the full dimensional calculations using the Hamiltonian of Eq. 4.19 (see text for details).

describes a C atom that instantaneously relaxes during the dynamics, is not even in qualitative agreement with the results of Figure 4.9 (not shown). This is mainly due to the strong interaction between the two hydrogen atoms which makes the reaction dynamics fast irrespective of the initial energy of the projectile, and thus the failure of the adiabatic approximation likely extends to the vanishingly small collision energies which are more relevant for the ISM.

4.3.2 Energy transfer

Next, we consider the amount of energy transferred to the surface. We are interested in the energy released for each reactive event, since this gives valuable information on the reaction dynamics.

The appropriate definition of energy transfer is a bit subtle, since the substrate prior to collision (the hydrogenated surface) differs from the substrate after a (reactive) collision has occurred (the bare surface). In addition, if we want to compare unambiguously quantum and classical results, we must be careful in handling zero-point energies, where present. To this end, we define the internal energy of the substrates as $E_{\mathrm{X}}^{\mathrm{int}} = E_{\mathrm{X}} - E_{\mathrm{X}}^{0}$, where X = CH,C labels the hydrogenated and the bare surface, respectively, and 0 stands for the corresponding ground-state, being it quantum or classical depending on the setting. Then, the energy transferred to the surface reads simply as

$$\Delta E_s = E_{\mathrm{C}}^{\mathrm{int}} - E_{\mathrm{CH}}^{\mathrm{int}} \tag{4.22}$$

In fact, the overall energy partitioning can be described as follows. The pre-collisional energy is given by $E_i = E_{\mathrm{coll}} + E_{\mathrm{CH}}^{\mathrm{int}} + E_{\mathrm{CH}}^{0}$, where $E_{\mathrm{CH}}^{\mathrm{int}}$ is the internal energy appropriate to the equilibrated hydrogenated surface ($\equiv 0$ in the case considered in this work), whereas the post-collisional one reads as $E_f = \epsilon_{\mathrm{K}} + \epsilon_{\mathrm{int}} + E_{\mathrm{mol}}^{0} + E_{\mathrm{C}}^{\mathrm{int}} + E_{\mathrm{C}}^{0}$, where

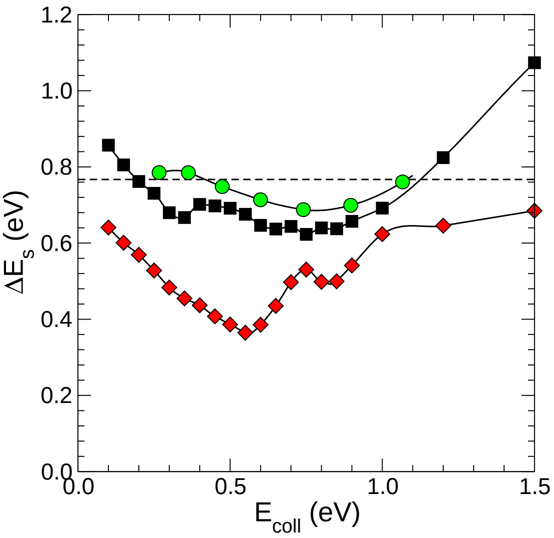

Figure 4.10: Energy transferred to the substrate per reaction event, as obtained from classical (T_s=300 K, squares), quasi-classical (diamonds) and quantum (circles) calculations at different collision energies. The horizontal line is the reference 'puckering energy' which is stored in the CH bond before reaction has occurred.

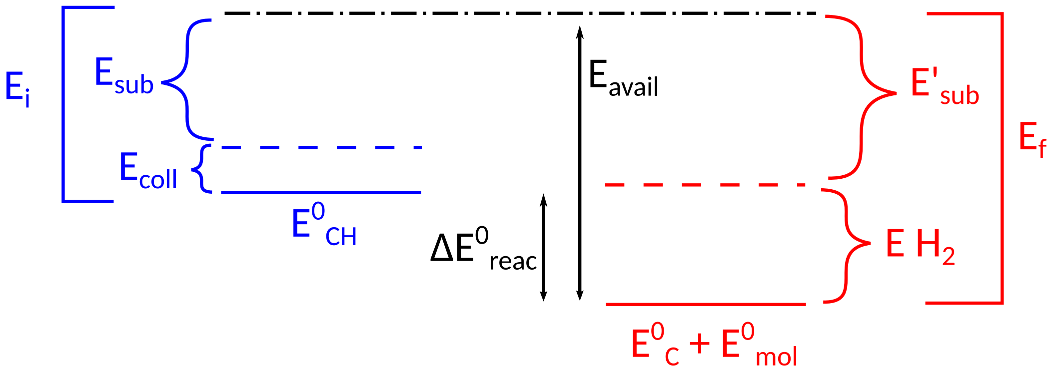

Figure 4.11: Schematic representation of the energetics scheme relative to the formation of H_2 on graphitic surface through Eley-Rideal mechanism.

ϵ_K and ϵ_{int} are the kinetic and internal energy of the product molecule, respectively, and E^0_{mol} the ground-state energy of H_2. Since

$$\Delta E^0_{\text{reac}} = E^0_{\text{C}} + E^0_{\text{mol}} - E^0_{\text{CH}} \tag{4.23}$$

is (minus) the reaction exothermicity, the energy at disposal of the products reads as

$$E_{\text{avail}} = -\Delta E^0_{\text{reac}} + E_{\text{coll}} \tag{4.24}$$

and appears correctly partitioned between the surface and the molecular components

$$E_{\text{avail}} = \Delta E_s + \epsilon_{\text{K}} + \epsilon_{\text{int}} \tag{4.25}$$

A schematic representation of the energetics scheme of the reaction is shown in Figure 4.11

In practice, application of Eq. 4.22 requires determination of the ground-state energy of the substrate for both X=C and X=CH. In the quantum case this is accomplished with imaginary-time propagations using the substrate-only Hamiltonian, whereas for the classical case this just requires a structural optimization of both the hydrogenated and the bare surface. Normal mode analysis of the equilibrium configuration further provides the necessary vibrational frequencies for defining the zero-point energy appropriate for the quasi-classical calculations (for X=CH this is in any case necessary to set the initial state of the substrate).

The results of such calculations in the energy range considered above are reported in Figure 4.10 for both the quantum, the classical (at 300 K) and the quasi-classical simulations. All the curves have a similar trend, slightly decreasing and then increasing for increasing collision energy, and the energy transferred to the substrate is approximately between 0.5 eV and 1.0 eV. In particular, the most reliable quantum results depend only weakly on the collision energy and give a value of ΔE_s very close to the energy stored in the surface puckering (~0.8 eV, dashed horizontal line in Figure 4.10). This is consistent with the previous findings: the reaction dynamics is fast compared to the C atom dynamics and most of the energy stored as lattice deformation remains in the substrate. Hence, even though the dynamics of the C atom is essential for the correct description of the reaction (see sec. 4.3.1), the binding substrate atom exchanges little energy with the reacting partners. In fact, this 'energy exchange' is essentially from the substrate to the H atoms and is $\sim$ 0.1 eV at most for $E_{\mathrm{coll}} \sim$ 0.7-0.8 eV, *i.e.*, where ΔE_s lies clearly below the nominal value of the puckering energy.

Surprisingly, Figure 4.10 also shows that purely classical mechanics performs better than QCT in reproducing the energy transfer, and CT results closely follow the quantum ones in the energy range 0.2-1.0 eV. This is most likely due to the approximate way in which zero-point energies are handled in QCT.

Overall, our findings show that the energy transferred to the lattice is significant, and that formation of hydrogen molecules considerably heats the interstellar grains. To give an idea, as already observed previously[64], we can estimate from this value the temperature increase per reaction event of a typical carbonaceous interstellar grain. This follows from the low temperature Debye expression of the specific heat, $c_v = 12\pi 4/5 \times n \times k_B \times (T/\Theta)^3$, where $n \sim 4/35.3 \times 10^{30}$ m^{-3} is the number density of carbon atoms in graphite and $\Theta_D \sim$400 K is its Debye temperature. For a typical grain 1 μm^3 sized at T = 5 K we find that formation of a single H_2 molecule increases the temperature of the grain by 2.2×10^{-4} K, a rather large value for a single molecular event. Overall, one should further consider the energy dissipated in chemisorbing the first H atom (~0.7 eV with our potential), so the total temperature increase for each H_2 molecule that is formed from gas-phase atoms is about twice the above estimate. This finding is in sharp contrast with the situation in which two (physisorbed) H atoms recombine *via* Langmuir-Hinshelwood kinetics: in the latter case only (twice) the H atom physisorption energy would be left on the surface, with hardly any consequence for the grain temperature.

4.3.3 Product energies

Finally, we analyze the energy in the product molecules, investigating the effects of the substrate on the total H_2 energy and on its partitioning between vibrational and translational excitation. We evaluated the average total (ϵ_{tot}), vibrational (ϵ_{V}) and translational (ϵ_{K}) H_2 energies considering both the full dynamical model and the two reduced-dimensional ones described above.

Figure 4.12 shows the results of our analysis in the range of the collision energies considered above. It is seen that the total energy of the newly formed molecule

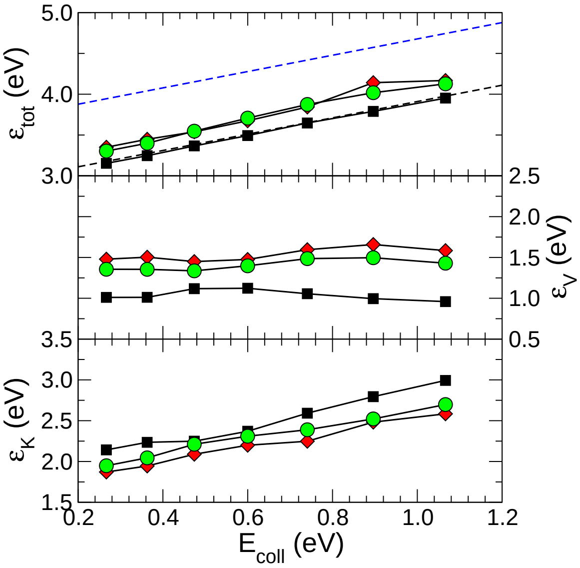

Figure 4.12: Average total (top panel), vibrational (middle panel) and translational (bottom panel) energies of the product H_2 as functions of the collision energy from quantum calculations. The data were obtained with three different substrate models: full (circles), 3D (diamonds) and 2D (squares). In the top panels, the solid lines represent the adiabatic (blue line) and the sudden (black line) limit for the energy transferred to H_2.

(top panel) increases linearly with E_{coll}, as expected from the behavior of the energy transferred to the substrate that was discussed in Sec. 4.3.2. The total energy of the product molecules is much closer to the diabatic limit (dashed black line) than to the adiabatic one (dashed blue line), though the correct description of the C atom dynamics introduces a small, energy-independent contribution from the surface (see also Sec. 4.3.2).

The collisional energy dependence of the product energy comes mainly from the *kinetic* rather than the internal component. As is evident from the middle panel of Fig. 4.12 the vibrational energy shows little variations in the range $E_{coll} = 0.2 - 1.0$ eV and takes a rather large value ($\sim$ 1.5 eV), even though smaller than previously obtained[11–13,15,26,29,64–68]. Importantly, comparison between the 2D and the higher dimensional models, shows that the energy contribution of the lattice is sizable and goes mainly in vibrations. Correspondingly, the translational energy of the H_2 molecules is very similar in the three models, *i.e.* it is less affected by the C atom dynamics, and takes rather large values: the ratio between the translational and the vibrational energy increases from 1.3 at low energies to 1.8 at high energies. In detail, one can see from Fig. 4.12 that the effect of the C atom motion – a sort of 'kick' of the recoiling C atom – favors the channeling of energy into vibrations (ϵ_V computed with the 3D or the full dimensional model is larger by $\sim$ 0.5 eV than that obtained with the 2D model) while reducing the one left in translations, an effect that is slightly less pronounced when the carbon atom binds to a movable rather than a static surface.

We also obtained the vibrational populations p_ν of the product molecule H_2. They are reported in Figure 4.13 for selected values of the collision energy for the 2D (black bars), 3D (red) and full (green) quantum calculations. Our potential model gives rise to vibrational distributions peaked around much lower ν than previously reported[30] (in line with the reduced internal excitation mentioned above), particularly at low

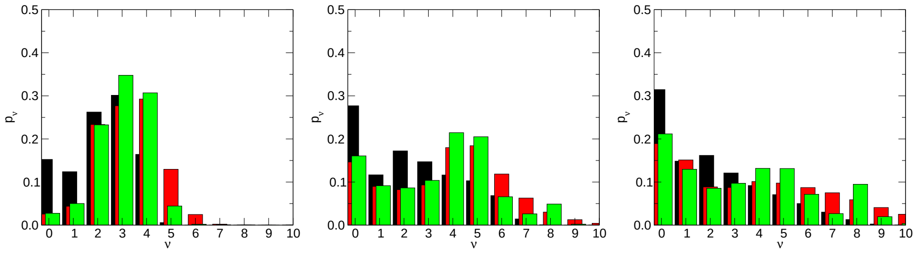

Figure 4.13: Vibrational distributions from our 2D (black) and 3D (red) reduced-dimensional models along with the results obtained with the full Hamiltonian (green), for E_{coll}=0.27, 0.74 and 1.07 eV (left, middle and right panel, respectively).

collision energies. In this E_{coll} regime, other collinear models predict the maximum of the distribution to be around ν=6, 8, while our results show that the most populated states are ν=3, 4, incidentally closer to the experimental data by Latimer *et al.*[69]. This is not due to the C atom motion rather it appears to be mainly an effect of the adopted potential (Eq. 4.20) which, introducing an additional term to describe the carbon atom dynamics, modifies the entrance channel potential. In fact, the results of the 2D model, where the C atom is fixed during the dynamics, show even colder vibrational distributions than the 3D and the full dimensional model. Hence, there remains to establish whether a new fully-fledge potential energy surface including the two H atoms and the binding C atom predicts similar findings or these are artifacts of the SO-like coupling in Eq. 4.20.

When increasing the collision energy the vibrational distributions broaden, becoming eventually bimodal with a first peak centered in the ground vibrational state of H_2 and a second peak at larger values of the vibrational quantum number, ν=4-5. This behavior largely arises from the carbon atom dynamics, as the comparison between the 2D and the higher dimensional results reported in Figure 4.13 shows.

Thus, the dynamics of the C atom not only affects the overall energy partitioning of the reaction but it also changes the shape of the vibrational distributions of H_2. The effect of the rest of the surface, on the other hand, is negligible, and this confirms the idea that the lattice dynamics gets into play right *after* the newly formed molecule has left the surface.

4.4 Summary and concluding remarks

We have investigated the collinear Eley-Rideal H_2 recombination on graphitic surface by means of high dimensional wavepacket simulations with the powerful ML-MCTDH method, as well as of classical and quasi-classical trajectories calculations. The key for the application of a fully quantum approach to the reaction dynamics — one that includes the surface as an active rather than a passive player —- is our system-bath modeling of the Hamiltonian. The resulting model explicitly describes the motion of the binding C atom and, using accurate information on its relaxation dynamics (as subsumed in the spectral density $J_C(\omega)$), replaces the complicated, 'atomistic' surface with a bunch of harmonic oscillators.

Our results show that the reaction probability is mainly influenced by the dynamics of the binding carbon atom. Although H_2 recombination is fast, recoil of this substrate atom does play a role in the dynamics and determines to some extent the energy partitioning. The rest of the surface, on the other hand, has a marginal effect only on the reaction. It does open efficient relaxation channels for the surface unpuckering, but only after that the molecule has left the surface. Moreover, classical and quasi-classical reaction probabilities have been shown to be in qualitative agreement only with the results of quantum simulations, thereby showing the inadequacy, especially at low surface temperature, of the classical dynamics to describe this inherently quantum system. This is mainly due to zero-point-energy effects in the dynamics, *e.g.* quantum fluctuations of the lattice, but it not easily amended with a quasi-classical approach.

We then examined how the energy disposal is shared between substrate and the different excitation channels of the newly formed molecule. The results show that the amount of energy left on the substrate is about the deformation energy stored in lattice during the chemisorption of the target hydrogen atom ($\sim$ 0.8 eV). ΔE_s depends only weakly on the collision energy and is converted into thermal energy that considerably heats the interstellar grains. Given the low temperature of the interstellar dust grains in the diffuse clouds (T_s = 5 - 10 K), the estimated temperature increase of $\sim$0.4 mK *for every single* H_2 *molecule* formed *via* Eley-Rideal recombination is quite remarkable. On the other hand, E_{coll} is almost completely transferred to the product molecule. The total energy of H_2 increases linearly with the incidence energy and it is much closer to the diabatic limit than to the adiabatic one, thereby confirming that the carbon remains close to its puckered position and relaxes only once H_2 is formed. Explicit consideration of the C atom motion, however, promotes vibrational excitation of the product, a kind of recoil effect of the substrate atom, at the expense of the translation energy of H_2.

Overall, the present study represents a first attempt to include the substrate as an active player of the dynamics in a full quantum setting, and our findings do show the importance of including the C atom motion in the description of the reaction (and of accounting for elementary quantum effects such as the initial quantum state of the substrate). They also show, though, that the rest of the lattice plays a marginal role, at least in the collinear configuration considered here.

There remain to establish whether these findings translate unaltered to higher dimensional models where non-collinear collisions are possible and the C atom dynamics is more directly probed by the projectile atom. These non-collinear collisions are actually those determining the size of the reaction cross-section, and could play an important role in determining the energy partitioning in a more realistic situation. To show their possible effect we can tentatively compare the results of our collinear calculations with those of full dimensional (though *classical*) AIMD simulations[26,64] on a T_s = 0 K surface (see Fig. 4.14). It is evident from Fig. 4.14 that the energy partitioning obtained in the two cases is rather different and only the energy transferred to the lattice is in (rough) agreement. It is thus important to establish whether this is an effect of the dimensionality (full *vs.* collinear), of the dynamics (classical *vs.* quantum), of the underlying potential (*ab initio vs.* 'semiempirical') or a combination thereof. Work is currently in progress to extend our simulations to a 4D *plus* bath model that can describe non-collinear collisions, while future work will address the role of the subsystem potential energy surface.

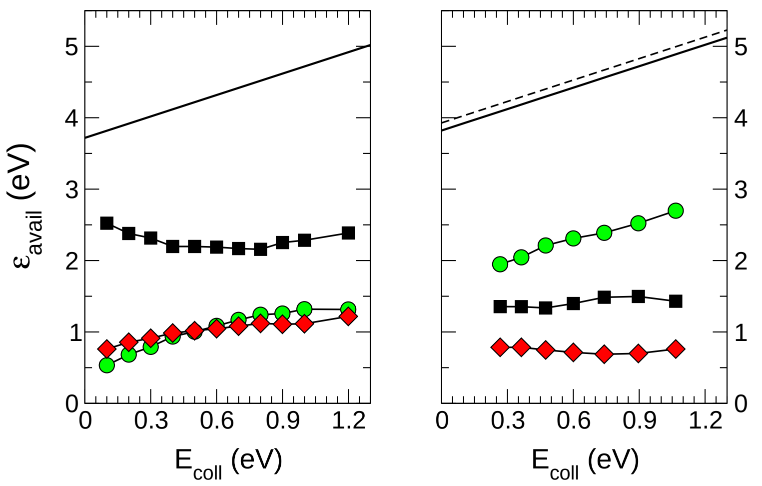

Figure 4.14: Energy partitioning obtained with classical AIMD (left panel) and quantum (right) calculations. Average product energies as functions of the collision energy: internal (square symbols) and translational (circles) energy of H_2 and internal energy of the surface (diamonds). Thick lines mark the reaction exoergicity (on the right panel, thin and dashed line for ZPE and non-ZPE corrected).

Chapter 5

Outlook

Our approach allowed us to investigate the Eley-Rideal abstraction of hydrogen atoms on a graphitic surface in a fully quantum setting including, for the first time, the lattice in the dynamical model. However, much work still needs to be done. In particular, we are interested in studying the isotope effect employing the system-bath model in order integrate our results obtained with the rigid-flat surface approximation (see chapter 3). Furthermore, in order to gain a more realistic description of the reactive process, we have to go beyond the collinear configuration; this can be accomplished using a 7D potential which includes the lateral displacement of the two hydrogen atoms. Indeed, as shown in chapter 3, the non-collinear collisions are crucial in determining the reactive cross sections. Moreover, we would like to improve the efficiency of our calculations employing the G-MCTDH method and to extend our investigation to the energy range relevant for the interstellar medium, *i.e.* cold collision energies.

In the next sections, we will show our preliminary results relative to some the these important further developments.

5.1 Isotope effect

We aim to investigate the isotope effect in the Eley-Rideal H_2 formation on graphite within the system-bath model described in section 4.2 and hence using the Hamiltonian in equation 4.19 and our 3D potential (equation 4.20). We are performing quantum simulations employing the MCTDH method, as well as classical and quasi-classical (QCT) trajectories with the same procedures described in section 4.2.

As in chapter 3, we use “AonB” to indicate the process in which the A atom from the gas phase (the *incidon*) collides with the chemisorbed B atom (the *targon*):

$$\mathrm{A}_{(g)} + \mathrm{B}_{ad} \rightarrow \mathrm{AB}_{(g)}$$

and consider the possible isotopic substitutions (A,B=H,D), with the target atom in its ground-vibrational state.

Our preliminary results relative to the reaction probabilities P_{ER} obtained from quantum calculations for the four possible isotopic substitutions are shown in Figure 5.1. In particular, the data were obtained using our 2D (top panel) and 3D (bottom panel) dynamical models described above; we are still working on the quantum calculations with full dimensionality. In general, the relative trends for both the dynamical models are comparable to the ones obtained within the rigid-flat surface approximation (see Figure 3.2). Indeed, the equal-masses combinations, HonH and DonD, are very similar,

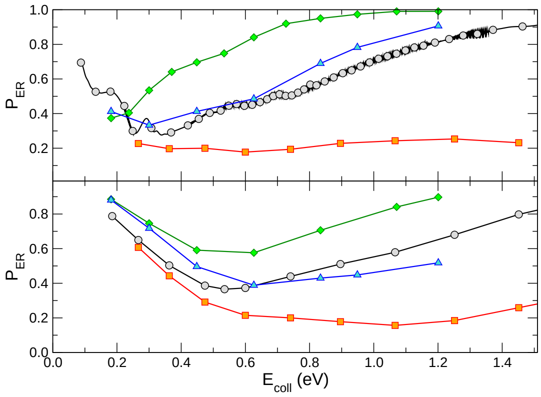

Figure 5.1: Quantum reaction probabilities as functions of the collision energy as obtained from reduced dimensionality calculations (2D in the top panel and 3D in the bottom panel). Results are compared for the four possible isotopic substitutions: HonH (circles), HonD (squares), DonH (diamonds) and DonD (triangles).

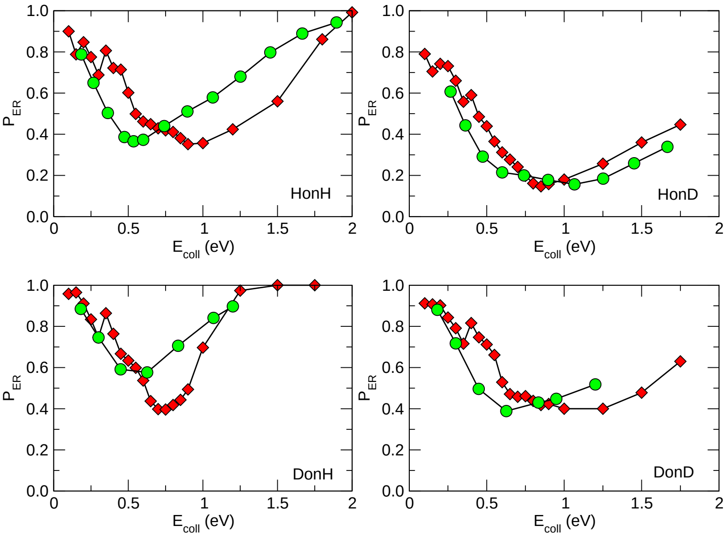

Figure 5.2: Eley-Rideal reaction probabilities as functions of the collision energy obtain from quasi-classical (diamonds) and quantum (circles) calculations employing the 3D model described in the text for the four possible isotopic combinations.

while HonD and DonH are, respectively, the least and the most reactive processes in the considered energy range.

In Figure 5.2, we compare the results obtained from the MCTDH and the quasi-classical calculations. For all the isotopic substitutions, the QCT results qualitatively reproduce the quantum ones, so that they are reliable for a qualitative investigation of the substrate role. In Figure 5.3 a direct comparison between the reaction probabilities obtained from QCT calculations with 2D, 3D and full dynamical models is shown, so that we can have a qualitative glimpse on the effects that the involved masses have on the substrate role. It is seen that the addition of the binding carbon motion has the same effect, independently on the mass of the reactants. Indeed, for all four the isotopic combinations, the introduction of the C atom dynamics leads to a higher (lower) P_{ER} at low (high) E_{coll} with respect to the fixed carbon case, the same trend observed for the HonH case (extensively discussed in section 4.3.1). Moreover, the 3D and the full dimensional models give almost identical results for the reaction probabilities,

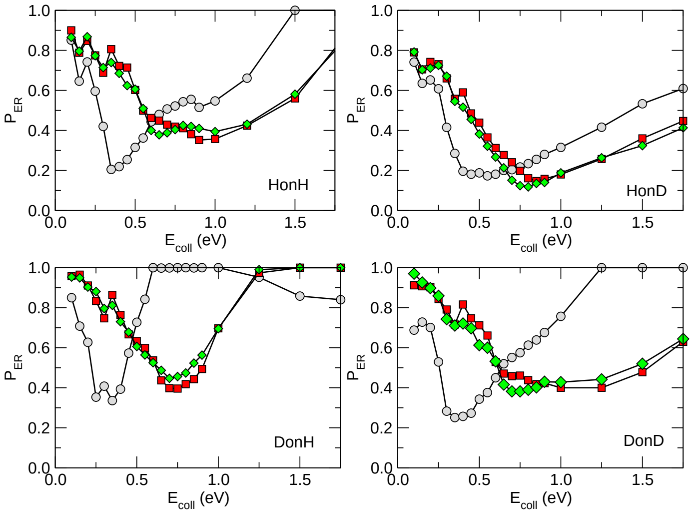

Figure 5.3: ER probabilities as functions of the collision energy as obtained from quasi-classical calculations employing the 2D (circles), 3D (squares) and full (diamonds) dynamical models for the four possible isotopic substitutions.

indicating that, even with heavier masses involved, the reactive process is faster than the substrate relaxation.

5.2 7D potential

In order to include non-collinear collisions in our simulations, we built a 7D analytic potential which takes into account the lateral displacements of the two hydrogen atoms; the binding carbon can move only along the direction normal to the surface, as in the 3D potential case. This approximation is reasonable since the C atom is bound to the rest of the graphitic substrate in either a tetrahedral or a planar configuration, so that its lateral motion is strongly limited. In the 7D model the main system is composed of the three coordinates of the incidon $\mathbf{x_i} = (x_i, y_i, z_i)$, the three coordinates of the targon $\mathbf{x_t} = (x_t, y_t, z_t)$ and the vertical coordinate of the carbon atom z_C. The bath description, as well as the system-bath coupling, remain unchanged with respect of the 3D case. Thus, the working IO Hamiltonian becomes:

$$H = \frac{\mathbf{p_i}^2}{2m_i} + \frac{\mathbf{p_t}^2}{2m_t} + \frac{p_C^2}{2m_C} + V(\mathbf{x_i}, \mathbf{x_t}, z_c) + \sum_k \frac{p_k^2}{2m} + \frac{m\omega_k^2}{2}\left(x_k - \frac{c_k z_c}{m\omega_k^2}\right)^2 \tag{5.1}$$

where $\mathbf{p_j} = (p_{x_j}, p_{y_j}, p_{z_j})$ and $V(\mathbf{x_i}, \mathbf{x_t}, z_c)$ is the 7D analytic potential.

In order to investigate the effect of the substrate on the dynamics, from our full dimensional model (7D system + bath), we devised a lower dimensional model, 7D, in which the graphitic surface role is neglected, *i.e.* the bath is removed.

As preliminary calculations, we are performing classical trajectories at T_s=300 K and quasi-classical calculations at T_s= 0 K, employing the same procedures described in section 4.2; in order to include non-collinear trajectories we introduces the impact parameter in a range between 0 and 6.5 Å. The reactive cross sections σ_{ER}* obtained

---

*In this preliminary analysis, we consider a trajectory to be reactive when at the end of the propagation the two hydrogen atoms are far away from the surface ($z_i, z_t > 10$ Å) and their 3D distance is smaller than ~2 Å.

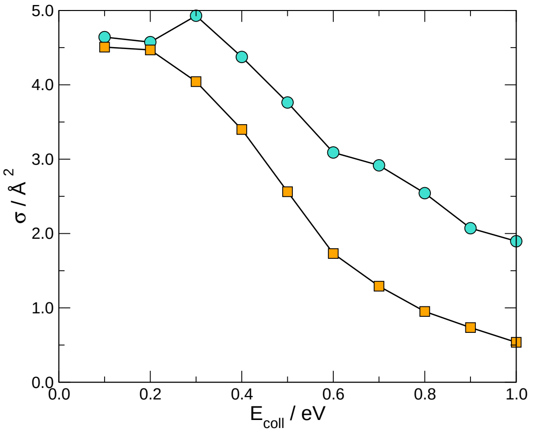

Figure 5.4: Reactive cross sections as functions of the collision energy as obtained from classical calculations at T_s=300 K (squares) and quasi-classical calculations (circles) within our 7D+bath dynamical model.

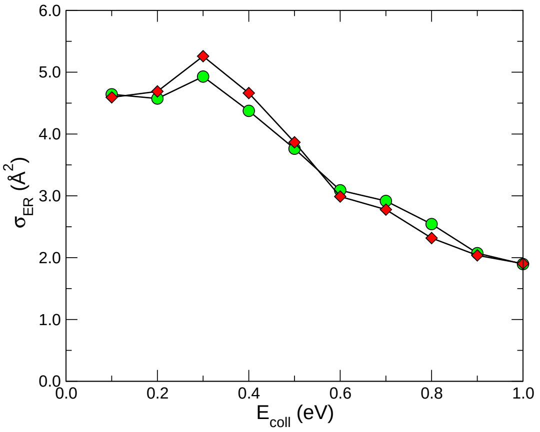

Figure 5.5: Eley-Rideal cross section as function of the collision energy as obtained from quasi-classical calculations within the 7D (diamonds) and full (circles) dynamical models.

from classical and quasi-classical simulations are reported in Figure 5.4. As in the collinear case, the QCT and CT results show the same general trends, although their similarity is only qualitative, since the classical calculations predict a smaller σ_{ER} in the whole energy range. Even if the cross sections have large values (∼5 Å^2 at their maximum), they are in general smaller than obtained in previous works (see Chapter 3). However, in rationalizing the results, we should be aware that quasi-classical and classical trajectories are not completely reliable, since they can reproduce only qualitatively the quantum data. In Figure 5.5 we compare the quasi-classical reactive cross sections σ_{ER} as obtained from our 7D and 7D+bath dynamical models. It is seen that, as previously observed for the collinear case, the reactivity is not affected by the presence of the substrate, which suggests that the H_2 formation dynamics is still faster than the substrate relaxation.

In Figure 5.6, the opacity functions obtained from quasi-classical calculations as functions of the impact parameter b are shown. As previously observed using other dynamical models[13], P(b) has a maximum at intermediate impact parameter values and it decreases for higher b. Comparing our results with the ones obtained by Martinazzo *et al.*[13], it is seen that the main trend of the opacity function is reproduce

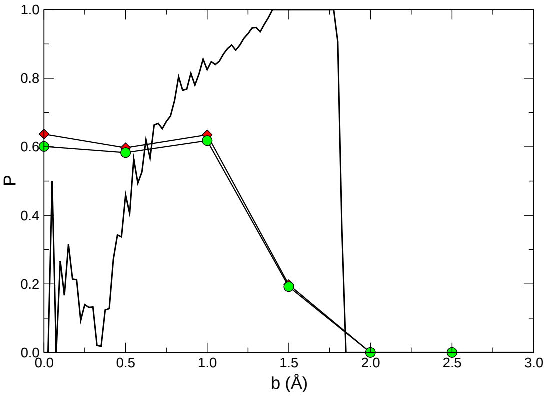

Figure 5.6: Opacity function as function of the impact parameter as obtained from our 7D (diamonds) and full (circles) dynamical models. The black line represent the quasi-classical data obtained by Martinazzo *et al.*[13] employing the LEPS potential[11] and the rigid-flat surface approximation. All the results are relative to a collision energy of 0.5 eV.

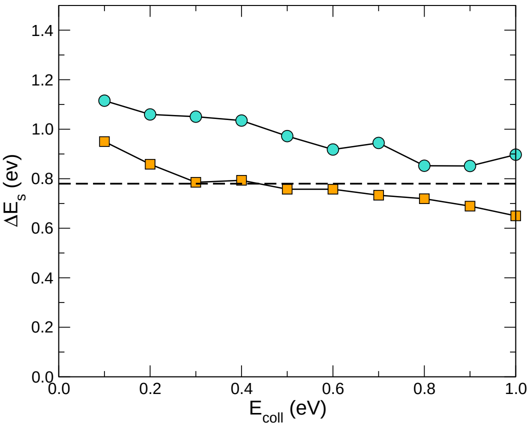

Figure 5.7: ρ-averaged amount of energy transferred to the substrate per reactive event as obtained from classical (T_s=300 K, squares) and quasi-classical (circles) calculations as function of the collision energy. The dashed line is the reference 'puckering energy' stored in the CH bond before the H_2 formation.

only qualitatively, since our calculations give smaller values, as in the case of the cross section. There remains to establish if these trends are due to artifacts in the adopted potential or to the inclusion of the binding carbon dynamics.

Then, we compute the amount of energy transferred to the substrate ΔE_s upon H_2 formation employing the same procedure as in the previous chapter (section 4.3.2), although here we consider a ρ-averaged value taking into account the impact parameters corresponding to the highest reactivity (ρ=0.0, 0.5, 1.0 Å). The results are reported in Figure 5.7 and they show that in the non-collinear case, ΔE_s has a mild dependence on the collision energy, decreasing for increasing E_{coll}. Moreover, in the low collision energy regime ($E_{coll} < 0.4$ eV) it is larger than the 'puckering energy', which implies that part of the collision energy is transferred from the reactants to the graphitic surface.

Our next goals are to obtain 7D and 7D+bath quantum results and to compute the energy components (vibrational, rotational and translational) of H_2; furthermore we want to develop a 6D potential, where the binding carbon is kept fixed, in order to better understand the role of C in the non-collinear configuration, since the ΔE_s

results suggest that there could be differences with respect to the collinear case.

5.3 Gaussian-MCTDH

Although the MCTDH and ML-MCTDH methods represent a remarkable improvement with respect to conventional quantum dynamical approach in treating large systems, their main limit is due to the propagation of multi-dimensional SPFs. A strategy that has been proposed to overcome this issue is the Gaussian-MCTDH (G-MCTDH) method[39,70], which is particularly suitable for complex systems that require an exact quantum dynamics for the so-called "primary modes", *i.e.* the dynamically active DOFs of the problem, while an approximate propagation is adequate for a class of "secondary modes", *i.e.* the environmental DOFs with a passive role. Thus, this method is perfectly suited for the application of the unitary system-bath approach.

5.3.1 G-MCTDH theory

In the G-MCTDH approach some or all the degrees of freedom are represented in terms of parametrized basis functions with a determined functional form, specifically analytic Gaussian wavepackets (GWPs). Although some flexibility in the wavefunction representation is lost, the computational efficiency is improved; indeed, the basis set representation of the SPFs is avoided and the time evolution of a set of parameters is computed instead.

The wavefunction *ansatz* in the G-MCTDH approach can be expressed as:

$$\Psi = \sum_J A_J \left(\prod_{k=1}^{p} \phi_{j_k}^{(k)} \right) \left(\prod_{k=p+1}^{f} g_{j_k}^{(k)} \right) \tag{5.2}$$

where p "primary" degrees of freedom are represented with conventional, fully flexible SPFs $\phi_{j_k}^{(k)}$, while the form of multidimensional GWPs $g_{j_k}^{(k)}$ is imposed to the remaining "secondary" DOFs. In particular, the GWPs has the following functional expression:

$$\begin{aligned} g_j^{(k)} &= g_j^{(k)} \left(\mathbf{\Lambda}_j^{(k)}; \mathbf{x}_k \right) \\ &= exp \left[\mathbf{x}_k^T \mathbf{a}_j^{(k)}(t) \mathbf{x}_k + (\boldsymbol{\xi}_j^{(k)}(t))^T \mathbf{x}_k + \eta_j^{(k)}(t) \right] \end{aligned} \tag{5.3}$$

and they are characterized by time dependent parameters $\mathbf{\Lambda}_j^{(k)}(t) = (\mathbf{a}_j^{(k)}(t), \boldsymbol{\xi}_j^{(k)}(t), \eta_j^{(k)}(t))$, each of which describes a feature of the GWP. In particular:

- $\mathbf{a}_j^{(k)}$ is a complex, symmetric matrix which defines the width of the multidimensional $g_j^{(k)}$ and whose off-diagonal elements contain the correlation between the DOFs represented with the GWP;

- $\boldsymbol{\xi}_j^{(k)}$ is a complex vector describing the center of the Gaussian function in the phase-space;

- $\eta_j^{(k)}$ is a complex number, whose real component determines the GWP norm, while the imaginary part is a phase factor.

Starting from equation 5.3 two kinds of Gaussian wavepackets are used in practice. On one hand, the *thawed* Gaussians depend on all three the parameters and, in particular, the width matrix $\mathbf{a}_j^{(k)}$ is a time dependent variational parameter. On the other hand, with *frozen* Gaussians the width matrix is fixed throughout the dynamics, so that $g_j^{(k)}$ depend only on two parameters $\boldsymbol{\Lambda}_j^{(k)}(t) = (\boldsymbol{\xi}_j^{(k)}(t), \eta_j^{(k)}(t))$.

As in standard MCTDH method, the wavefunction representation is not unique, so that singularities can appear in the equations of motion. Thus, in general, the constraints in equation 2.44 and 2.45 are imposed to the conventional SPFs $\phi_{j_k}^{(k)}$'s - and in the following we consider $h^{(k)} = 0$ -. On the other hand, no constraints are applied to the GWPs, since the imposed functional form can be seen as a constraint itself; however, conventionally, the real part of $\eta_j^{(k)}$ is fixed so that the GWP is always normalized, while its imaginary part is either set to zero or evolved with the classical action.

In order to obtain the equations of motion for the G-MCTDH method, the same procedure applied for the standard approach is used. In particular, the EoMs relative to the conventional SPFs are unchanged with respect to the MCTDH method (equation 2.51), while a correlation between the coefficients A_J and the parameters $\boldsymbol{\Lambda}_j^{(k)}$ appears. Indeed, the equations of motion relative to A_J and $\boldsymbol{\Lambda}_j^{(k)}$ are:

$$i\dot{\mathbf{A}} = \left(\mathbf{S}^{-1}\mathbf{H} - i\mathbf{S}^{-1}\sum_{\alpha}\mathbf{S}^{0\alpha}\dot{\boldsymbol{\Lambda}}_{\alpha}\right)\mathbf{A} \tag{5.4}$$

$$i\dot{\boldsymbol{\Lambda}} = \mathbf{C}^{-1}\mathbf{Y} \tag{5.5}$$

where $\mathbf{S}^{(\chi)}$ is the overlap matrix for the SPFs relative to the χth DOF, *i.e.* $S_{jl}^{(\chi)} = \delta_{jl}$ for standard single particle functions and $S_{jl}^{(\chi)} = \langle g_j^{(\chi)} | g_j^{(\chi)} \rangle$ and $\mathbf{H}$ is the mean field Hamiltonian. The elements of the matrices $\mathbf{C}$ and $\mathbf{Y}$ are defined as:

$$C_{j\alpha,l\beta} = \rho_{jl}^{f}\left(S_{jk}^{(\alpha\beta)} - \left[\mathbf{S}^{(\alpha0)}\mathbf{S}^{-1}\mathbf{S}^{(0\beta)}\right]_{jl}\right)$$

$$Y_{j\alpha} = \sum_{l}\left(\langle H_{jl}^{(\alpha0)}\rangle_{jl} - \left[\mathbf{S}^{(\alpha0)}\mathbf{S}^{-1}\langle \mathbf{H}_{jl}\rangle\right]_{jl}\right)$$

ρ_{jl}^{f} being the elements of the density matrix. Equations 2.51, 5.4 and 5.5 are the working equations for the dynamics of the G-MCTDH method and it can be seen (equations 5.4 and 5.5) that the solution for the coefficients depends on the solution for the parameters.

5.3.2 G-MCTDH preliminary calculations

In order to evaluate the potential efficiency gain due to the employ of the G-MCTDH method, we tried to reproduce our results obtained from standard ML-MCTDH calculations. Our goal is to decrease the computational cost of our simulations by substituting the Hermite DVR used in the representation of the bath modes with frozen Gaussian wavepackets.

We prepared two different inputs to evaluate the best set up for the 32 harmonic oscillators composing the bath. In the first input, we set 32 1-dimensional modes described by one frozen GWP each, *i.e.* one for each degree of freedom; while in the second input, we chose 4-dimensional modes described with one Gaussian each. In both of the inputs, the main system was represented in a 3D combined mode described with one SPF and uniform grids were used as primitive basis. As a comparison, we prepared two other inputs with the same set up as above, but with standard Hermite basis instead of GWPs. Thus, we were able to perform efficiency tests, comparing the computational (wall) time needed to propagate for 10 fs the wavefunction generated by the inputs described above. The results are summarized in table 5.1 and they unexpectedly show that the calculations with the G-MCTDH method are actually much slower than with the standard MCTDH representation of the wavefunction. Thus, more work still needs to be done to find an optimized representation of the wavefunction in order to reduce the computational costs of our calculations, especially in the perspective of 7D + bath simulations.

Bath representation	Wall time (min)
1D GWPs	20
1D Hermite	2
4D GWPs	19
4D Hermite	1

Table 5.1: Computational (wall) time needed to perform a propagation of 10 fs with the set up described in the main text.

Bibliography

[1] E. Herbst, Chemical Society Reviews **30**, 168 (2001).

[2] R. A. Bernstein, W. L. Freedman, and B. F. Madore, The Astrophysical Journal **571**, 107 (2002).

[3] R. I. Kaiser, Chemical Reviews **102**, 1309 (2002).

[4] J. S. Mathis, Annual Review of Astronomy and Astrophysics **28**, 37 (1990).

[5] B. T. Draine, Annual Review of Astronomy and Astrophysics **41**, 241 (2003).

[6] P. Ehrenfreund, W. Irvine, L. Becker, J. Blank, J. Brucato, L. Colangeli, S. Derenne, D. Despois, A. Dutrey, H. Fraaije, *et al.*, Reports on Progress in Physics **65**, 1427 (2002).

[7] A. Dalgarno and J. Black, Reports on Progress in Physics **39**, 573 (1976).

[8] R. Gould, T. Gold, and E. Salpeter, The Astrophysical Journal **138**, 393 (1963).

[9] D. Hollenbach and E. Salpeter, The Journal of Chemical Physics **53**, 79 (1970).

[10] D. Hollenbach and E. Salpeter, The Astrophysical Journal **163**, 155 (1971).

[11] X. Sha, B. Jackson, and D. Lemoine, The Journal of Chemical Physics **116**, 7158 (2002).

[12] S. Morisset, F. Aguillon, M. Sizun, and V. Sidis, The Journal of Physical Chemistry A **108**, 8571 (2004).

[13] R. Martinazzo and G. F. Tantardini, The Journal of Chemical Physics **124**, 124702 (2006).

[14] D. Bachellerie, M. Sizun, F. Aguillon, D. Teillet-Billy, N. Rougeau, and V. Sidis, Physical Chemistry Chemical Physics **11**, 2715 (2009).

[15] S. Casolo, R. Martinazzo, M. Bonfanti, and G. F. Tantardini, The Journal of Physical Chemistry A **113**, 14545 (2009).

[16] A. J. Meijer, A. J. Farebrother, D. C. Clary, and A. J. Fisher, The Journal of Physical Chemistry A **105**, 2173 (2001).

[17] R. Martinazzo, S. Casolo, and L. H. Hornekær, "Dynamics of gas-surface interactions: Atomic-level understanding of scattering processes at surfaces," (Springer, Berlin, Heidelberg, 2013) Chap. Hydrogen Recombination on Graphitic Surfaces, pp. 201–213.

[18] B. Lepetit and B. Jackson, Physical Review Letters **107**, 236102 (2011).

[19] E. Ghio, L. Mattera, C. Salvo, F. Tommasini, and U. Valbusa, The Journal of Chemical Physics **73**, 556 (1980).

[20] M. Bonfanti, R. Martinazzo, G. F. Tantardini, and A. Ponti, The Journal of Physical Chemistry C **111**, 5825 (2007).

[21] M. Bonfanti, B. Jackson, K. H. Hughes, I. Burghardt, and R. Martinazzo, The Journal of Chemical Physics **143**, 124704 (2015).

[22] M. Bonfanti, B. Jackson, K. H. Hughes, I. Burghardt, and R. Martinazzo, The Journal of Chemical Physics **143**, 124703 (2015).

[23] E. Aréou, G. Cartry, J.-M. Layet, and T. Angot, The Journal of Chemical Physics **134**, 014701 (2011).

[24] S. Morisset, F. Aguillon, M. Sizun, and V. Sidis, The Journal of Chemical Physics **122**, 194702 (2005).

[25] R. Martinazzo and G. F. Tantardini, The Journal of Chemical Physics **124**, 124703 (2006).

[26] S. Casolo, G. F. Tantardini, and R. Martinazzo, Proceedings of the National Academy of Sciences **110**, 6674 (2013).

[27] A. Douglas and G. Herzberg, The Astrophysical Journal **94**, 381 (1941).

[28] M. Agúndez, J. Goicoechea, J. Cernicharo, A. Faure, and E. Roueff, The Astrophysical Journal **713**, 662 (2010).

[29] R. Martinazzo and G. F. Tantardini, The Journal of Physical Chemistry A **109**, 9379 (2005).

[30] M. Pasquini, M. Bonfanti, and R. Martinazzo, Physical Chemistry Chemical Physics **18**, 6607 (2016).

[31] J. R. Taylor, *Scattering theory: the quantum theory of nonrelativistic collisions* (Courier Corporation, 2006).

[32] J. Light, I. Hamilton, and J. Lill, The Journal of Chemical Physics **82**, 1400 (1985).

[33] R. G. Littlejohn, M. Cargo, T. Carrington Jr, K. A. Mitchell, and B. Poirier, The Journal of Chemical Physics **116**, 8691 (2002).

[34] R. Meyer, The Journal of Chemical Physics **52**, 2053 (1970).

[35] D. T. Colbert and W. H. Miller, The Journal of Chemical Physics **96**, 1982 (1992).

[36] G. Worth, M. Beck, A. Jäckle, H. Meyer, F. Otto, M. Brill, and O. Vendrell, User's Guide, Version **8** (2000).

[37] M. H. Beck, A. Jäckle, G. Worth, and H.-D. Meyer, Physics Reports **324**, 1 (2000).

[38] H.-D. Meyer, F. Gatti, and G. A. Worth, Multidimensional Quantum Dynamics: MCTDH Theory and Applications , 17 (2009).

[39] S. Römer, M. Ruckenbauer, and I. Burghardt, The Journal of Chemical Physics **138**, 064106 (2013).

[40] H. Wang and M. Thoss, The Journal of Chemical Physics **119**, 1289 (2003).

[41] M. Persson and B. Jackson, The Journal of Chemical Physics **102**, 1078 (1995).

[42] D. Lemoine and B. Jackson, Computer Physics Communications **137**, 415 (2001).

[43] R. Martinazzo and G. F. Tantardini, The Journal of Chemical Physics **122**, 094109 (2005).

[44] M. Bonfanti, S. Casolo, G. F. Tantardini, and R. Martinazzo, Physical Chemistry Chemical Physics **13**, 16680 (2011).

[45] D. Lemoine, The Journal of Chemical Physics **101**, 3936 (1994).

[46] M. Feit, J. Fleck, and A. Steiger, The Journal of Computational Physics (1982).

[47] B. Jackson and D. Lemoine, The Journal of Chemical Physics **114**, 474 (2001).

[48] S. Casolo, O. M. Løvvik, R. Martinazzo, and G. F. Tantardini, The Journal of Chemical Physics **130**, 054704 (2009).

[49] A. J. Meijer, A. J. Farebrother, and D. C. Clary, The Journal of Physical Chemistry A **106**, 8996 (2002).

[50] T. Millar, Planetary and Space Science **50**, 1189 (2002).

[51] T. Millar, Astronomy & Geophysics **46**, 2 (2005).

[52] M. Bonfanti, K. H. Hughes, I. Burghardt, and R. Martinazzo, Annalen der Physik **527**, 556 (2015).

[53] M. Bonfanti and R. Martinazzo, "Research advances in quantum dynamics," (InTech, Rijeka, 2016) Chap. 8, Unitary Approaches to Dissipative Quantum Dynamics.

[54] G. W. Ford, J. T. Lewis, and R. O'connell, Physical Review A **37**, 4419 (1988).

[55] A. O. Caldeira and A. J. Leggett, Physica A: Statistical mechanics and its Applications **121**, 587 (1983).

[56] J. Kerwin, X. Sha, and B. Jackson, The Journal of Physical Chemistry B **110**, 18811 (2006).

[57] H.-D. Meyer, U. Manthe, and L. S. Cederbaum, Chemical Physics Letters **165**, 73 (1990).

[58] M. Hans-Dieter, F. Gatti, and G. A. Worth, *Multidimensional quantum dynamics* (WILEY-VCH, 2009).

[59] G. A. Worth, M. H. Beck, A. Jäckle, O. Vendrell, and H.-D. Meyer, The MCTDH Package, Version 8.2, (2000). H.-D. Meyer, Version 8.3 (2002), Version 8.4 (2007). O. Vendrell and H.-D. Meyer Version 8.5 (2013). Version 8.5 contains the ML-MCTDH algorithm. Current versions: 8.4.12 and 8.5.5 (2016). See http://mctdh.uni-hd.de/.

[60] O. Vendrell and H.-D. Meyer, J. Chem. Phys. **134**, 044135 (2011).

[61] S. Sakong and P. Kratzer, The Journal of Chemical Physics **133**, 054505 (2010).

[62] M. Bonfanti and R. Martinazzo, International Journal of Quantum Chemistry **116**, 1575 (2016).

[63] M. Bonfanti, M. F. Somers, C. Díaz, H. F. Busnengo, and G.-J. Kroes, Zeitschrift für Physikalische Chemie **227**, 1397 (2013).

[64] S. Casolo, G. Tantardini, and R. Martinazzo, The Journal of Physical Chemistry A **120**, 5032 (2016).

[65] A. J. H. M. Meijer, A. J. Farebrother, D. C. Clary, and A. J. Fisher, The Journal of Physical Chemistry A **105**, 2173 (2001).

[66] M. Rutigliano, M. Cacciatore, and G. Billing, Chemical Physics Letters **340**, 13 (2001).

[67] S. Morisset, F. Aguillon, M. Sizun, and V. Sidis, Physical Chemistry Chemical Physics **5**, 506 (2003).

[68] S. Morisset, F. Aguillon, M. Sizun, and V. Sidis, Chemical Physics Letters **378**, 615 (2003).

[69] E. R. Latimer, F. Islam, and S. D. Price, Chemical Physics Letters **455**, 174 (2008).

[70] I. Burghardt, H.-D. Meyer, and L. Cederbaum, The Journal of Chemical Physics **111**, 2927 (1999).